THE UNIVERSITY OF CHICAGO

DEVELOPING SEMI-LADDER POLYMER SYSTEMS FOR LIGHT-EMITTING TRANSISTOR APPLICATIONS

A DISSERTATION SUBMITTED TO

THE FACULTY OF THE DIVISION OF THE PHYSICAL SCIENCES

IN CANDIDACY FOR THE DEGREE OF

DOCTOR OF PHILOSOPHY

DEPARTMENT OF CHEMISTRY

BY

MOHAMMAD AHMAD AWAIS

CHICAGO, ILLINOIS

MARCH 2021

TABLE OF CONTENTS

LIST OF SCHEMES

LIST OF FIGURES

LIST OF TABLES

ACKNOWLEDGEMENTS

Choosing to go to graduate school at the University of Chicago has been one of the most pivotal decisions of my life. It has been challenging, at times frustrating, but a rewarding experience never the less. Asking the right questions, searching for the correct answers, and experiencing that ‘aha’ moment when one stumbles upon it makes all the effort worthwhile.

First of all, I would like to thank my supervisor, Professor Luping Yu, for mentoring me throughout graduate school, for his patience, and for everything I learned from him. I would also like to thank Professors Bozhi Tian and David Mazziotti for agreeing to be a part of my dissertation committee.

Next, I would like to thank my late grandfather, a Chemistry Ph.D. himself, for instilling in me a love for Chemistry that has remained a part of me to this day and will remain so for the rest of my life. I would also like to thank my parents and my fiancé; my parents for always supporting my academic pursuits, encouraging me to pursue graduate school, and taking an interest in my research without having the background to understand most of it; my fiancé for her support throughout the dissertation writing process.

It would be unfair if I fail to mention my senior lab mates Dr. Andriy Neshchadin, Dr. Xunshan Liu, and Dr. Valerii Sharapov, for their help and support during the entire Ph.D. process. I would especially like to thank Dr. Dafei Yuan for his device work, without which the materials I synthesized would never have realized their full potential. I am grateful to have had the pleasure of working alongside you all.

Chapter 1

Organic Light-Emitting Transistors: Materials and Devices

1.1 Background

The first known example of electrical conduction in organic systems dates back to 1862 when Letheby observed slight electrical conduction in polyaniline synthesized from anodic oxidation of aniline in sulfuric acid. [1] Then, in 1960, after a hiatus of a hundred years, Kallmann and Pope observed hole current flowing through an anthracene crystal in contact with a positively charged electrolyte acting as a hole injector. [2,3] This work was followed by Heeger, MacDiarmid and, Shirakawa in 1977 when they discovered electrical conductivity in iodine-treated polyacetylene. [4] These works firmly established organic systems as potential electrical conductors that could be applied to various optoelectronic devices.

Fast-forward forty years, organic semiconductors have become increasingly attractive optoelectronic materials. [5] The past few decades have witnessed several optoelectronic devices based on organic semiconductors. These include field-effect transistors (FET), light-emitting diodes (LED), and photovoltaics (PV). [5–8] The first of these examples date back to 1986 when Tsumura developed a polythiophene thin-film based organic field-effect transistor (OFET). Although rudimentary by current standards, their device exhibited an on/off ratio of 10^3 and a charge carrier mobility of 10^{-5} cm^2/Vs. [7] A year later, Tang developed an Alq_3 based organic light-emitting diode (OLED). Their device had decent external quantum efficiency (EQE) of 1% and

brightness larger than 1000 cd/m^2, both of which were achieved at driving voltages of less than 10 V. [6] Two decades later, in 2003, Hepp combined both light-emitting as well as current modulating functionalities in a single organic light-emitting transistor (OLET) device. Based on the tetracene small molecule as an active layer, his device consisted of Au source and drain electrodes deposited on a Si/SiO_2 substrate. However, their p-type device only emitted near the drain electrode with an EQE of only 6.7×10^{-5} %.

Although inorganic materials outperform their organic counterparts in device performance, recent development has narrowed this performance gap significantly over the past few years. [9] Moreover, organic systems enjoy certain advantages over their inorganic counterparts: Firstly, the optoelectronic properties of organic systems can be easily tuned by introducing any combination of a vast spectrum of functional groups and by varying molecular structure. [9,10] Secondly, when compared to inorganic semiconductors, organic materials are lightweight, mechanically flexible, and can be incorporated into devices of varying architectures, leading to soft electronics. [11] Thirdly, organic systems are solution-processable to avoid high temperature and rigid fabrication protocols associated with inorganic systems. [9–11]

1.2 Research Problem

While OLEDs have been extensively researched and commercialized, research in OLETs is still in its infancy stage and offers abundant research and development opportunities. As opposed to an OLED device, in which charge carriers travel vertically through a 100 nm thick active layer, the OLET device requires charge carriers to travel horizontally between source-drain electrodes across a 10-100 μm long channel. [12] This forces OLET charge carriers to experience charge

trapping and recombination with nonradiative decay, effectively quenching light emission. This difference makes the development of OLETs significantly more challenging than that of OLEDs.

Several factors need to be considered while developing active materials for OLET devices. Firstly, the organic system being considered must exhibit the appropriate HOMO/LUMO energy levels to emit light in the appropriate region of the visible spectrum and minimize the energy barrier for charge injection from the metal source-drain electrodes. Secondly, it needs to have high and balanced hole/electron mobility to reduce the potential for exciton quenching due to interaction with metallic electrodes and emit at the channel's center. Lastly, it needs to be soluble and have a high photoluminescence quantum yield in solid-state. Unfortunately, high charge carrier mobility, high solid-state photoluminescence, and high solubility are difficult to achieve simultaneously. For instance, strong pi-pi stacking leading to increased orbital overlap is beneficial for charge transport but opens up additional nonradiative decay pathways via excimer/exciplex formation. Conversely, poor pi-pi stacking as a consequence of extensive sidechain engineering favors high solubility and solid-state photoluminescence but leads to low mobility. [13,14] Thus, for optimal OLET device performance, one needs to find the right balance between the three.

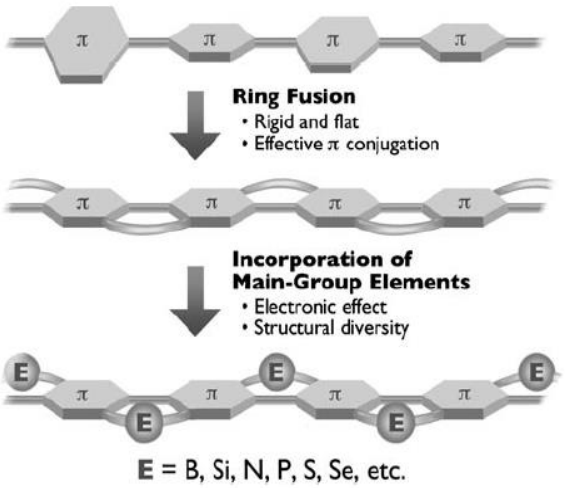

Figure 1.1: Ladder Type System. Reprinted with permission from Ref. [14]

One way to address this issue is to employ double-stranded ladder-type structures which are covalently interconnected and conformationally locked as in a physical ladder (**Figure 1.1**). [13–16] These molecules offer certain unique structural features. [17] For instance, the fused ring constriction introduces rigidity in these systems and prevents torsional rotation between the aromatic units along the molecular backbone. This reduces the number of vibrational modes available for nonradiative decay and improves the emission quantum yield. These systems' uniquely planar structure exhibits no torsional rotation and zero dihedral angles, which offers improved pi-conjugation and enhanced charge transport. However, complete ladder systems also introduce strong pi-pi stacking interactions, which are detrimental to emission quantum yield and solubility. [13,14] Therefore, the solution lies somewhere between the two extremes of the ladder spectrum. We conceived semi-ladder polymers as a possible solution to this problem. It was hypothesized that such a system would allow us to access high charge carrier mobility, high solid-state photoluminescence, and high solubility simultaneously.

Another solution is to develop devices with multi-layered structures, in which one system is used for charge transport, and another is employed for emission in the same OLET device. If this device is to be mass-produced inexpensively, the active layer needs to be soluble in solvents orthogonal to the ones used for the charge transport layer. Thus, the following chapters will seek to address these issues by employing semi-ladder polymers in solution-processed multi-layered OLET devices.

1.3 Working Principles

Like any organic optoelectronic device, OLET device performance is intimately associated with issues such as the class of active optoelectronic materials, their packing structure, device

architecture, and operating conditions. [18] While several classes of optoelectronic materials with varying device architectures have been employed successfully in OLET devices we will only be dealing with single gate devices using purely organic systems.

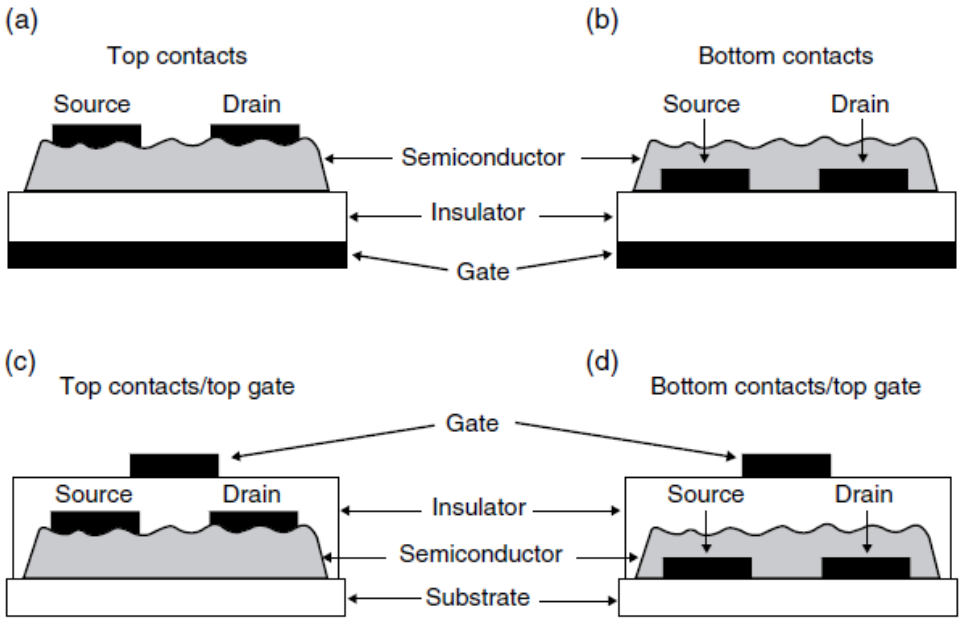

Figure 1.2: OLET Architectures. Reprinted with permission from Ref. [19]

The most basic OLET device architecture is identical to that of a field-effect transistor with source and drain electrodes, a gate electrode, a substrate, a dielectric, and an active layered organic semiconductor. Here, the gate and source and drain electrodes can either be on top or the bottom, as shown in **Figure 1.2**. [19] It is well known that the choice of material for source and drain is critical. Ideally, they should have work functions such that the energy barrier for hole and electron injection is kept minimal, and both charge carriers can easily inject into the active layer and combine to form an exciton pair. This exciton pair can then decay radiatively and emit light at the appropriate wavelength. It is required that the device exhibit ambipolar charge transport characterized by a V-shaped I-V transfer curve where each of the branches around the minima corresponds to either hole or electron transport, with the minima representing the ambipolar region.

However, most semiconducting materials, especially those with a relatively large bandgap (> 1.5 eV), are not ambipolar. In these non-ideal cases, while the energy gap for hole injection is relatively low as the HOMO energy level of the active layer is usually close to the work function of gold (5.1 eV), the energy gap for electronic injection is relatively high as the LUMO energy level is a lot higher than the work function of gold. This then leads to unipolar charge transport with the electrons acting as the minority carriers and emission happening near the drain electrode as opposed to the middle of the channel. This scenario yields a low EQE, with most of the exciton pairs decaying nonradiatively due to their interaction with gold atoms at the drain electrode. In rare cases, ambipolar transport is possible with gold electrodes, albeit with high non-ohmic contact resistance. [20]

This problem can be addressed in one of two ways. Firstly, one can employ a low work function metal such as calcium as a drain electrode to lower the electron injection energy barrier. However, using asymmetric electrodes will necessarily complicate the device architecture and make large scale fabrication of such devices tedious and expensive. Alternatively, one can insert effective electron-transporting (ETL) and hole-transporting layers (HTL) with appropriate energy levels to sandwich the active layer, which will lower the energy barrier for carrier injection. Judicious selection of charge-transporting and active layers made it possible to use orthogonal solvents for the device fabrication. The subsequent chapters will employ this strategy to optimize device performance.

When a low bandgap (<1.5 eV) semiconductor is used, the resulting devices usually exhibit ambipolar behavior without any special requirements due to a small injection barrier for both holes and electrons. Charge carrier traps at the dielectric-semiconductor interface must also be kept to a

minimum. This is usually ensured by carrying out device fabrication in a completely dry nitrogen/argon atmosphere.

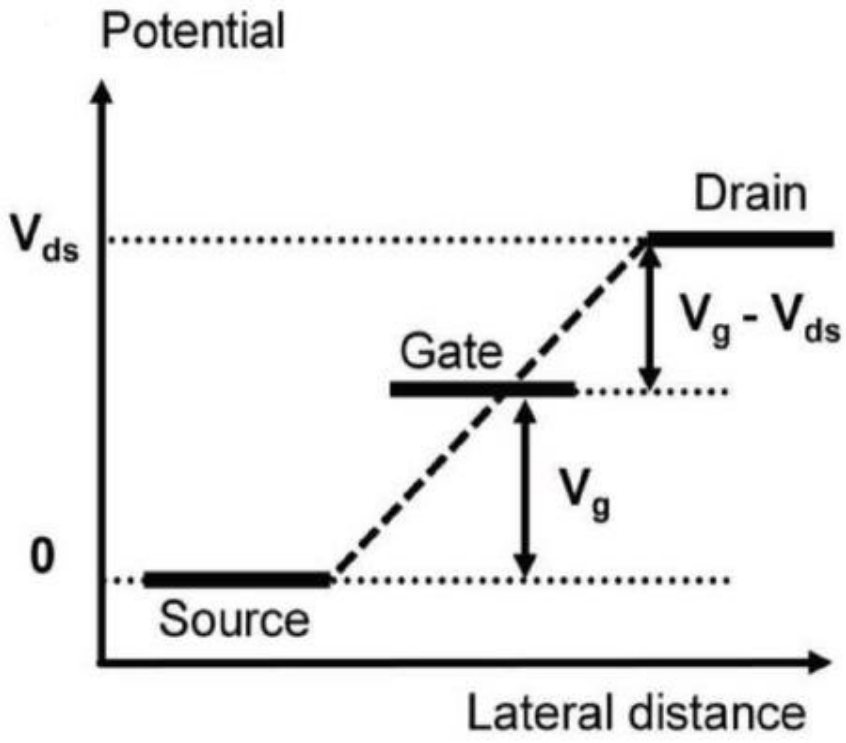

Figure 1.3*:* OLET Operation. Reprinted with permission from Ref. [21]

Assuming these conditions are fulfilled, the device operation depends on the applied source-drain and gate voltages, as illustrated in **Figure 1.3**. [21] If the gate-source voltage is positive but smaller than the drain-source voltage, the effective gate voltage with respect to the drain becomes negative. This ensures that electrons are injected from the source, and holes are injected from the drain. The higher the drain-source voltage, the earlier the onset of hole injection with respect to the gate voltage. This is also true of negative gate-source and drain-source voltages where hole injection takes place from the source and electron injection from the drain. [21]

In a fully functional device, each of the carrier concentrations depends on the effective local potential where each of them approaches zero at the point of recombination and emission

zone. Moreover, it is assumed that all the charge carriers combine with the number of holes equaling the number of electrons, which is determined by the drain current. The recombination zone here moves from the drain to the source electrodes with increasing gate voltages, with the drain current being maximum at the edges and minimum at the center (**Figure 1.4**). [21]

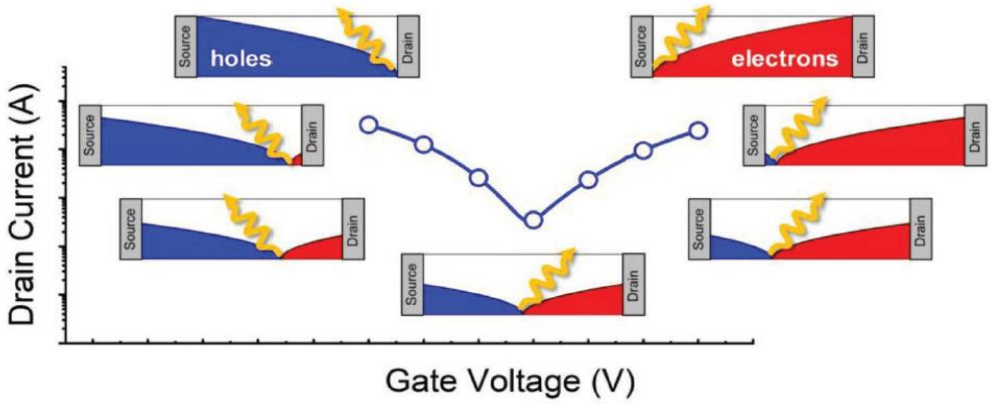

Figure 1.4: Spacial illustration of holes, electrons, and emission zone. Reprinted with permission from Ref. [21]

1.4 Device Configuration

As previously discussed, an OLET is composed of an electroluminescent semiconducting organic system that acts as an electrical channel for holes and electrons. At one end of the channel, there is a source electrode, followed by a drain electrode at the other end of the channel. In between the gate and the organic system, we have a dielectric layer allowing for current modulation through the gate.

While any OLET device has all five components described in the previous paragraph, their positioning with respect to the semiconducting organic system can be different in different configurations (**Figure 1.2**). For instance, the source/drain electrodes can be positioned above or below the semiconducting layer to give top contact or bottom contact device, respectively. In the same way, the gate can be placed above or below the semiconducting layer to give a top gate or

bottom gate device, respectively. Each of these four configurations has certain advantages and disadvantages. These will be described below.

For instance, BC devices generally have greater contact resistance than their TC counterparts. Modification of the dielectric surface is tricky in BG-BC configuration since source/drain electrodes prevent the modification of the dielectric edges. Devices such as BG-BC are easier to fabricate as they involve fewer steps when compared to BG-TC devices. Additionally, since gate and source/drain contacts are patterned before organic semiconductor deposition, any heat-assisted degradation of the organic system is ruled out. Microscale BG-BC devices can be pre-patterned by photolithography. BC devices generally exhibit cavitation and smaller grain sizes of the organic semiconductor system near the contacts, leading to low conductivity. [19,22] In BG-TC and TG-BC devices, the charge injection zone (electrode/organic semiconductor interface) is kept separate from the charge transport zone (organic semiconductor/dielectric interface). This makes dielectric layer modification a straightforward process. [19]

TC devices generally exhibit lower contact resistances as compared to BC devices. This is most likely due to increased surface area at the contact/ organic semiconductor interface. However, such devices have increased access resistance as the charge carriers have to travel from the source down to the organic semiconductor/dielectric interface and then back up to the drain. Nevertheless, access resistance can be kept at a minimum by minimizing organic active layer thickness. Access resistance is only a concern in TC devices, whereas, in BC devices, the conductance channel is in the same plane as source/drain contacts. As for the two TG configurations, TG-TC devices offer less resistance as TG-BC devices can potentially have access resistance. However, both TG devices suffer from unevenness at the organic semiconductors' top surface, making for an unstable dielectric/organic semiconductor interface. In such devices, perfect alignment of the gate electrode

across the entirety of the device often proves tricky, which can lead to additional contact resistance across the ungated section of the organic semiconductor.

Table 1.1: OLET Materials

Organic Semiconductor	Device Type	Optoelectronic Properties
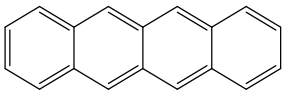 Tetracene	Unipolar [8]	λ_{max} = 540 nm luminance = 45 cdm^{-2} EQE = 6.7×10^{-5}%
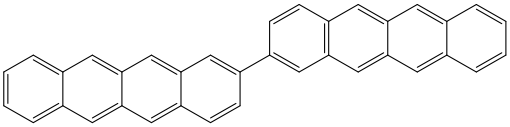 Ditetracene	Ambipolar [23]	λ_{max} = 580 nm EQE = 0.012%
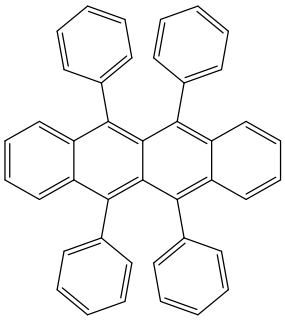 Rubrene	Ambipolar [24]	$\mu_h = 1.8 \times 10^{-2}$ cm^2/Vs $\mu_e = 1.1 \times 10^{-2}$ cm^2/Vs

Table 1.1: OLET Materials *(continued)*

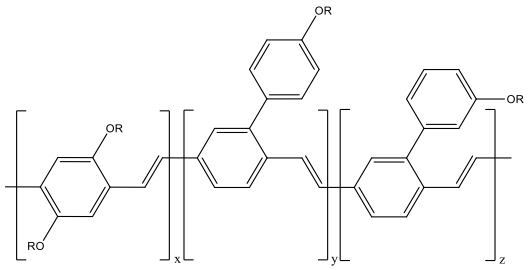 Super Yellow	Unipolar [25]	EQE = 0.15% luminescence = 2500 cdm^{-2}
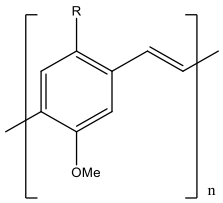	Unipolar [26]	μ_h = 0.14 cm^2/Vs luminescence = 112 cdm^{-2} EQE = 0.1%
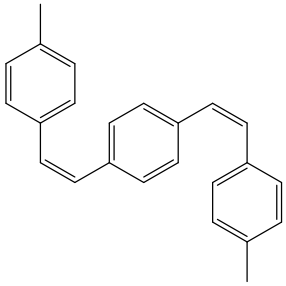 1,4-Bis(4-methylstyryl)benzene	Ambipolar [27]	φ_{PL} = 89%
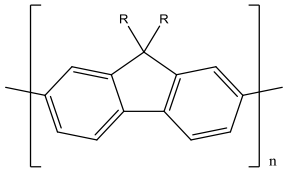 poly[9,9-di(ethylhexyl)-fluorene]	Unipolar [26]	μ_h = 0.16 cm^2/Vs luminescence = 137 cdm^{-2} EQE = 0.1%

Table 1.1: OLET Materials *(continued)*

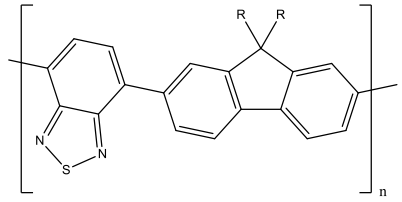	Ambipolar [28]	luminescence = 8000 cdm^{-2} EQE = 8%
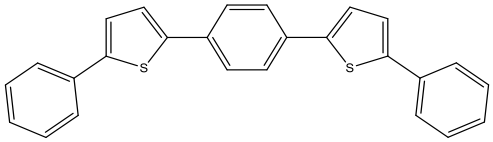 1,4-bis5-phenylthiophen-2-ylbenzene	Ambipolar [29]	φ_{PL} = 35% $\mu_h = 2.9 \times 10^{-1}$ cm^2/Vs $\mu_e = 6.7 \times 10^{-3}$ cm^2/Vs
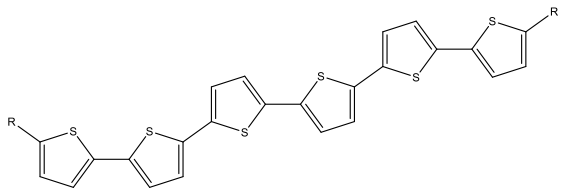 dihexylsexithiophene	Ambipolar [30]	$\mu_h = 2.2 \times 10^{-2}$ cm^2/Vs $\mu_e = 2.8 \times 10^{-3}$ cm^2/Vs
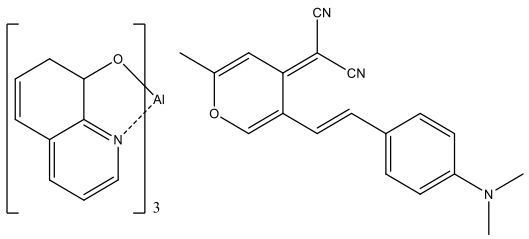	Unipolar [31]	EQE = 5%
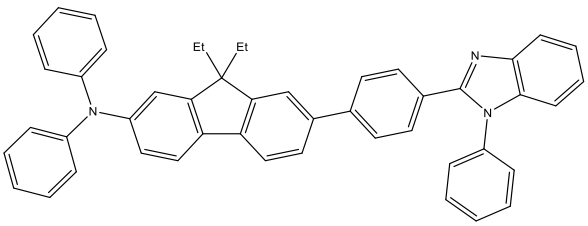	Unipolar [32]	EQE = 0.2%

Table 1.1: OLET Materials *(continued)*

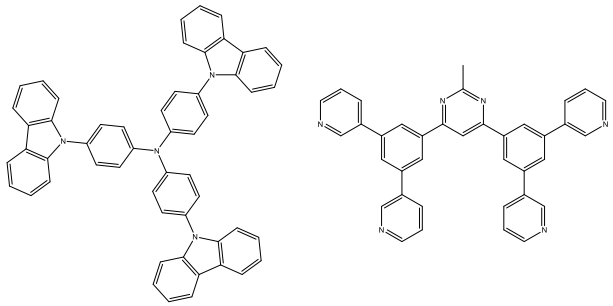	Unipolar [33]	EQE = 0.93% (TADF)
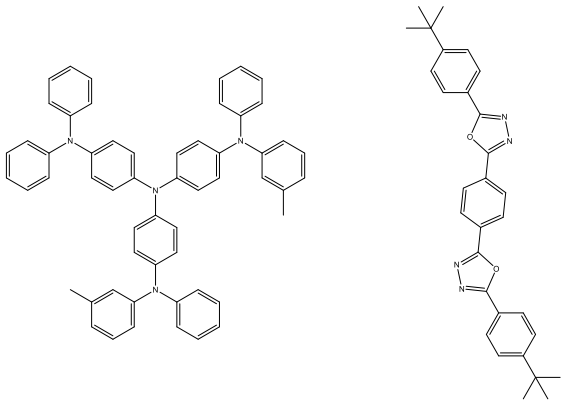	Unipolar [33]	EQE = 3.76% (TADF)
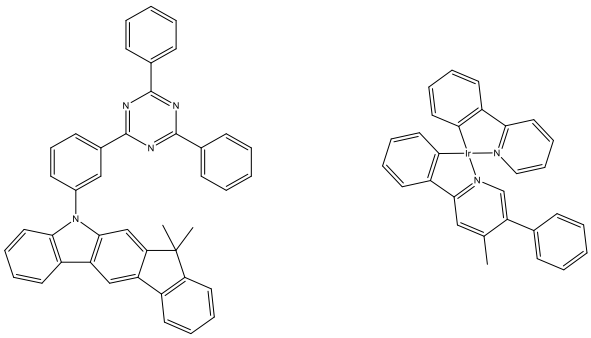	Ambipolar [34]	luminescence = 14500 cdm^{-2} EQE = 9%

1.5 Materials and Devices

In principle, the vast library of existing organic semiconductors can be potentially employed as different components in light-emitting devices. However, as explained above, a very

stringent set of requirements must be met before any material is employed as an active layer in a light-emitting device. First, the material needs to have an appropriate bandgap corresponding to red, green, and blue emission in the visible region of the electromagnetic spectrum. Second, it needs to have a high quantum yield of emission. If an organic system meets these requirements, it can be employed as an active layer in an OLED device. However, for an OLET device, the organic system in question needs adequate charge carrier mobility in addition to the first two constraints to be employed as an active layer. While a wide array of organic systems such as fluorene, spirobifluorene, phenylene-vinylene, biphenyl, acene, oligothiophene, thiophene-phenylene, and furan based moieties have been employed as active layers in OLET devices, we will be only focusing on those systems which were employed to elucidate major developments in this field (**Table 1.1**). For a more comprehensive list of organic systems, readers should refer elsewhere. [18,35,36]

1.5.1 Unipolar Device Materials

Materials for ambipolar charge transport were scarce in the early days of OLETs. However, those materials still produced weak light emission on the edges of the drain electrode in devices exhibiting unipolar hole transport. Moreover, the devices based on these systems exhibited very low external quantum (EQE) and luminescence efficiencies, most likely due to imbalanced charge recombination and exciton quenching at the drain electrode. [8,37,38] A classic example of a device based on such a system was a single-layered tetracene-based BG-BC OLET comprising of an interdigitated gold source and drain electrodes on a Si/SiO_2 substrate developed by Hepp in 2003. [8] The light emitted had a typical tetracene emission spectrum with the maxima at 540 nm. Simultaneously, the luminance and its efficiency in the device were found to be 45 cd m^{-2} and 0.0024 cd A^{-1}, respectively. As described previously, the device exhibited unipolar hole transport

as the tetracene HOMO and LUMO were such that the barrier for hole injection was only 0.3 eV, which could easily be overcome at room temperature. However, the electron injection barrier was 2.7 eV, which is impossible to surmount at room temperature. [8] The EQE of the device was very low (6.7×10^{-5} %), which was likely due to the strong intermolecular packing in small molecule tetracene.

To improve the viability of such materials, Namdas proposed to separate the processes of charge injection, transport, and emission into separate systems, and thus multi-layered OLETs were conceived. [25] This allowed them to use an optimized material for each process and improve the devices' active layer performance. Their bi-layered device included poly(2,5-bis(3-tetradecylthiophen2-yl)thieno[3,2-b] thiophene) as a hole transporting layer, which would then improve the device performance of polymer polyphenylenevinylene based super yellow emissive layer. Towards these ends, an asymmetric BG-TC device was fabricated with a hole injecting silver source electrode and an electron injecting calcium drain electrode exhibiting an EQE of 0.15% and peak luminescence of 2500 cd m^{-2}. Although they tried to circumvent the issue of electron injection by employing a low workfunction Ca drain electrode which was close in energy to the LUMO of super yellow, however, their super yellow polymer still exhibited unipolar characteristics with light emission near the edge of the drain electrode and still independent of the gate voltage.

In 2010, Capelli further explored the multilayer model towards improving active material performance in his p-channel/emitter/n-channel tri-layered symmetric BG-TC device with ITO gate, PMMA dielectric, and Au as source/drain electrodes. [31] This was the first time a trilayered structure was used in OLET devices. Here, they employed small molecule tris(8-hydroxyquinolinato)aluminium/4-(dicyanomethylene)-2-methyl-6-(p-dimethylaminostyryl) - 4H-pyran (Alq_3/DCM) host/guest system as an emissive layer sandwiched between quaterthiophenes

(DH-4T) and fluorinated quaterthiophenes (DFH-4T) as hole and electron transporting layers, respectively. The energy levels of the host/guest emissive layer were closely aligned with those of hole and electron transporting layers showing excellent energetic compatibility. Their Alq_3/DCM host/guest emissive system exhibited an EQE of 5% in their OLET device. This was twice more efficient than the optimized OLED of the same material and ten times more than any previously reported OLET at the time. More importantly, although their organic system was still unipolar (electron dominated), exhibiting emission near the drain electrode, the emission zone was somewhat controllable and could be spread out by controlling the gate voltage.

Besides asymmetric electrodes, symmetric but multifunctional electrodes composed of Magnesium and Aluminium have been employed by Adachi to improve the performance of unipolar small molecular 9,9-diethyl-N,N-diphenyl-7-(4-(1- phenyl-1H-benzoimidazol-2-yl)-phenyl)-9H-fluoren-2-amine blue light-emitting system. [32] Their unique device architecture was composed of a single active light-emitting layer. Although the material performance was relatively poor (EQE = 0.2%), the authors claimed magnesium's low work function facilitated electron injection. Moreover, they could control the light intensity and recombination zone in the active layer by varying the gate voltage.

Another significant development in the field was the use of conjugated polyelectrolytes (CPE) as an electron injection layer by the Heeger group. [26] Their p-type symmetric tri-layered device was composed of a hole transporting layer, an emissive layer, and poly[9′,9-bis[6′(*N*,*N*,*N*-trimethylammonium)hexyl]florene-*alt*-*co*-1,4- phenylene] with tetrakis(imidazoly)borate counterion ($PFN^+BIm_4^-$) as an electron injecting polyelectrolyte. This development was made possible by employing poly[2-methoxy-5-(2′-ethyhexyloxy-1,4-phenylenevinylene)] (MEH-PPV), phenyl-substituted poly(para-phenylene vinylene) copolymer (Superyellow), and poly[9,9-

di(ethylhexyl)fluorene] (PFO) polymers to achieve red, yellow, and blue emission respectively. Additionally, it was determined that the thickness of the CPE layer was critical for device performance.

Traditional emissive materials only utilize singlet excitons, which only account for 25% of all excitons, for light emission. To harvest the remainder 75% of excitons, one must employ thermally activated delayed fluorescence materials (TADF) in which the triplet state is energetically close to the singlet state. One such material is 4,4′,4″-tris(N-carbazolyl)-triphenylamine:bis-4,6-(3,5-di-3-pyridylphenyl)-2-methyl pyrimidine, which was first employed by Liu in their OLET device. [33] Their device exhibited an exciton utilization efficiency of 60.3% with a maximum EQE of 0.93% despite a large hole injection barrier. To lower the hole injection barrier, they developed 4,4′,4″-tris(N-3-methyl phenyl-N-phenylamino)triphenylamine as a donor, and (1,3-bis[2-(4-tert-butyl phenyl)-1,3,4-oxadiazo-5-yl]-benzene) as an acceptor based TADF emitter. This improved the exciton utilization efficiency to 74.3% with a maximum EQE of 3.76% and a brightness exceeding 1100 cdm^{-2}. This device even outperformed their corresponding OLEDs based on the same emitting material.

1.5.2 Ambipolar Device Materials

Although unipolar OLET devices have made progress in recent years, they have to meet the bare minimum threshold for commercialization. A large electron injection barrier leads to imbalanced electron-hole transport and forces exciton formation near the drain electrode. This leads to exciton quenching at the metal contacts and a low EQE for the material. For this reason, device optimization towards achieving ambipolar charge transport in active emissive layers is

essential. Materials in such devices can potentially accumulate both electrons and holes and, by extension, exhibit both n-type and p-type behavior in a single device.

The first attempts at ambipolar OLETs were made around 2005 by Zaumseil in the Sirringhaus group at Cavendish Laboratory in Cambridge. [39,40] They demonstrated that hydroxyl groups in SiO_2 dielectric at semiconductor-dielectric interface led to electron trapping. This was why most organic systems previously showed only p-type behavior in OFETs. By replacing SiO_2 with a hydroxyl-free dielectric led to increased electron mobilities in several polyfluorenes and dialkyl-substituted poly(p-phenylenevinylene) active layer copolymers. Based on this, they then fabricated a BG-TC LET device with multifunctional gold/calcium electrodes. Photoluminescent poly(2- methoxy-5-(3,7-dimethyloctoxy)-p-phenylene-vinylene) with an emission maximum of around 660 nm and PLQY = 10% was the emissive layer while SiO_2 dielectric was passivated with a benzocyclobutene derivative as a buffer dielectric. By varying the gate voltage and the source-drain bias, they were able to move the recombination/emission zone across the entire active layer channel length. Even though their hole/electron mobilities were balanced, the EQE of their device was relatively low (0.35%).

The most promising materials for light emission are based on fluorene. For example, poly(9,9-di-n-octylfluorene-alt-benzothiadiazole (F8BT) has been investigated in detail because it has high photoluminescent quantum efficiency in solid-state (50-60%), high electron mobility, and bright green emission. [28,41,42] Employing a TG-BC device architecture, the Sirrighaus group has employed this polymer to demonstrate several concepts.

Firstly, they developed TG-BC architecture that doesn't depend on the vacuum deposition of a high and low work function metal for an efficient hole and electron injection, hence improving

the devices' shelf-life by eliminating reactive low work function metals. Also, TG architecture allows for several polymer gate dielectrics to be employed that need not be crosslinked and are simply solution-processed onto the emissive F8BT semiconductor layer. Since the gate and dielectric are coated over the F8BT emissive layer, they can potentially isolate the emissive layer from environmental degradation. [42]

Secondly, they could bypass the electron injection barrier by solution patterning on gold source/drain electrodes a layer of an n-type zinc oxide layer. In addition to avoiding unstable low work function metals, their modified device structure significantly lowered the electron threshold voltages, improved ambipolar currents, and by extension, light emission intensities in the F8BT system by several orders of magnitude. Critically, they were able to keep the device fabrication temperature under 150 °C, which was well below the degradation temperature of their F8BT emissive polymer system. [41]

Lastly, employing the same F8BT emissive layer, their group achieved an EQE of 8% and the highest luminescence efficiency of 28 CdA^{-1}. These values were then one of the highest reported for LETs and comparable to the state of the art OLEDs. Their OLETs had extremely high current densities (400 mA cm^{-2}) and brightness (8000 cd m^{-2}). More impressively, they achieved these results without employing any additional electron/hole injecting/transporting layers or low work function electrodes. They quantified exciton quenching as a function of position and charge concentration along the entirety of the channel and hence providing direct evidence for low exciton-polaron quenching. [28]

Among other factors affecting light emission, the effect of morphology and microstructure on light emission has been interesting. Employing F8BT as a model system, Zaumseil directly

visualized the current density by studying the width and shape of the emission zone. [43,44] For a polycrystalline film, the electroluminescent emission zone was grainy while photoluminescence was uniform. Moreover, depending on whether the polymer films were aligned parallel or perpendicular to the charge transport direction, the emission zone was found to be wide or narrow, respectively. Another factor affecting light emission is the molecular structure. For instance, employing thieno(bis)imide (TBI) moiety as an end group in unipolar non-emissive oligothiophene makes the resulting molecule both ambipolar and emissive, albeit only weakly. [45]

Although not practically useful, several materials, such as tetracene, pentacene, and rubrene, have been employed in single-crystal devices to study charge transport, electroluminescence, and field-effect. The first genuinely ambipolar single-crystal OLET device was developed by Takahashi in 2007. [46] This work was followed by another study by the same group, but this time on rubrene instead of tetracene. Both devices employed silver paste as source/drain electrodes, PMMA as the gate dielectric, and doped silicon as the gate. Both their devices exhibited similar results and very low external quantum efficiencies. [24] Low intrinsic photoluminescence and strong packing in tetracene and rubrene were detrimental to their device performance. To address this issue, Isawa employed a 1,4-bis(5-phenylthiophen-2-yl)benzene active layer system in a single crystal device. This material emitted green light with a photoluminescence efficiency of 35%, which was naturally confined within the crystal. Here, only the edges were luminescent, and this was attributed to perfectly aligned transition dipole moments. [29]

Among single crystal systems for OLET devices, organic photovoltaic materials have attracted considerable attention. For instance, Adachi employed 1,4-bis(4-methylstyryl)benzene (CH_3-P3V2) single crystals with a photoluminescent quantum efficiency of 89 % in a single crystal

OPV device. [27] This proves that high photoluminescence quantum yield is possible in densely packed single crystals in some instances. This was most likely due to a relatively high energy level of the triplet state relative to the singlet, which prevents singlet fission. While their device exhibited a relatively high hole/electron mobilities of 0.1/0.01 $cm^2V^{-1}s^{-1}$, respectively, hole mobility was an order of magnitude higher than the electron mobility. To address this issue, they increased the conjugation length of their OPV active layer system from three (P3V2) to four (P4V3) phenylene rings, which balanced electron/hole mobilities to around 0.11/0.12 $cm^2V^{-1}s^{-1}$, respectively. [47] A strong edge emission was observed in both cases, indicating strong optical waveguiding.

Among the best performing single component device was fabricated by Qin in 2019. [48] This was achieved by using 2,6-diphenylanthracene (DPA) and 2,6-di(2-naphthyl) anthracene (dNaAnt) single crystals as materials for the active layer and employing oblique incidence evaporation technique for balanced and efficient charge transport. For DPA OLETs, the EQE value was 1.61%, with a brightness of 1210 cd m^{-2} and average electron and hole mobilities of 0.07 cm^2 V^{-1} s^{-1} and 0.79 cm^2 V^{-1} s^{-1}, respectively. On the other hand, for the dNaAnt OLETs, the EQE value was 1.75%, with a brightness of 3180 cd m^{-2} and average electron and hole mobilities of 0.39 cm^2 V^{-1} s^{-1} and 0.29 cm^2 V^{-1} s^{-1}, respectively. These results can be attributed to the excellent ambipolar transport performance allowing for efficient electron and hole recombination, the materials' high mobility emissive characteristics, and long-range molecular order of organic single-crystals.

While single crystal devices offer a robust model to study complex optoelectronic processes, they are not useful for large-scale mass manufacturing, which is essential for commercializing any system. On the other hand, single-layered devices exhibit less than optimal

optoelectronic performances since it is incredibly unlikely, if not impossible, for a single material to check all the requisite optoelectronic property boxes. Multi-layered devices offer a way around this problem, where architectural simplicity is sacrificed for device performance. In this case, it is possible to employ multiple systems where each of them is optimized for a specific purpose.

One of the first ambipolar multi-layered OLETs was fabricated by the Marks group in 2006. Attempting a bi-layered OFET assembly, the authors tried to determine the most effective way to structure the layers to achieve maximum mobility and electroluminescence. They employed a p-type ω-dihexylquaterthiophene (DHT4) layer at the bottom and an n-type *N*,*N*′-ditridecylperylene-3,4,9,10-tetracarboxylic diimide (P13) layer at the top to fabricate their bilayered device and successfully achieved electroluminescence as a consequence of balanced hole/electron mobilities. Inversion of this configuration, however, led to growth compatibility issues and significant loss in hole mobility. The best performance is not necessarily achieved based on the constituents' single-layer performance; instead, growth compatibility between the two organic layers is essential to achieve a good performance. While the emission zone wasn't discussed, it was most likely at the interface between the layers near the drain electrode. [49]

Muccini published another study that improved upon the same concept. [50] Using two different configurations to structure the active layer, the carrier mobilities were determined for several different combinations of p-type (pentacene, DH4T, T5) and n-type materials (P13). Here T5 is α-quinquethiophene, while DH4T and P13 have been described previously. One configuration is a bi-layered heterojunction where electroluminescence occurs around the junctions due to the spatial separation of the electron and hole transport layers. The best results in this configuration were calculated with the DH4T/P13 combination with both carrier mobilities around 3×10^{-2} cm^2 V^{-1} s^{-1}. The other configuration is a bulk heterojunction where both p and

n-type molecules co-evaporate on the same substrate to ensure they are mixed together. As a result, the electron and hole transport regions are intermixed and allow recombination to occur anywhere within the active layer. The carrier mobilities are much lower in this case due to the lack of a continuous surface between the dielectric and the charge transport layer. After experimenting with varying ratios of T5 and P13, the most balanced charge transport was achieved with mobilities in the lower ranges of 10^{-3} cm^2 V^{-1} s^{-1}.

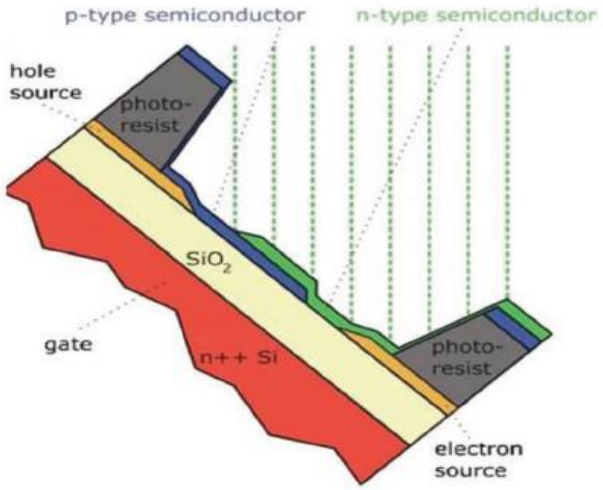

Figure 1.5: OLET structure. Reprinted with permission from Ref. [51]

Vausser later improved upon this bi-layer concept by depositing n-type N,N′N,N′-ditridecylperylene-3,4,9,10-tetracarboxylic diimide (PTCDI-$C_{13}H_{27}$) layer on top of the p-type 1,4-bis(octyloxy)-2,5-bis[(E)(E)-4-(E)(E)-styrylstyryl]benzene (O-octyl-OPV5) at an angle such that they overlapped only in the middle of the device (**Figure 1.5**). In this configuration, the device would be forced to emit in the middle of the channel away from the drain electrode, thereby improving the electroluminescence quantum yield. [51]

In the previous examples, only one of the bilayers was emissive. However, as Feldmeier demonstrated, this need not be the case, who fabricated OLETs employing tetracene/ditetracene emissive layers with gold and calcium electrodes. [23] In a double-layered setup, it is possible to

achieve emissions varying in color. This is done by spatially manipulating the recombination zone via applied voltages. Changing the gate bias allows the recombination to occur in either of the two layers. With a purely ditetracene-based FET, the hole mobility is observed to be 0.126 $cm^2\ V^{-1}\ s^{-1}$, while the electron mobility is 0.033 $cm^2\ V^{-1}\ s^{-1}$, with a small ambipolar window between 65 to 75 V and visible light emission in the red range at 580 nm. On the other hand, a pure tetracene-based FET has hole and electron mobilities of 1.12×10^{-3} and 0.435 $cm^2\ V^{-1}\ s^{-1,}$ respectively. The visible light emission occurs in the green range at 530 nm. Finally, using a combination of tetracene and ditetracene layers, ambipolarity is achieved between 71 to 83 V, and the resulting emission occurs as a combination of its two constituents. The mixed emission spectrum results from the recombination zones' vertically varying spatial location controlled by the gate voltage. Here, the positioning of the energy levels is such that electrons can easily move from tetracene (green emission) into diterracene (red emission). In contrast, holes cannot move the other way round. This is why the region and the color of the recombination zone can be modulated by applied voltages, which is essential in multi-color devices.

In another significant development, Choi optimized the neutral cluster beam deposition method to construct dihexylsexithiophene (DH6T) and P13 based OLET at room temperature. [30] Their device had improved surface morphology, crystalline structures, and packing density, all of which are impossible via conventional vapor deposition and solution-processing methods. Various groups then employed this same technique to fabricate P13/tetracene, pentacene/P13/2,5-bis(4-biphenyl) thiophene (BP1T, protective layer), and P13/CuPc based devices. [36]

The best performing device to date is based on a tri-layered structure employing a BG-TC architecture for one electrode and BG-BC architecture for another electrode. [34] The materials used and their energy levels are shown in **Figure 1.6**. They fabricated several devices based on high-*k*

polymer crosslinked poly(vinyl alcohol) (C-PVA) and perfluoro(1-butenyl vinyl ether) polymer (CYTOP) modified C-PVA dielectric layers and were able to achieve a brightness of 14 500 cdm^{-2} and an external quantum efficiency of 9%. This demonstrates the potential of multi-layered devices towards high optoelectronic performance.

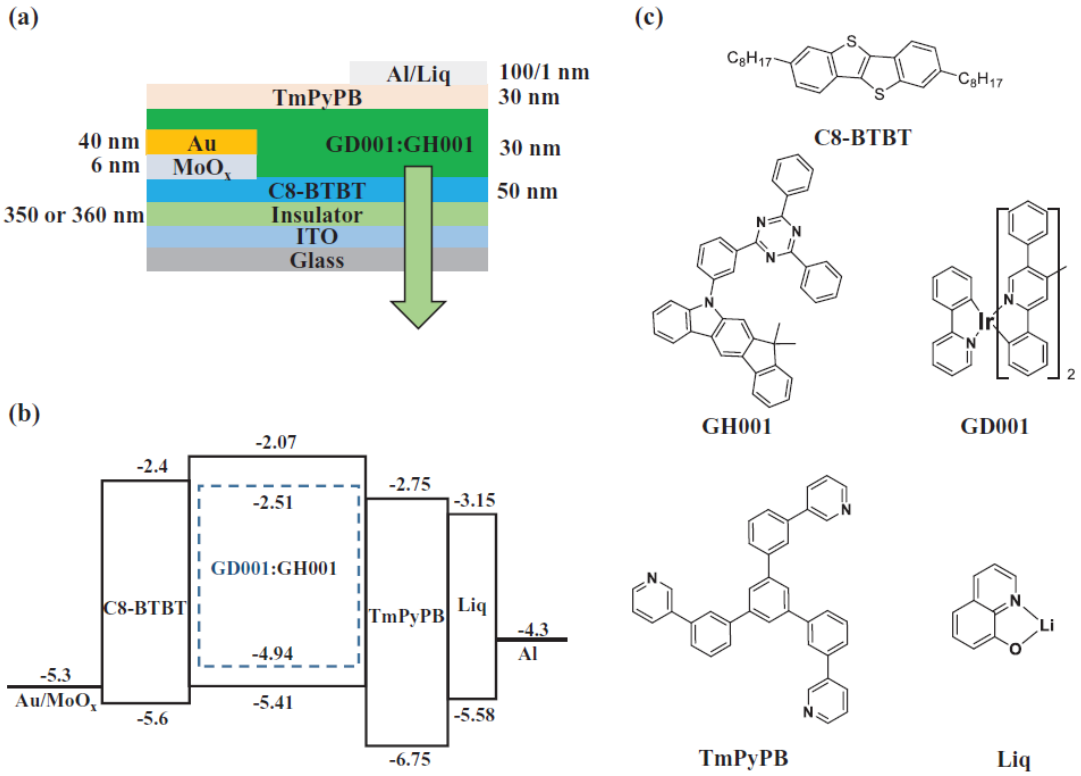

Figure 1.6: OLET structure, materials and energy levels. Reprinted with permission from Ref. [34]

All the previous examples in this paper focused on traditional organic materials and device architectures as components for OLET applications. However, this need not be the case. For instance, using a single-wall carbon nanotube network, it is possible to integrate an OLED with a vertical FET to create a carbon nanotube enabled vertical field-effect transistor (CN-VOLET). [52] The nanotubes act as a source electrode, and the CN-VFET structure is responsible for hole injection in the OLED layers. The OLED is connected to a drain electrode on the other end. The device was fabricated for each of the three primary colors with Iridium(III)bis(2-methyldibenzo[f,h]quinoxaline) (acetylacetonate), F*ac*-tris(2-phenylpyridinato) iridium(III), and

Bis[(4,6-di-fluorophenyl)-pyridinate-N,C2′]picolinate, as red, green, and blue emitters respectively. With an operational gate voltage of ±3 V for each color, the luminance crosses the 500 cd/m^2 mark at drain voltages of -6.8 V (red), -4.9 V(green), and -5.7 V(blue). The contrast ratios approach a factor of 10^4. CN-VOLET here operates at 98% current efficiency compared to their corresponding OLEDs, with the transistor layer contributing very little to the parasitic power consumption (19, 6, and 15% of total power consumption in red, green, and blue pixels, respectively).

Another example used natural Fibroin, the constituent protein of silk, to fabricate electronic and optoelectronic devices such as OFETs and OLETs. [53] One p-type and one n-type organic thin-film transistor was fabricated using DH4T and P13, respectively. The Fibroin silk was used as a dielectric in both transistors, and its performance was compared against PMMA and SiO_2. The silk dielectric results in negligible hysteresis, and therefore low charge trapping, especially for electrons. With electron mobility of 4×10^{-2} and hole mobility of 1.3×10^{-2}, the mobility values for silk are comparable to that of PMMA and SiO_2. For the silk-P13 transistor, the voltage threshold measured is one order of magnitude smaller than a standard OFET. The on-off ratio is in the order of 10^4. The light emission intensity was 100nW at $V_{g\text{-}s}$= $V_{d\text{-}s}$= 90 V. This was the first time that electroluminance was observed from a silk-based device.

Vertical organic light-emitting transistors (VOLET) have also been employed. [54] For this study, the VOLET was designed by combining a capacitor and a light-emitting polymer (LEP) via a common (source) electrode. Aluminum was used as the source electrode to create a large injection barrier between the LEP and the source, such that at zero gate voltage, no injection of electrons occurs. The output characteristics suggest that gate modulation can significantly lower the electron injection barrier and affect light emission. It is essential to keep the source electrode

restricted to a certain thickness in order to keep the gate modulation effect. This device can potentially have applications in the fabrication of active-matrix displays.

Another example of the same concept is that of a semi-transparent VOLET. [55] This was done by inserting an OLED in the channel of a thin-film transistor with transparent electrodes. The source electrode was made out of porous ITO, which played a significant role in enhancing the luminescent characteristics of the device. The maximum luminance was observed to be 500 cd/m^2, and the luminance modulation was in the order of 10^4. The light was emitted from both the top and the bottom of the device, though the emission color varied slightly due to the thicker layers that the light had to penetrate through on the bottom end. The top emission wavelength peak was around 520 nm, while the bottom peak is shifted slightly to 525 nm. As for the current efficiency, increasing the gate voltage from 14 V to 18 V increases the efficiency from 3.6 cd/A to 13.1 cd/A.

1.6 Conclusion

The past few decades have witnessed remarkable developments in the field of organic optoelectronics. Every conceivable optoelectronic device has its organic counterpart, which in some cases, match or even exceed the performance metrics of the original device. While considerable research efforts have been allocated towards organic light-emitting transistor devices, they have yet to reach their promised potential. For instance, the current state of the art OLET device has managed to achieve an efficiency of only 9%, whereas OLED devices already operate at efficiencies of over 50%. [56] Considerable resources need to be devoted towards achieving high mobility, large $I_{ON/OFF}$ ratio, low operating-voltage, balanced carrier injection, high brightness, high EQE, and tunable electroluminescent zone to realize the full potential of such systems.

Most OLET devices reported in the literature are fabricated employing OLED materials instead. This remains a key issue since OLED materials generally don't exhibit a high charge carrier mobility, which is fine since these charge carriers have to travel distances in tens of nanometers. However, in the case of OLETs, low mobility becomes a significant problem since the travel distance can be in tens of micrometers. In theory, this issue could be addressed by employing a material that exhibits both high hole/electron mobilities as well as high photoluminescent quantum efficiency in solid-state. Very few such materials are available, and it is a significant challenge to design new materials as increased mobility is usually achieved only at the expense of luminescence and vice versa. One way to address this issue is to employ semi-ladder polymers that offer rigidity and reduced vibrational modes necessary for emission, planarity, and improved orbital overlap essential for charge carrier mobility and solution processability, which is the topic that this thesis is focused on. Another solution to this issue is the use of multi-layered devices where each layer is specifically tailored for a specific purpose. Therefore, multi-layered devices in concert with semi-ladder polymers might just be the most optimal solution, especially if such devices can be made solution-processable.

The following chapters will demonstrate the potential offered by semi-ladder polymers in LET devices. We will describe the synthesis, characterization, and, most importantly, the device performance of our state-of-the-art semi-ladder polymers. We will provide evidence that semi-ladder polymers employed in solution-processed multi-layered devices offer adequate mobility and impressive EQE. We will describe the structure-property relationship, which will prove pivotal as OLET devices move ever closer to commercialization.

1.7 References

(1) Kvarnström, C. György Inzelt, Conducting Polymers. A New Era in Electrochemistry: Series: Monographs in Electrochemistry, Editor: Fritz Scholz, 2008, XII, 282 p, ISBN: 978-3-540-75929-4, 139.05 €. *J. Solid State Electrochem.* **2010**.

(2) Kallmann, H.; Pope, M. Positive Hole Injection into Organic Crystals. *The Journal of Chemical Physics*. 1960.

(3) Kallmann, H.; Pope, M. Bulk Conductivity in Organic Crystals. *Nature* **1960**.

(4) Shirakawa, H.; Louis, E. J.; MacDiarmid, A. G.; Chiang, C. K.; Heeger, A. J. Synthesis of Electrically Conducting Organic Polymers: Halogen Derivatives of Polyacetylene, (CH) X. *J. Chem. Soc. Chem. Commun.* **1977**, No. 16, 578.

(5) Wei, A.; Zempo, Y. Focus on Organic Electronics. *Sci. Technol. Adv. Mater.* **2014**, *15* (4), 040301.

(6) Tang, C. W.; Vanslyke, S. A. Organic Electroluminescent Diodes. *Appl. Phys. Lett.* **1987**, *51* (12), 913–915.

(7) Tsumura, A.; Koezuka, H.; Ando, T. Macromolecular Electronic Device: Field-Effect Transistor with a Polythiophene Thin Film. *Appl. Phys. Lett.* **1986**, *49* (18), 1210–1212.

(8) Hepp, A.; Heil, H.; Weise, W.; Ahles, M.; Schmechel, R.; von Seggern, H. Light-Emitting Field-Effect Transistor Based on a Tetracene Thin Film. *Phys. Rev. Lett.* **2003**, *91* (15), 157406.

(9) Dou, L.; Liu, Y.; Hong, Z.; Li, G.; Yang, Y. Low-Bandgap Near-IR Conjugated Polymers/Molecules for Organic Electronics. *Chem. Rev.* **2015**, *115* (23), 12633–12665.

(10) Embracing the Organics World. *Nat. Mater.* **2013**, *12* (7), 591–591.

(11) Facchetti, A. Organic Semiconductors: Made to Order. *Nat. Mater.* **2013**, *12* (7), 598–600.

(12) Yuan, D.; Sharapov, V.; Liu, X.; Yu, L. Design of High-Performance Organic Light-Emitting Transistors. *ACS Omega*. 2019.

(13) Yu, L.; Chen, M.; Dalton, L. R. Ladder Polymers: Recent Developments in Syntheses, Characterization, and Potential Applications as Electronic and Optical Materials. *Chemistry of Materials*. 1990, pp 649–659.

(14) Fukazawa, A.; Yamaguchi, S. Ladder π-Conjugated Materials Containing Main-Group Elements. *Chemistry - An Asian Journal*. 2009, pp 1386–1400.

(15) Nacci, C.; Ample, F.; Bleger, D.; Hecht, S.; Joachim, C.; Grill, L. Conductance of a Single Flexible Molecular Wire Composed of Alternating Donor and Acceptor Units. *Nat. Commun.* **2015**, *6* (May), 7397.

(16) Osaka, I.; Takimiya, K. Naphthobischalcogenadiazole Conjugated Polymers: Emerging Materials for Organic Electronics. *Adv. Mater.* **2017**, *29* (25), 1–4.

(17) Shen, Y.; Chen, C.-F. Helicenes: Synthesis and Applications. *Chem. Rev.* **2012**, *112* (3), 1463–1535.

(18) Zhang, C.; Chen, P.; Hu, W. Organic Light-Emitting Transistors: Materials, Device Configurations, and Operations. *Small*. 2016, pp 1252–1294.

(19) Muccini, M.; Toffanin, S. *Organic Light-Emitting Transistors: Towards the Next Generation Display Technology*; 2016.

(20) Zaumseil, J.; Donley, C. L.; Kim, J.-S.; Friend, R. H.; Sirringhaus, H. Inside Front Cover: Efficient Top-Gate, Ambipolar, Light-Emitting Field-Effect Transistors Based on a Green-Light-Emitting Polyfluorene (Adv. Mater. 20/2006). *Adv. Mater.* **2006**.

(21) Zaumseil, J. Recent Developments and Novel Applications of Thin Film, Light-Emitting Transistors. *Advanced Functional Materials*. 2019.

(22) Kymissis, I.; Dimitrakopoulos, C. D.; Purushothaman, S. Erratum: High-Performance Bottom Electrode Organic Thin-Film Transistors (IEEE Trans. Electron Devices (2001) 48 (1060-1064)). *IEEE Transactions on Electron Devices*. 2001.

(23) Feldmeier, E. J.; Schidleja, M.; Melzer, C.; Von Seggern, H. A Color-Tuneable Organic Light-Emitting Transistor. *Adv. Mater.* **2010**.

(24) Takahashi, T.; Takenobu, T.; Takeya, J.; Iwasa, Y. Ambipolar Organic Field-Effect Transistors Based on Rubrene Single Crystals. *Appl. Phys. Lett.* **2006**.

(25) Namdas, E. B.; Ledochowitsch, P.; Yuen, J. D.; Moses, D.; Heeger, A. J. High Performance Light Emitting Transistors. *Appl. Phys. Lett.* **2008**.

(26) Seo, J. H.; Namdas, E. B.; Gutacker, A.; Heeger, A. J.; Bazan, G. C. Solution-Processed Organic Light-Emitting Transistors Incorporating Conjugated Polyelectrolytes. *Adv. Funct. Mater.* **2011**.

(27) Nakanotani, H.; Kabe, R.; Yahiro, M.; Takenobu, T.; Iwasa, Y.; Adachi, C. Blue-Light-Emitting Ambipolar Field-Effect Transistors Using an Organic Single Crystal of 1,4-Bis(4-Methylstyryl)Benzene. *Appl. Phys. Express* **2008**.

(28) Gwinner, M. C.; Kabra, D.; Roberts, M.; Brenner, T. J. K.; Wallikewitz, B. H.; McNeill,

C. R.; Friend, R. H.; Sirringhaus, H. Highly Efficient Single-Layer Polymer Ambipolar Light-Emitting Field-Effect Transistors. *Adv. Mater.* **2012**.

(29) Yomogida, Y.; Takenobu, T.; Shimotani, H.; Sawabe, K.; Bisri, S. Z.; Yamao, T.; Hotta, S.; Iwasa, Y. Green Light Emission from the Edges of Organic Single-Crystal Transistors. *Appl. Phys. Lett.* **2010**.

(30) Seo, H. S.; Zhang, Y.; An, M. J.; Choi, J. H. Fabrication and Characterization of Air-Stable, Ambipolar Heterojunction-Based Organic Light-Emitting Field-Effect Transistors. *Org. Electron.* **2009**.

(31) Capelli, R.; Toffanin, S.; Generali, G.; Usta, H.; Facchetti, A.; Muccini, M. Organic Light-Emitting Transistors with an Efficiency That Outperforms the Equivalent Light-Emitting Diodes. *Nat. Mater.* **2010**.

(32) Ke, T. H.; Gehlhaar, R.; Chen, C. H.; Lin, J. T.; Wu, C. C.; Adachi, C. High Efficiency Blue Light Emitting Unipolar Transistor Incorporating Multifunctional Electrodes. *Appl. Phys. Lett.* **2009**.

(33) Song, L.; Hu, Y.; Liu, Z.; Lv, Y.; Guo, X.; Liu, X. Harvesting Triplet Excitons with Exciplex Thermally Activated Delayed Fluorescence Emitters toward High Performance Heterostructured Organic Light-Emitting Field Effect Transistors. *ACS Appl. Mater. Interfaces* **2017**.

(34) Chen, H.; Xing, X.; Miao, J.; Zhao, C.; Zhu, M.; Bai, J. W.; He, Y.; Meng, H. Highly Efficient Flexible Organic Light Emitting Transistor Based on High-k Polymer Gate Dielectric. *Adv. Opt. Mater.* **2020**.

(35) Cicoira, F.; Santato, C. Organic Light Emitting Field Effect Transistors: Advances and Perspectives. *Adv. Funct. Mater.* **2007**.

(36) Liu, C. F.; Liu, X.; Lai, W. Y.; Huang, W. Organic Light-Emitting Field-Effect Transistors: Device Geometries and Fabrication Techniques. *Advanced Materials*. 2018.

(37) Ahles, M.; Hepp, A.; Schmechel, R.; Von Seggern, H. Light Emission from a Polymer Transistor. *Appl. Phys. Lett.* **2004**.

(38) Sakanoue, T.; Fujiwara, E.; Yamada, R.; Tada, H. Visible Light Emission from Polymer-Based Field-Effect Transistors. *Appl. Phys. Lett.* **2004**.

(39) Chua, L. L.; Zaumseil, J.; Chang, J. F.; Ou, E. C. W.; Ho, P. K. H.; Sirringhaus, H.; Friend, R. H. General Observation of N-Type Field-Effect Behaviour in Organic Semiconductors. *Nature* **2005**.

(40) Zaumseil, J.; Friend, R. H.; Sirringhaus, H. Spatial Control of the Recombination Zone in an Ambipolar Light-Emitting Organic Transistor. *Nat. Mater.* **2006**.

(41) Gwinner, M. C.; Vaynzof, Y.; Banger, K. K.; Ho, P. K. H.; Friend, R. H.; Sirringhaus, H.

Solution-Processed Zinc Oxide as High-Performance Air-Stable Electron Injector in Organic Ambipolar Light-Emitting Field-Effect Transistors. *Adv. Funct. Mater.* **2010**.

(42) Zaumseil, J.; Donley, C. L.; Kim, J. S.; Friend, R. H.; Sirringhaus, H. Efficient Top-Gate, Ambipolar, Light-Emitting Field-Effect Transistors Based on a Green-Light-Emitting Polyfluorene. *Adv. Mater.* **2006**.

(43) Zaumseil, J.; Kline, R. J.; Sirringhaus, H. Electroluminescence Imaging and Microstructure of Organic Light-Emitting Field-Effect Transistors. *Appl. Phys. Lett.* **2008**.

(44) Zaumseil, J.; Groves, C.; Winfield, J. M.; Greenham, N. C.; Sirringhaus, H. Electron-Hole Recombination in Uniaxially Aligned Semiconducting Polymers. *Adv. Funct. Mater.* **2008**.

(45) Melucci, M.; Favaretto, L.; Zambianchi, M.; Durso, M.; Gazzano, M.; Zanelli, A.; Monari, M.; Lobello, M. G.; De Angelis, F.; Biondo, V.; et al. Molecular Tailoring of New Thieno(Bis)Imide-Based Semiconductors for Single Layer Ambipolar Light Emitting Transistors. *Chem. Mater.* **2013**.

(46) Takahashi, T.; Takenobu, T.; Takeya, J.; Iwasa, Y. Ambipolar Light-Emitting Transistors of a Tetracene Single Crystal. *Adv. Funct. Mater.* **2007**.

(47) Nakanotani, H.; Saito, M.; Nakamura, H.; Adachi, C. Highly Balanced Ambipolar Mobilities with Intense Electroluminescence in Field-Effect Transistors Based on Organic Single Crystal Oligo(p -Phenylenevinylene) Derivatives. *Appl. Phys. Lett.* **2009**.

(48) Qin, Z.; Gao, H.; Liu, J.; Zhou, K.; Li, J.; Dang, Y.; Huang, L.; Deng, H.; Zhang, X.; Dong, H.; et al. High-Efficiency Single-Component Organic Light-Emitting Transistors. *Adv. Mater.* **2019**.

(49) Dinelli, F.; Capelli, R.; Loi, M. A.; Murgia, M.; Muccini, M.; Facchetti, A.; Marks, T. J. High-Mobility Ambipolar Transport in Organic Light-Emitting Transistors. *Adv. Mater.* **2006**.

(50) Capelli, R.; Dinelli, F.; Loi, M. A.; Murgia, M.; Zamboni, R.; Muccini, M. Ambipolar Organic Light-Emitting Transistors Employing Heterojunctions of n-Type and p-Type Materials as the Active Layer. *J. Phys. Condens. Matter* **2006**.

(51) De Vusser, S.; Schols, S.; Steudel, S.; Verlaak, S.; Genoe, J.; Oosterbaan, W. D.; Lutsen, L.; Vanderzande, D.; Heremans, P. Light-Emitting Organic Field-Effect Transistor Using an Organic Heterostructure within the Transistor Channel. *Appl. Phys. Lett.* **2006**.

(52) McCarthy, M. A.; Liu, B.; Donoghue, E. P.; Kravchenko, I.; Kim, D. Y.; So, F.; Rinzler, A. G. Low-Voltage, Low-Power, Organic Light-Emitting Transistors for Active Matrix Displays. *Science (80-.).* **2011**.

(53) Capelli, R.; Amsden, J. J.; Generali, G.; Toffanin, S.; Benfenati, V.; Muccini, M.; Kaplan, D. L.; Omenetto, F. G.; Zamboni, R. Integration of Silk Protein in Organic and Light-

Emitting Transistors. *Org. Electron.* **2011**.

(54) Xu, Z.; Li, S. H.; Ma, L.; Li, G.; Yang, Y. Vertical Organic Light Emitting Transistor. *Appl. Phys. Lett.* **2007**.

(55) Yu, H.; Ho, S.; Barange, N.; Larrabee, R.; So, F. Semi-Transparent Vertical Organic Light-Emitting Transistors. *Org. Electron.* **2018**.

(56) Song, J.; Kim, K. H.; Kim, E.; Moon, C. K.; Kim, Y. H.; Kim, J. J.; Yoo, S. Lensfree OLEDs with over 50% External Quantum Efficiency via External Scattering and Horizontally Oriented Emitters. *Nat. Commun.* **2018**.

Chapter 2

Developing Linear Semi-Ladder Polymer Systems for use in Multi-Layered OLET Devices

2.1 Background

The last chapter of this thesis briefly described research progress in organic optoelectronic systems and the motivation behind pursuing studies in several classes of organic optoelectronic devices. As a recap, the reasons behind the trend towards organic systems are listed here as well: Firstly, organic systems offer immeasurable opportunities for tuning their optoelectronic properties by structural modifications. Secondly, organic systems are both lightweight and mechanically flexible, and thus these materials can be easily processed onto flexible substrates of varying architectural complexity. Thirdly, organic systems can be solution-processed and made compatible with the modern printing electronics industry. [1–5]

Among the most promising optoelectronic devices that employ organic systems is an organic light-emitting transistor (OLET). First developed by Hepp in 2003, OLET has come a long way since. [6] Already in 2006, the Sirringhaus group in Cambridge had achieved efficiencies of over 8%. [7] Since then, several research groups have tried and failed to move past this efficiency barrier. Only recently, one group achieved an external quantum efficiency (EQE) of 9%. [8] There

is a reason behind the lack of progress in this area. EQE is a function of photoluminescence and charge carrier mobility in solid-state, and improving one necessarily diminishes the other because of reasons described in the previous chapter.

The previous chapter describes a few ways to address this issue. The first approach involves using multi-layered devices where charge injection, charge transport, and emission functionalities are separated across different layers. It allows each layer to be tailored for a specific purpose. The second approach involves the use of semi-ladder polymers as active layers in OLET devices. This approach can potentially allow us to access reduced vibrational modes, extended conjugation, and improved orbital overlap without the strong pi-pi stacking associated with completely ladder structures. We reasoned that a combination of both strategies would enable us to address the issues above more effectively.

Thus, we developed electron-deficient thieno[2',3':5,6]pyrido[3,4-g]thieno[3,2-c]isoquinoline-5,11(4H,10H)-dione (TPTI) and its positional isomer thieno[2',3':4,5]pyrido[2,3-g]thieno[3,2-c]quinoline-4,10-dione (TPTQ) based monomer systems copolymerized with carbazole (C) and fluorene (F). We chose the TPTI and TPTQ monomers as the starting point for our polymer synthesis for several reasons. Firstly, they can be copolymerized with a wide spectrum of comonomers to yield semi-ladder structures. Secondly, the resulting polymers could potentially exhibit strong photoluminescence in solution. [9,10] Thirdly, TPTI polymers were known to exhibit field-effect mobility in their OFET devices. [11]

It was found that the variation of chemical structure leads to significant differences in energy levels, emission colors, and intermolecular aggregation. The resulting polymers exhibited high PLQY and moderate charge mobility. We then fabricated solution-processed tri-layered

OLET devices based on these polymers and found that these devices showed high ambipolar charge mobility and strong electroluminescence. An excellent EQE of 2.8% was achieved in the TPTI-F device, one of the highest among solution-processed OLET devices.

2.2 Results and Discussion

2.2.1 Synthesis

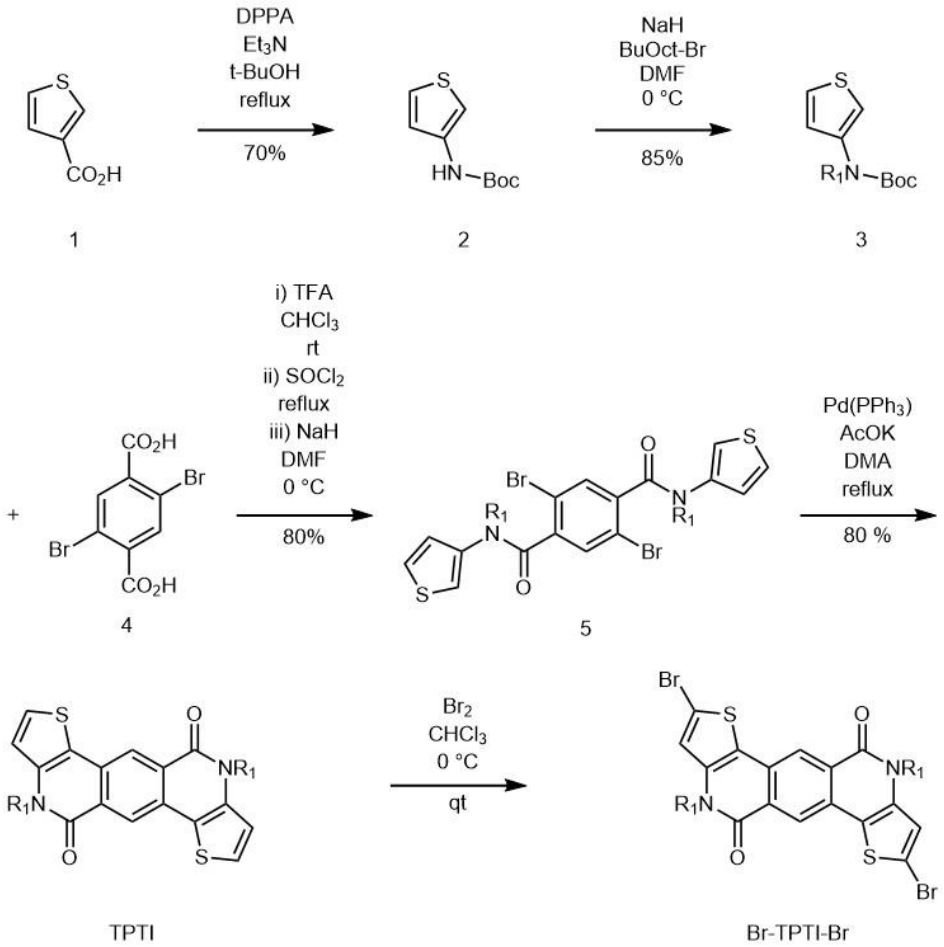

Scheme 2.1: Synthesis of Br-TPTI-Br.

We started our synthesis of di-brominated TPTI monomer from 3-thiophenecarboxylic acid (**Scheme 2.1**) according to a modified procedure reported previously. [12] Compound 1 was subject to Curtius rearrangement with diphenyl phosphoryl azide (DPPA) in tertiary butanol to give a Boc-

protected amine (Compound 2). Compound 2 was then deprotonated using sodium hydride (NaH) and then alkylated via SN2 reaction of 2-butyloctyl bromide in DMF to yield an alkylated thiophene amine (Compound 3). Compound 3 was first deprotected using trifluoroacetic acid (TFA), which was then deprotonated via NaH. This intermediate was then mixed with an acylated version of Compound 4 in DMF and heated to give compound 5. We then converted this compound to TPTI via Heck reaction in DMA with Potassium Acetate (AcOK). TPTI was then brominated to Br-TPTI-Br via N-Bromosuccinimide (NBS) chemistry to yield our monomer.

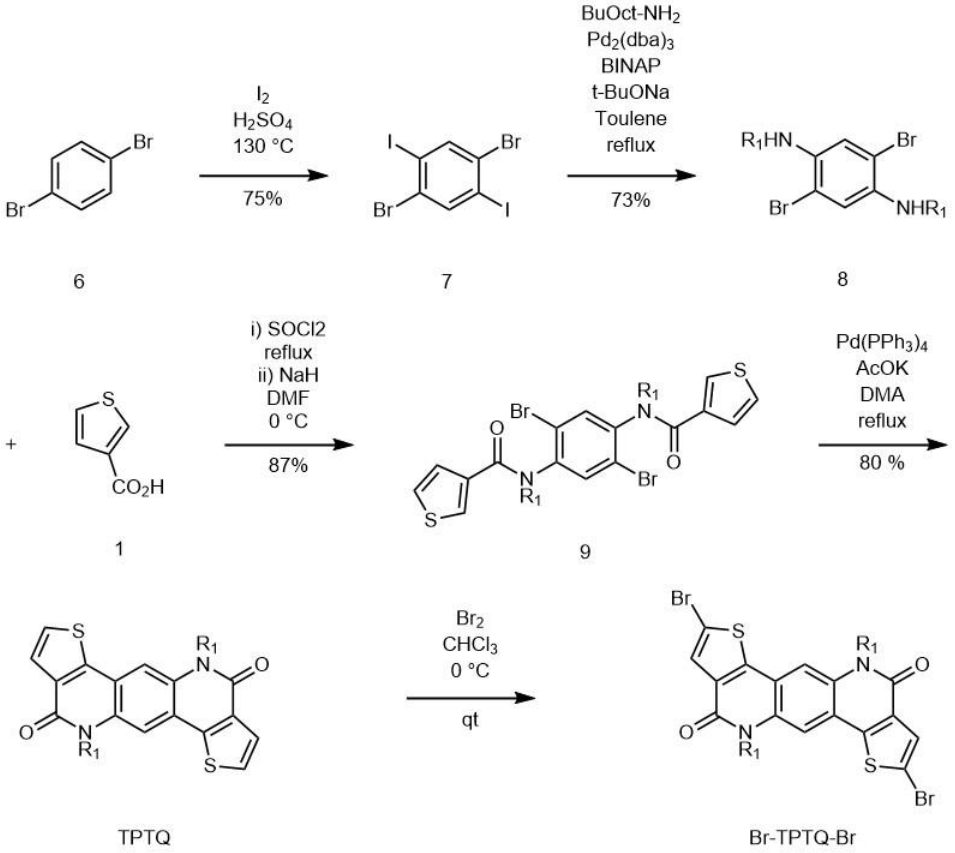

Scheme 2.2: Synthesis of Br-TPTQ-Br.

We synthesized our di-brominated TPTQ monomer as per the protocol shown in **Scheme 2.2**. [9] Here, we started from 1,4-Dibromobenzene (Compound 6), which was subjected to electrophilic aromatic substitution with iodine (I_2) in concentrated sulfuric acid (H_2SO_4). This reaction yielded dibromo diiodo benzene (Compound 7), which was then subjected to Buchwald

reaction with a 2-butyloctyl amine in toluene to give a dibromo diamino benzene (Compound 8). Compound 8 was first deprotonated and then treated with an acylated version of 3-thiophenecarboxylic acid in DMF. Heating this mixture gave Compound 9, which was first subjected to Heck reaction and then bromination to yield our Br-TPTQ-Br monomer.

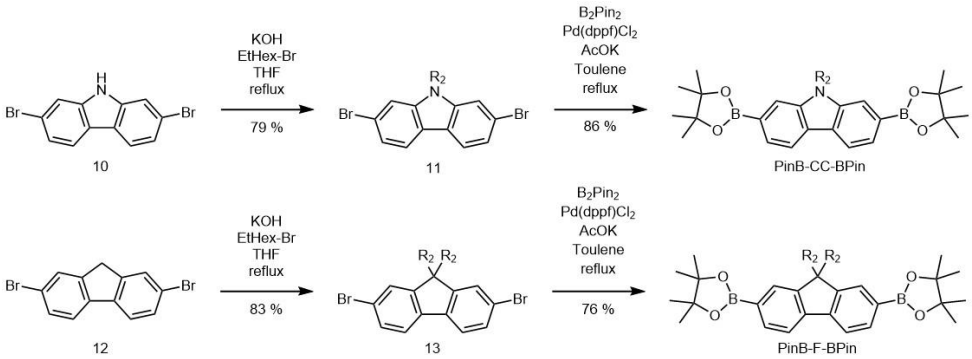

Scheme 2.3: Synthesis of fluorene/carbazole comonomers

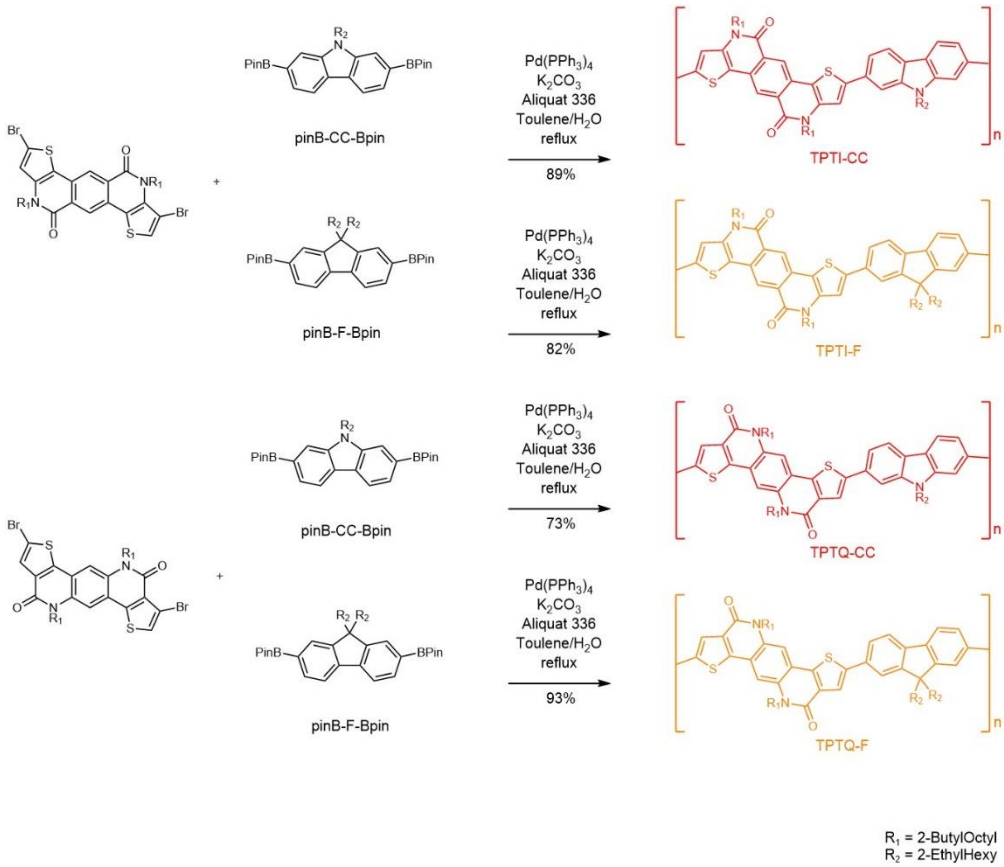

Scheme 2.4: Synthesis of linear polymers

The synthesis of our fluorene/carbazole comonomers was carried out according to previously reported protocols (**Scheme 2.3**). [13–15] Starting from dibrominated fluorene/carbazole molecules, we employed potassium hydroxide (KOH) for deprotonation, followed by an SN2 reaction of 2-ethylhexyl bromide in THF to give Compounds 11 and 13. These compounds were then subjected to borylation reaction with bis pinacolato diboron and palladium catalyst ($Pd(dppf)_2Cl_2$) in DMF to yield our target comonomers.

We then synthesized our four polymeric systems by employing the Suzuki coupling condensation reaction of electron-accepting Br-TPTI-Br and Br-TPTQ-Br with electron-donating carbazoles and fluorenes, as shown in **Scheme 2.4**.

2.2.2 Basic Characterizations

Table 2.1: Physical and Optoelectronic properties of linear polymers

Polymer	HOMO (eV)	LUMO (eV)	Bandgap E_g (eV)	PLQY (%)	M_w	M_n	PDI
TPTI-CC	-5.20[a]/-4.91[b]	-3.20[d]/-2.17[b]	2.74[b]/2.00[c]	23	32428	23471	1.38
TPTI-F	-5.48[a]/-4.93[b]	-3.15[d]/-2.25[b]	2.68[b]/2.33[c]	59	11963	9421	1.27
TPTQ-CC	-5.65[a]/-5.18[b]	-3.30[d]/-2.41[b]	2.77[b]/2.35[c]	15	1861	1524	1.22
TPTQ-F	-5.76[a]/-5.21[b]	-3.38[d]/-2.46[b]	2.75[b]/2.38[c]	77	55172	36012	1.53

[a] Measured from the cyclic voltammetry, [b] Bandgap E_g calculated from DFT, [c] Bandgap E_g calculated from the onset of the film absorption, [d] LUMO energy levels are calculated as HOMO of the polymer from CV + E_g from the onset of film absorption

All our polymers, except TPTQ-CC, were soluble in common organic solvents such as toluene, xylene, and chlorobenzene. The polymer TPTQ-CC had lower molecular weight, primarily due to its poor solubility, which was likely caused by strong pi-pi stacking interactions. The resulting polymers were characterized by using gel permeation chromatography (GPC) in chloroform solution, the results of which are summarized in **Table 2.1**.

PLQYs of our polymers follow a trend in which fluorene polymers exhibit significantly higher quantum yields than their carbazole counterparts. The PLQY of TPTQ-F is 77%, and that of TPTI-F is 59%. Carbazole polymers, however, exhibit low quantum yields of around 20%. We calculated the HOMO/LUMO energy levels and our polymer systems' bandgaps based on the onset of thin-films' oxidation potential in Cyclic Voltammetry and the onset absorbance in the UV-Vis absorbance spectra of thin-films. The HOMO/LUMO energy levels and bandgaps of our four polymers in eVs are -3.2/-5.2, -3.15/-5.48, -3.3/-5.65, -3.38/-5.76 and 2.00, 2.33, 2.35, and 2.38 for TPTI-CC, TPTI-F, TPTQ-CC, and TPTQ-F, respectively. While the bandgaps themselves appear to be similar in value here, the HOMO/LUMO orbitals follow the order: TPTI-CC > TPTI-F > TPTQ-CC > TPTQ-F.

2.2.3 DFT Results

We also performed density functional theory (DFT) calculations at the B3LYP level of theory using a 6-31G** basis set and summarized the results in **Table 2.1**. The HOMO/LUMO energy levels of TPTI-CC were slightly upshifted compared to those of TPTI-F. TPTQ-CC

HOMO/LUMO energy levels were also upshifted compared to TPTQ-F. Both TPTQ polymers had deeper energy levels than their TPTI counterparts, which can be explained by the stronger electron-withdrawing ability of TPTQ. DFT optimized molecular geometry results in **Figure 2.1** indicated linear backbones for all four polymers and extensive delocalization for all eight frontier molecular orbitals. The cyclic voltammetry (CV) measurements (**Table 2.1**) were in good agreement with DFT calculations except for the fact that our DFT energy levels were upshifted by approximately half an eV on average. This upshift is due to the fact that DFT results were calculated assuming a single polymer chain in a vacuum, while CV results were based on a thin polymeric film. The slightly higher HOMO energy levels of carbazole-based polymers could be explained by the stronger electron-donating carbazole than fluorene.

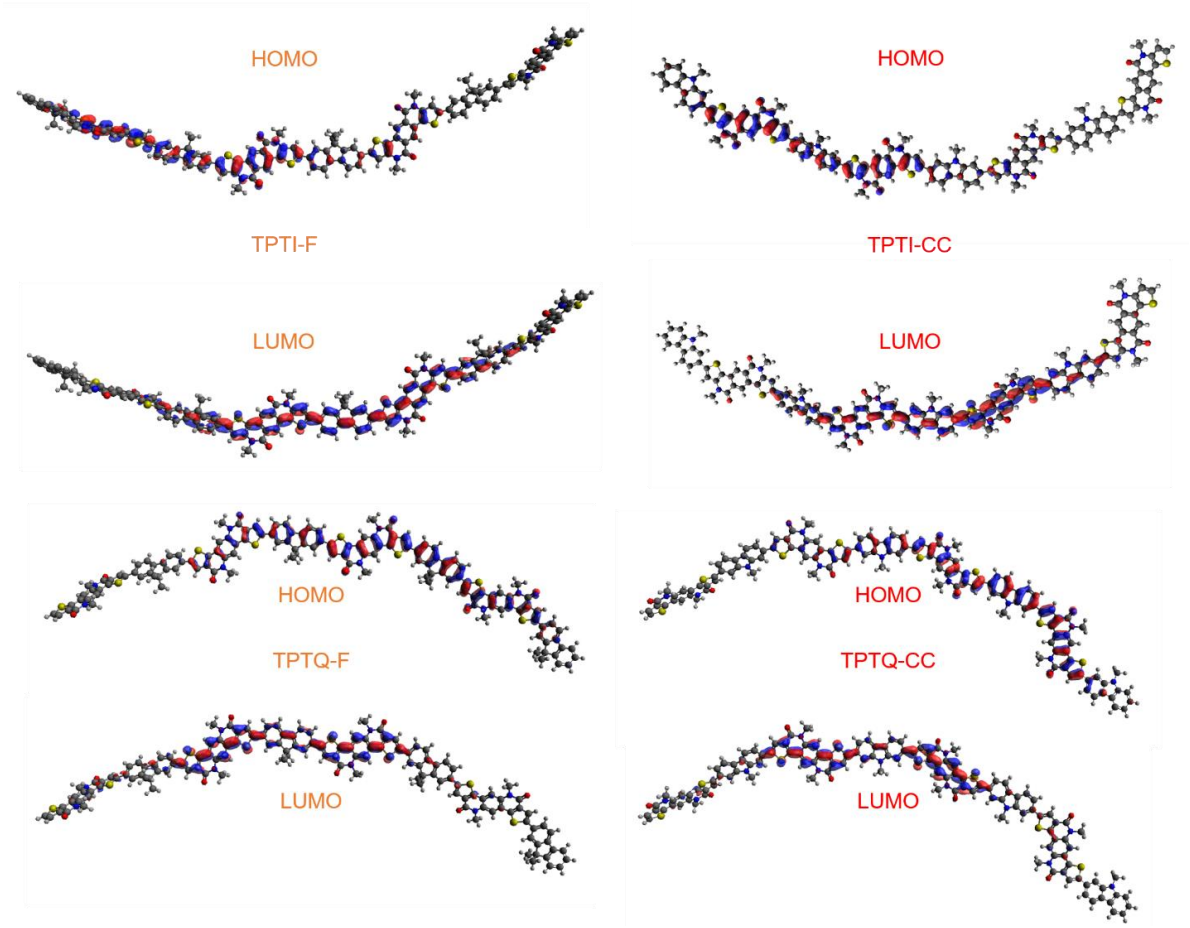

Figure 2.1: DFT results for linear polymers

2.2.4 Optical Characterizations

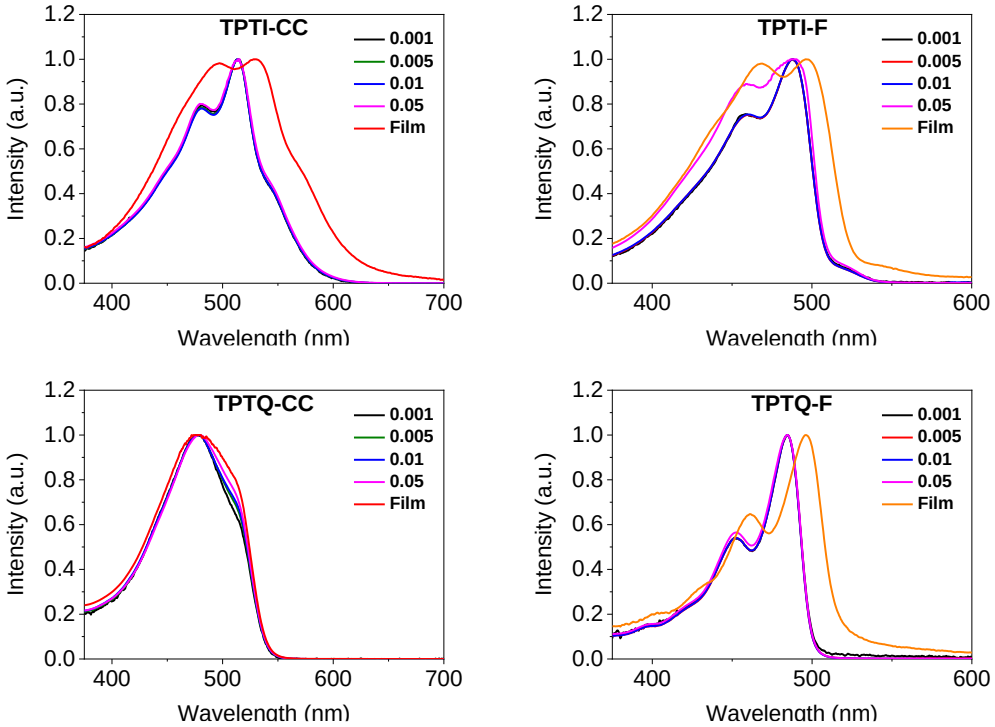

Figure 2.2: UV-Vis absorption spectra for linear polymers

The concentration-dependent UV-Vis absorption spectra for all four of our polymers are shown in **Figure 2.2**. For TPTI-CC solutions, we observed three prominent concentration-independent absorption peaks at 480, 514, and 544 nm, which correspond to 0-2, 0-1, and 0-0 transitions. However, in TPTI-CC thin film, we see a decrease in I_A^{0-1}/I_A^{0-2} ratio and a significant red-shift for all three transitions. On the other hand, the solution absorption spectra of TPTI-F exhibits only two prominent peaks at 460 nm (0-1) and 488 nm (0-0) and a minor shoulder peak at 510 nm. Moreover, the absorption spectrum remains concentration-independent until 0.05 mg/mL, after which the I_A^{0-0}/I_A^{0-1} ratio decreases and continues to decline in the solid-state. Furthermore, the thin film spectrum is slightly red-shited by approximately 10 nm compared to its solution spectra.

For the TPTQ series of polymers, slightly different trends are observed. Polymer TPTQ-F

has intense absorption around 375 to 600 nm, while the polymer TPTQ-CC has a slightly blue-shifted spectrum in the range 375 to 550 nm. The shape of their film absorption spectra is similar to their solution analogs, albeit red-shifted and broadened due to the pi systems' planarization. Of the two polymers, TPTQ-CC exhibited a film absorption spectrum that was nearly identical to the ones in solution, which appear to be almost independent of solution concentration. Here 0-1 absorption is the most intense peak, with the I_A^{0-0}/I_A^{0-1} ratio increasing very slightly with increasing concentration. This seems to be consistent with the extremely poor solubility of TPTQ-CC, which exists in the H-aggregated state in solution and thin-film. On the other hand, a completely different pattern is observed in polymer TPTQ-F in which the 0-0 transition is the most intense. While its solution spectra are concentration-independent, its thin-film spectrum exhibits a decrease in I_A^{0-0}/I_A^{0-1}. This is indicative of J aggregation.

We performed concentration-dependent photoluminescence measurements (**Figure 2.3**) to understand polymeric aggregation. For TPTI-CC thin film, we see two peaks at 642 nm and 712 nm, which correspond to 0-0 and 0-1 transitions, respectively. Although the I_A^{0-0}/I_A^{0-1} ratio decreases with increasing concentration, 0-0 is still the most intense peak. This is consistent with the formation of J-aggregates. [16–18] For TPTI-F, the I_A^{0-0}/I_A^{0-1} ratio decreases gradually with increasing concentration, with the 0-0 transition disappearing completely in thin-film and leaving the 0-1 transition as the dominant peak. This is indicative of strong H-aggregation in TPTI-F films. The thin-film photoluminescence spectrum of TPTI-F exhibits a prominent 0-1 emission peak at 582 nm and a 0-2 shoulder peak at around 619 nm, which are significantly red-shifted from those in dilute solution. Although the large red-shifts in TPTI-F would typically indicate J-aggregation, our polymeric systems are quadrupolar dyes that form red-shifted H-aggregates. [16–19] Furthermore, large red-shifts and extremely broad peaks in thin films indicate the formation of excimers and

strong interchain interaction in TPTI-F.

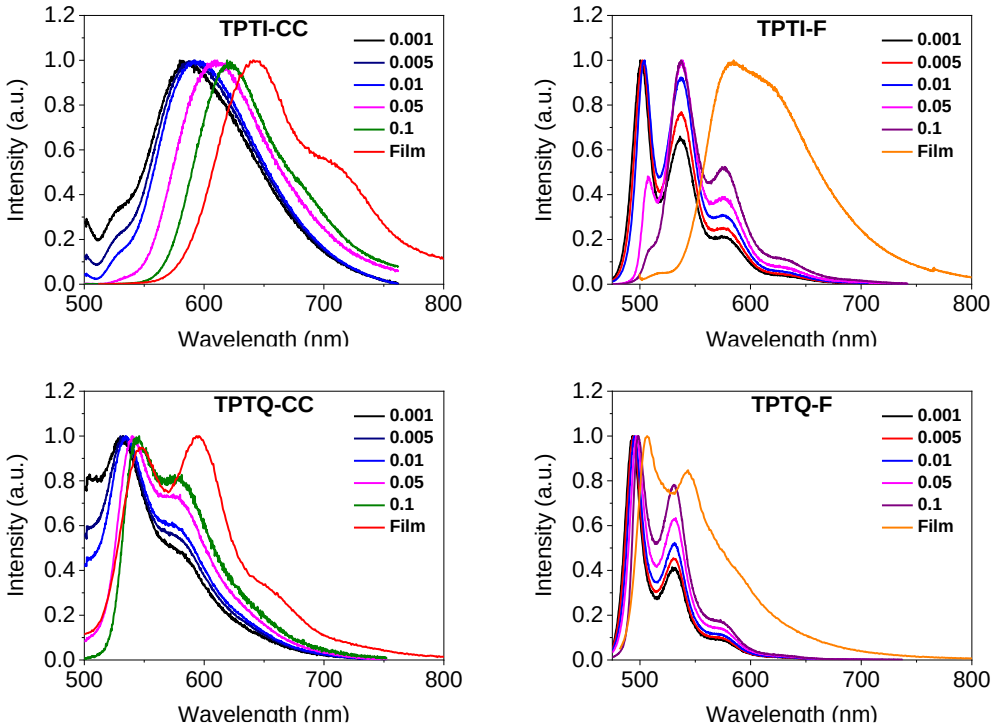

Figure 2.3: Emission spectra for linear polymers

Emission spectra for TPTQ polymers provide further evidence for our hypothesis. They all exhibit slight red-shifts with increasing concentration and are further red-shifted in thin-films. The 0-1 transition peaks are evident in even the most dilute solutions, and their intensity increases with increasing concentration and then further in thin-films. This seems to contradict the formation of H-aggregates, which exhibits blue-shifts with increasing concentration. However, compounds exhibiting quadrupole interactions exhibit red-shits in H-aggregates when intermolecular angles reach specific values. [16–18] A centrosymmetric TPTQ monomer exhibits quadrupole interactions, and if its comonomers in its polymeric form align in trans-mode, this property is kept intact.

We also performed time-resolved fluorescence decay measurements, fitted them against the exponential decay equation, and calculated the fluorescence lifetimes (**Table 2.2**). Both our fluorene polymeric systems exhibited identical lifetimes of 0.62 ns with monoexponential decay

behavior. However, the carbazole polymeric systems showed a dual exponential decay behavior indicating at least two relaxation pathways.

Table 2.2: Time-resolved fluorescence decay measurements for linear polymers

Polymer	τ1 (ns)	Fraction 1 (%)	τ2 (ns)	Fraction 2 (%)
TPTI-CC	1.33	86	0.38	14
TPTI-F	0.62	100		
TPTQ-CC	1.98	52	0.67	48
TPTQ-F	0.62	100	-	-

2.2.5 GIWAX Results

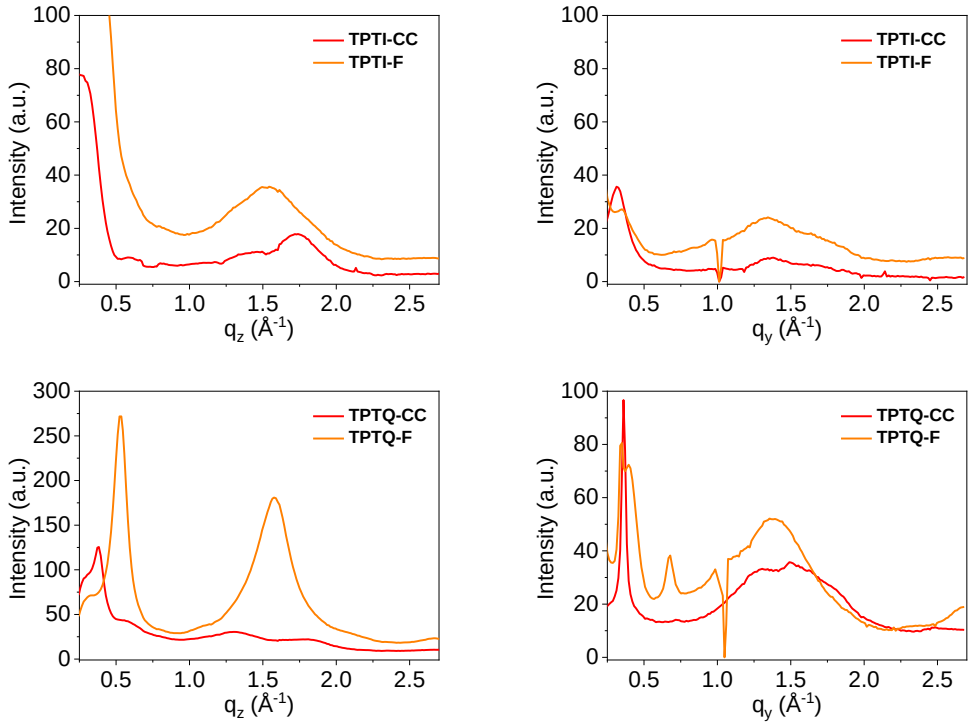

Figure 2.4: Linecuts of 2D GIWAX profiles for linear polymers

We performed GIWAXS experiments to elucidate additional information on molecular packing. We prepared our samples onto PEDOT:PSS coated silicon wafers and took measurements in a vacuum. The linecuts of their 2D scattering profiles along in-plane and out-of-plane orientations are shown in **Figure 2.4**. Our studies suggest that polymer TPTI-F exhibits weak crystallinity with loose molecular packing; TPTI-F had a pi-pi stacking distance of 4.1 Å. This distance is consistent with H-aggregation, in which branched alkyl chains on the TPTI moiety are in close contact with each other. TPTI-CC, on the other hand, exhibited lamellar stacking along the in-plane direction and tight molecular packing with pi-pi stacking distances of 3.6 Å. This is consistent with its more planar molecular backbone, relatively higher M_w, and J-aggregation. Of all four polymers in this series, TPTQ-F is the most crystalline, with two well-resolved peaks appearing in the q_z direction at $0.52Å^{-1}$ and $1.55Å^{-1}$. This corresponds to J-aggregated face-on packing with an interlamellar distance of 12.1 Å and a pi-pi stacking distance of 4.1 Å. TPTQ-CC, however, is relatively amorphous, with a slight preference for face-on packing. These results were consistent with previously determined intramolecular H-aggregation.

2.3 Device Fabrication

2.3.1 OFET Fabrication

We employed all four polymers as active layers in bottom-gate top-contact (BG TC) OFET devices. For this purpose, we used a 300 nm thick silicon dioxide layer as a dielectric with a self-assembled *n*-octadecyltrichlorosilane (OTS) monolayer immobilized on the top. This OTS layer was employed to minimize charge trapping by surface hydroxyl groups on the silicon dioxide dielectric layer. The polymer solutions were then spin-coated onto our substrates under an inert nitrogen atmosphere. This was followed by thermal annealing for thirty minutes on a hot-plate at

120 °C. Afterward, gold was vacuum-deposited through a mask (L = 50 μm, W = 18 mm) on top of the active polymer layer as the source and drain electrodes.

Table 2.3: Charge carrier mobility values for linear polymers

Material	μ_h ($cm^2V^{-1}s^{-1}$)	μ_e ($cm^2V^{-1}s^{-1}$)
TPTI-CC[a]	3.1×10^{-4}	-
TPTI-F[a]	-	1.8×10^{-6}
TPTQ-CC[a]	-	-
TPTQ-F[a]	5.0×10^{-6}	8.7×10^{-5}
TPTI-CC[b]	4.1×10^{-2}	5.9×10^{-2}
TPTI-F[b]	5.1×10^{-2}	1.4×10^{-2}
TPTI-CC[c]	2.6×10^{-1}	2.4×10^{-2}
TPTI-F[c]	4.4×10^{-2}	4.6×10^{-2}
TPTQ-CC[c]	2.0×10^{-1}	6.5×10^{-2}
TPTQ-F[c]	2.8×10^{-1}	1.4×10^{-1}

a Mobility calculated from OTS modified OFET devices; b Mobility calculated from PMMA modified OLET devices; c Mobility calculated from OTS modified OLET devices.

We then measured the optoelectronic properties of the OFET device, the results of which are summarized in **Table 2.3**. Our OFET devices for TPTI-CC polymer exhibited unipolar p-type transport behavior with a relatively moderate hole mobility of 3.1×10^{-4} cm^2 V^{-1} s^{-1}. However, the devices for its TPTI-F polymeric counterpart exhibited unipolar n-type transport behavior along with much lower electron mobility of 1.8×10^{-6} cm^2 V^{-1} s^{-1}. OFET devices for TPTQ-CC failed to exhibit any FET behavior at all, and no mobility was observed. This lack of mobility was in sharp contrast to the devices for TPTQ-F, which were the only ones in this series to exhibit both hole and electron mobility. Of all four polymers, TPTI-CC showed the highest charge carrier mobility in its FET devices. This result is consistent with J-aggregation in addition to improved lamellar stacking and shorter pi-pi stacking distances, as shown in our GIWAX studies.

Although all four polymers exhibited non-zero solution PLQYs, we observed no electroluminescence in these single-layered devices. The lack of emission was probably due to a high charge injection energy barrier and low charge carrier mobility. While the low mobility factor might not be as relevant in OLED devices, it becomes critical in OLET devices where channel lengths are almost a thousand times larger - 50 μm in this case. This increased channel length severely limits charge carrier recombination in our OFET device.

2.3.2 OLET Fabrication

We employed a tri-layered OLET device system to address both of these issues, as shown in **Figure 2.5**. A 30 mg/mL Polymethylmethacrylate (PMMA) propyl acetate solution was spin-coated on top of a 120-150 nm thick Si_3N_4 dielectric layer to minimize charge trapping. We then spin-coated a 5 mg/mL chloroform solution of a DPP-DTT charge transporting layer on top of PMMA. In addition to exhibiting a high hole and electron mobility, DPP-DTT polymer has a high

lying HOMO (-5.2 eV), which matches well with the HOMO of the emissive layers, thereby facilitating hole transport from DPP-DTT towards the emissive layer. Moreover, DPP-DTT polymer has a very poor solubility in xylene or toluene, which means that as long as the emissive layer is soluble in these two solvents, we can fabricate the whole device through orthogonal solution processing. The emissive polymer solutions (12 mg/mL xylene) were then spin-coated on top of the DPP-DTT later.

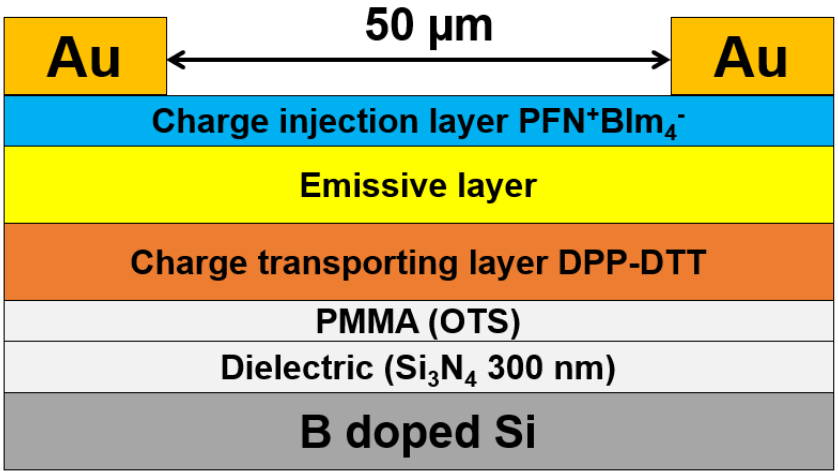

Figure 2.5: OLET Device architecture for linear polymers

From the energy level diagram in **Figure 2.6,** it is clear that the LUMO of all four emissive polymers is misaligned substantially with the work function of gold (5.1 eV), which would obstruct electron injection. To address this issue, we chose to employ $PFN^{+}BIm_4^{-}$ conjugated polyelectrolyte (CPE) as an electron injection layer as its ionic effect lowers the electron injection energy barrier. It is also known that the device performance directly correlates with the thickness of the $PFN^{+}BIm_4^{-}$ layer. [20,21] After thickness optimization, we found that a thickness of around 10 nm is optimal for our device. Afterward, a 30 nm thick gold layer was vacuum-deposited through a mask as source-drain electrodes. To ensure reliability, we fabricated at least ten devices for each emissive polymer and then averaged their results.

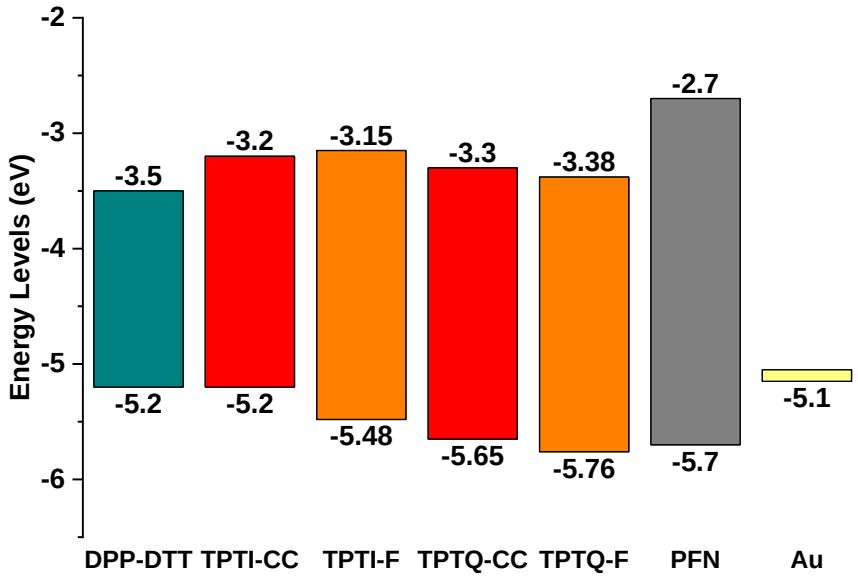

Figure 2.6: Energy Level diagram for linear polymers

Devices of both of our polymers exhibit ambipolar V-shaped transfer curves with hole/electron mobility of 0.041/0.059 $cm^2\ V^{-1}\ s^{-1}$ and 0.051/0.014 $cm^2\ V^{-1}\ s^{-1}$ for TPTI-CC, and TPTI-F, respectively. Multi-layered device structure substantially improved these mobilities from single-layered devices, most likely due to the integration of DPP-DTT polymer as the charge transporting layer. We also observed yellow-orange and yellow emission from TPTI-CC and TPTI-F, respectively (**Figure 2.7**). It was found that the electroluminescent spectra for both polymers were blue-shifted compared to their corresponding solid-state photoluminescent spectra. This blue-shift is clear proof that the emission in devices from these polymers comes from comparatively less aggregated chromophores. Unfortunately, our devices exhibited low-intensity emission and narrow emission zones near the drain electrodes. We hypothesized that it was most likely a consequence of poor synergy between DPP-DTT and the PMMA layer. For this reason, we did not fabricate PMMA modified devices for TPTQ polymers.

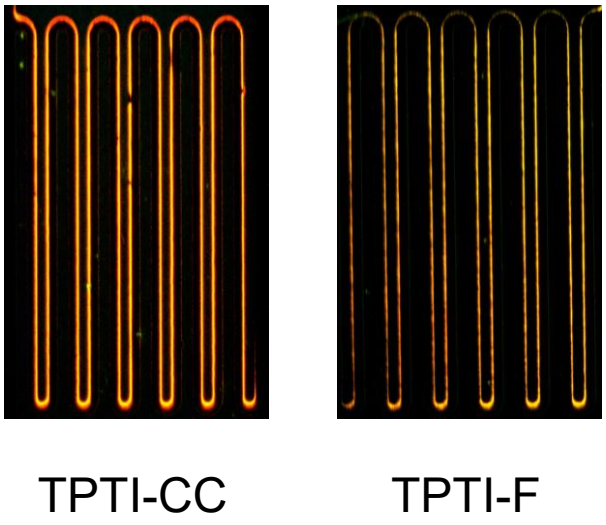

Figure 2.7: Electroluminescence for linear TPTI polymers

2.3.3 OLET Optimization

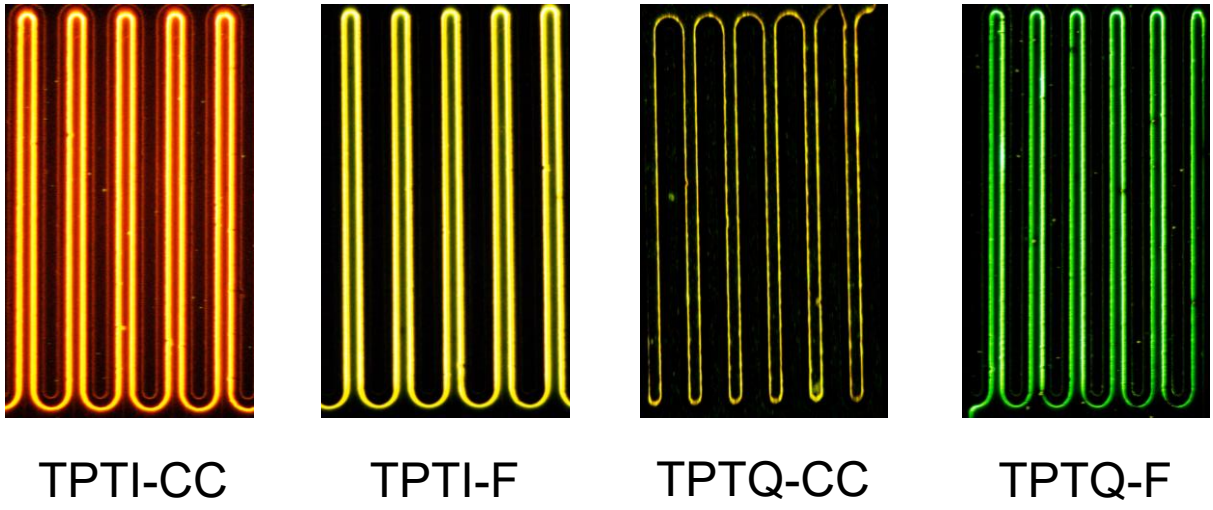

Figure 2.8: Electroluminescence for linear polymers

We sought to replace the relatively thick PMMA layer with a self-assembled OTS monolayer while keeping the rest of the device architecture the same. As is abundantly clear in **Figure 2.8**, the emission intensity in these devices significantly improves from the ones based on PMMA. The emissive regions for at least TPTI-CC and TPTI-F based devices extend further from the electrodes compared with their PMMA modified counterparts under the same gate voltages.

Unfortunately, the emission is still not ideal. It is fixed near the drain electrodes, which most likely is due to the poor charge-transporting behavior of $PFN^{+}BIm_4^{-}$ and the emissive layer, and by extension, an OLED like working mode.

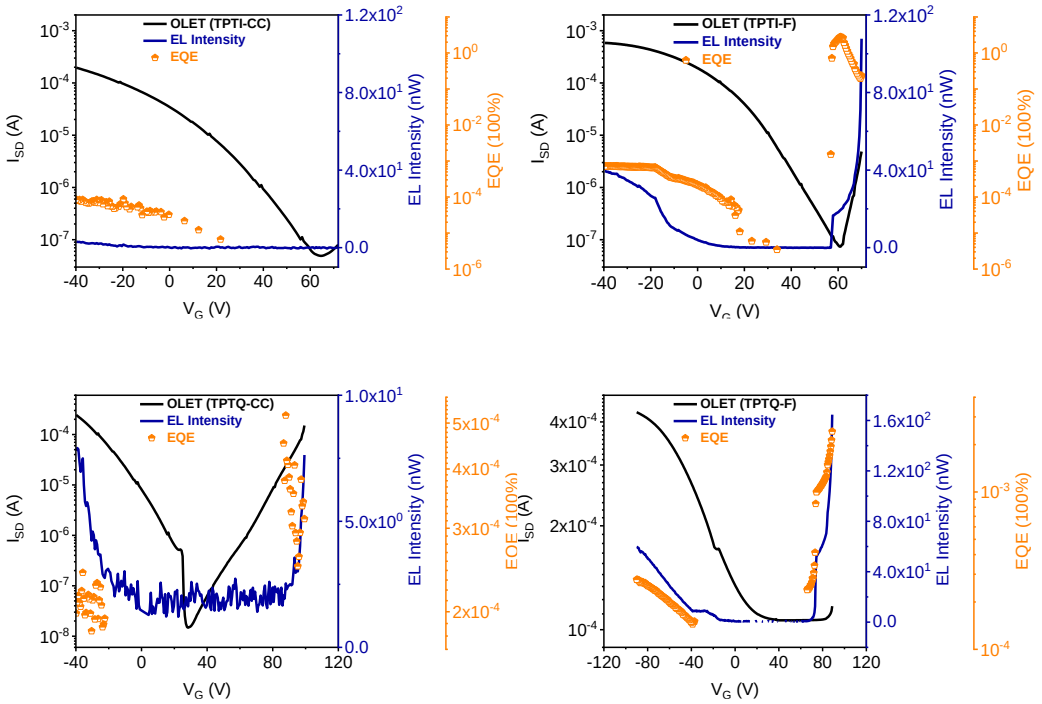

Figure 2.9: EQE and EL intensity for linear polymers

We calculated the electroluminescence quantum efficiency (EQE) and the electroluminescent output (EL intensity) of our OLET devices. We did these calculations by calibrating the photodetector with an OLED of the same material and measuring the photocurrent, divided by the source-drain current (**Figure 2.9**). [22,23] Let us take the case of the TPTI-CC device, for instance. Its EL intensity increases from 0.5 nW at $V_G = -20$ V to 26 nW at $V_G = -65$ V. This is consistent with the device switching-on at −20 V and increased emission intensity as V_G increases. However, we observed the most significant increase in the 55 V < V_G < 70 V range, where EL intensity increases from 4 nW to 153 nW. These performance parameters are comparable with the best vacuum-deposited tri-layered OLET device in literature. [23] We also calculated the

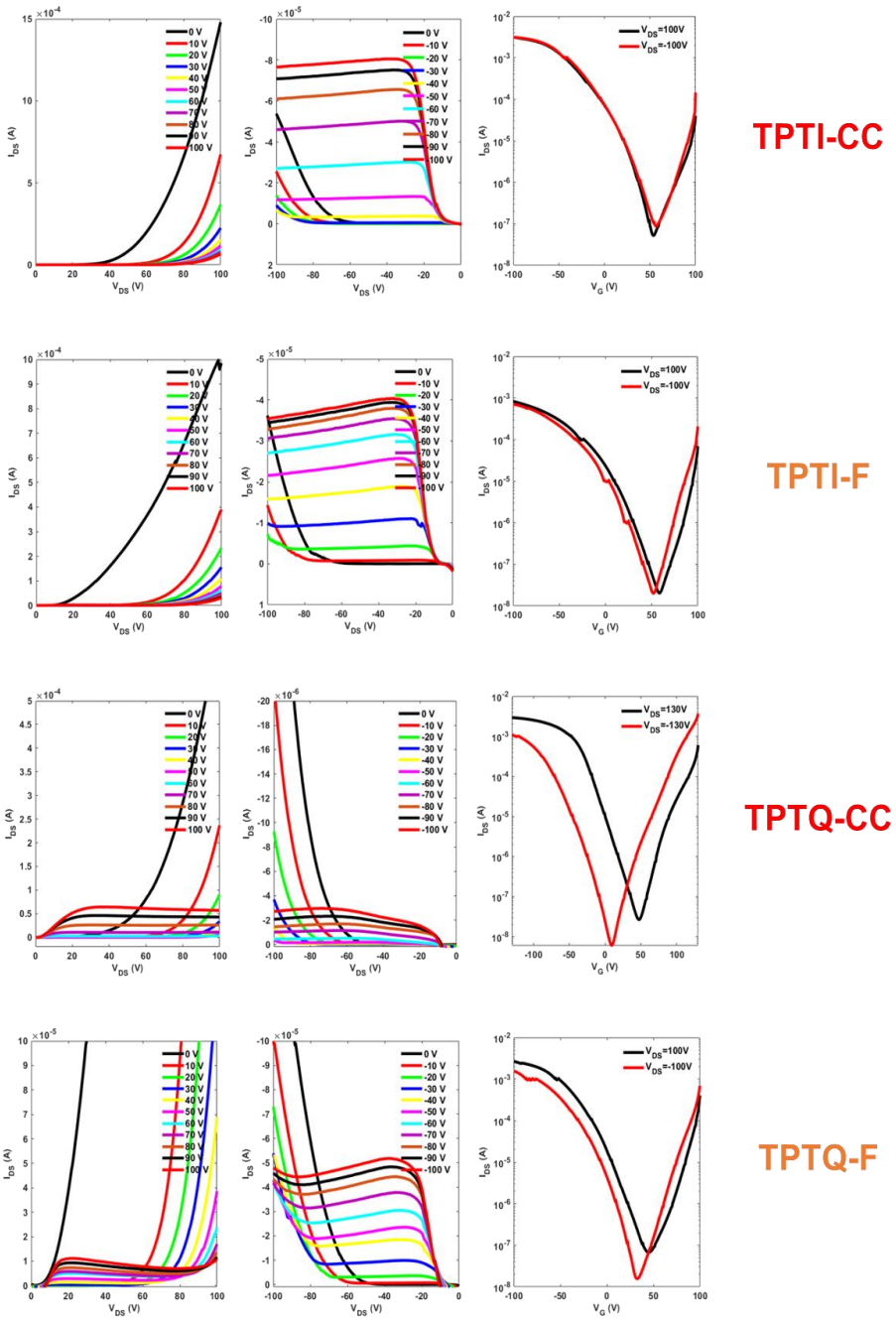

Figure 2.10: Transfer and output curves for linear polymers

EQE as a function of gate voltages for our devices. For TPTI-CC devices, We found the highest EQE (0.56 %) at low applied voltages (V_G= 59 V and V_{SD} = 70V). In terms of EL intensity, the TPTI-F device fared better. Its EL intensity increased from 0.07 nW at V_G = 35 V to 40 nW at V_G = −40 V and then from 16.9 nW at V_G = 58 V to 108 nW at V_G = 70 V. Its highest EQE, however,

was quite impressive (2.8% at V_G= 62 V and V_{SD} = 70V) and was five times higher than the highest EQE for TPTI-CC. Moreover, the highest EQE for tri-layered OLED (ITO/PEDOT:PSS/DPP-DTT/Emissive layer/ $PFN^+BIm_4^-$/Ca/Al) was three orders of magnitude lower than its corresponding OLET device.

Both of our TPTQ devices exhibited very low EQEs (10^{-3} %). For TPTQ-CC, this is not surprising as it exhibited very poor solubility to make good films. It is surprising to note the low EQE for TPTQ-F, which exhibited high solution PLQY, relatively high OLET mobility, and decent solubility. We can explain the low EQE if we consider the highly crystalline molecular packing and strong pi-pi interactions in TPTQ-F, which quench emission. Additionally, the EQE for both the TPTQ polymers stays roughly constant over a wide voltage range, which is a plus.

Semi-ladder structures here played a critical role in polymeric packing, charge transport, and light emission. Finding the right degree of ladderization here was essential to device performance as fully ladder TPTI/TPTQ molecules failed to exhibit any luminescence in its OLET device. This lack of emission was most likely due to strong pi-pi interactions quenching excited chromophores. TPTI/TPTQ monomer choice was critical here, considering that TPTI polymers' devices gave an EQE three orders of magnitude higher than their TPTQ counterparts.

2.4 Conclusion

In this work, we designed and synthesized four semi-ladder copolymers, TPTI-CC, TPTI-F, TPTQ-CC, and TPTQ-F. All four polymers were characterized in detail to elucidate structural information, in addition to physical and optoelectronic properties. We found that very slight chemical structure changes lead to significant differences in energy levels, emission colors, and intermolecular aggregation. These polymeric systems exhibit moderate charge carrier mobility,

impressive emission, and suitable energy levels. The OLET devices made from TPTI-F showed high photoluminescence quantum yield and balanced electron/hole mobility (0.046/0.044 $cm^2 V^{-1} s^{-1}$). We obtained an EQE as high as 2.8% at a relatively low voltage (V_G= 62 V and V_{SD} = 70V). At the same time, the obtained EQE was a thousand times higher than its corresponding OLED device. Our system demonstrated enough promise to merit further device and molecular structure optimization. We intend to address both issues in later chapters.

2.5 Materials and Methods

Unless stated otherwise, all chemicals and solvents were procured commercially and used without further purification. Column chromatography was carried out on silica gel (silica 60M, 400-230 mesh). ^{1}H and ^{13}C NMR spectra were obtained employing a 500MHz Bruker DRX-500 spectrometer in $CDCl_3$ with TMS as an internal reference. Mass Spectra were recorded utilizing Bruker Daltonics UltrafleXtreme MALDI-TOF system and dithranol as a matrix. MWs and PDIs of our polymers were determined by using a Waters Associates liquid chromatography GPC equipped with a Waters 510 HPLC pump, a Waters 410 differential refractometer, and a Waters 486 tunable absorbance detector. Polystyrene was used as standard and chloroform as the eluent.

2.5.1 Synthesis

Compound 2: 3-Thiophenecarboxylic acid (1 eq) was dissolved in tertiary butanol (60 mL). Diphenyl phosphoryl azide (1.3 eq) and triethylamine (2 eq) were added successively. The mixture was then refluxed overnight and allowed to cool to room temperature. The solvent was then evaporated under reduced pressure, and the residue was extracted with DCM. The organic layer was washed with Na_2CO_3 and then brine. It was then dried over $MgSO_4$, and the solvent was removed under reduced pressure. The crude mixture was then purified by silica gel chromatography eluted with hexane:ethyl acetate (4:1) to afford Compound 2 as a white solid in a 70% yield. ^{1}H-NMR (500 MHz, DMSO): δ (ppm) 9.58 (br, 1H), 7.35 (d, 1H), 7.16 (s, 1H), 6.99 (d, 1H), 1.46 (s, 9H). ^{13}C-NMR (100 MHz, DMSO): δ (ppm) 152.69,137.29, 124.49, 121.07, 105.73, 78.88, 28.05.

Compound 3: Compound 2 (1 eq) was dissolved in DMF and added dropwise to NaH (2 eq) suspension in DMF (40 mL) at 0 °C. After 30 min, 2-butyloctyl bromide (2 eq) was added slowly

to the mixture, which then was stirred at room temperature overnight. The reaction mixture was poured into water and extracted with DCM. The organic layer was washed with water, dried over $MgSO_4$, and the solvent was removed under reduced pressure. The crude mixture was then purified by silica gel chromatography eluted with hexane:ethyl acetate (9:1) to afford Compound 3 in an 85% yield. ^{1}H-NMR (500 MHz, CHCl3): δ (ppm) 7.19 (m, 1H), 7.03 (d, 2H), 3.57 (d, 2H), 1.61 (m, 1H), 1.46 (s, 9H), 1.22 (m, 18H), 0.86 (m, 6H). ^{13}C-NMR (100 MHz, CDCl3): δ (ppm) 154.68, 141.11, 125.49, 123.79, 115.48, 80.46, 53.42, 36.66, 31.93, 31.40, 31.09, 29.86, 28.63, 28.48, 26.40, 23.24, 22.80, 14.24, 14.19. MS (MALDI-TOF) *m*/*z* 367.18 (M+), calcd 367.59.

Compound 5: Compound 3 (2.5 eq) was dissolved in a mixture of TFA and chloroform (30 ml, 1:2) and stirred at room temperature overnight. The reaction mixture was poured into water and extracted with DCM. The organic layer was washed with water, dried over $MgSO_4$, and the solvent was removed under reduced pressure. It was then directly used for the next step. A solution of Compound 4 (1 eq) was dissolved in thionyl chloride (20 mL) and refluxed overnight. Afterward, the solvent was removed under reduced pressure to yield an acyl chloride as a white solid. It was then dissolved in DMF (20 mL) and added dropwise to a suspension of Compound 3, NaH (4 eq), and DMF (30 mL) at 0 °C. The reaction mixture was stirred at room temperature overnight. Afterward, the reaction mixture was then poured into water and extracted with DCM. The organic layer was washed with water, dried over $MgSO_4$, and the solvent was removed under reduced pressure. The crude mixture was then purified by silica gel chromatography eluted with hexane:ethyl acetate (9:1) to afford Compound 5 in an 80 % yield. ^{1}H-NMR (500 MHz, CDCl3): δ (ppm) 7.12 (d, 2H), 7.08 (s, 2H), 6.84 (s, 2H), 6.76 (d, 2H), 3.75 (s, 4H), 1.56 (m, 2H), 1.22 (m, 32H), 0.86 (m, 12H). ^{13}C-NMR (100 MHz, CDCl3): δ (ppm) 166.79, 140.42, 139.70, 132.03,

125.84, 125.50, 120.88, 118.04, 52.34, 36.23, 31.95, 31.23, 30.97, 29.80, 28.61, 26.32, 23.20, 22.78, 14.24. MS (MALDI-TOF) *m*/*z* 822.64 (M+), calcd 822.84.

TPTI: Compound 5 (1 eq), $Pd(PPh_3)_4$ (0.05 eq), and AcOK (3 eq) was dissolved in DMA (150 mL). The mixture was degassed for 30 min and then refluxed for 4 h. The reaction mixture was then poured into water and extracted with DCM. The organic layer was washed with water, dried over $MgSO_4$, and the solvent was removed under reduced pressure. The crude mixture was then purified by silica gel chromatography eluted with hexane:ethyl acetate (9:1) to afford TPTI as a yellow solid in an 80% yield. ^{1}H-NMR (500 MHz, CDCl3): δ (ppm) 8.87 (s, 2H), 7.48 (d, 2H), 7.08 (d, 2H), 4.22 (d, 4H), 2.01 (m, 2H), 1.25-1.38 (m, 32H), 0.86 (m, 12H). ^{13}C-NMR (100 MHz, CDCl3): δ (ppm) 161.70, 139.55, 130.08, 126.90, 126.25, 123.72, 118.05, 117.85, 49.80, 37.25, 31.91, 31.76, 31.48, 29.77, 29.00, 26.77, 23.18, 22.73, 14.20. MS (MALDI-TOF) *m*/*z* 661.43 (M+), calcd 661.01.

Br-TPTI-Br: TPTI (1 eq) was dissolved in chloroform, and the solution cooled to 0 °C in the dark. Br_2 (10 eq) was then added dropwise, after which the solution was warmed to room temperature and stirred for 4 hours. The reaction mixture was poured into an aqueous solution of Na_2SO_3 and extracted with chloroform. The organic layer was dried with $MgSO_4$, and the solvent was removed under reduced pressure. The crude mixture was recrystallized from dichloromethane/methanol to give a yellow solid in quantitative yield. ^{1}H-NMR (500 MHz, CDCl3): δ (ppm) 8.70 (s, 2H), 7.07 (s, 2H), 4.16 (br, 4H), 1.99 (m, 2H), 1.24-1.41 (m, 32H), 0.75-0.92 (m, 12H). ^{13}C-NMR (100 MHz, CDCl3): δ (ppm) 161.05, 138.84, 129.29, 126.77, 123.34, 120.86, 118.79, 115.14, 49.74, 37.02, 31.81, 31.50, 31.24, 29.66, 28.76, 26.54, 23.06, 22.64, 14.09. MS (MALDI-TOF) *m*/*z* 818.89 (M+), calcd 818.81.

Compound 7: 1,4-dibromobenzene (1 eq) and I_2 (4 eq) were dissolved in 250 mL of concentrated H_2SO_4. The mixture was then stirred at 130 °C for 72 h and then poured into ice water. The precipitate was then dissolved in DCM and washed with saturated sodium sulfite (Na_2SO_3), sodium bicarbonate ($NaHCO_3$), and water. The solvent was then removed under reduced pressure to yield Compound 7 as a white solid in a 75% yield. ^{1}H-NMR (500 MHz, CDCl3): δ (ppm) 8.05 (s, 2H). ^{13}C-NMR (100 MHz, CDCl3): δ (ppm) 142.51, 129.43, 101.56. MS (MALDI-TOF) *m*/*z* 487.77 (M+), calcd 487.70.

Compound 8: Compound 7 (1 eq), 2-butyloctyl amine (3 eq), $Pd_2(dba)_3$ (0.1 eq), BINAP (0.5 eq), and Sodium tert-butoxide (t-BuONa) (3 eq) were dissolved in 100 mL of toluene. The mixture was then purged with nitrogen (N_2) for 30 mins and then refluxed for 2 hours. The reaction mixture was then poured into water and extracted with DCM. The organic layer was washed with water, dried over $MgSO_4$, and the solvent was removed under reduced pressure. The crude mixture was then purified by silica gel chromatography eluted with hexane:DCM (9:1) to afford Compound 8 as a yellow oil in a 73% yield. ^{1}H-NMR (500 MHz, CDCl3): δ (ppm) 6.81 (s, 2H), 3.78 (s, 2H), 2.98 (t, 4H), 1.59 (m, 2H), 1.25-1.49 (m, 32H), 0.84-0.97 (m, 12H). MS (MALDI-TOF) *m*/*z* 602.65 (M+), calcd 602.58.

Compound 9: A solution of Compound 1 (4 eq) was dissolved in thionyl chloride (20 mL) and refluxed overnight. Afterward, the solvent was removed under reduced pressure to yield an acyl chloride as a white solid. It was then dissolved in DMF (20 mL) and added dropwise to a suspension of Compound 8 (1 eq), NaH (4 eq), and DMF (30 mL) at 0 °C. The reaction mixture was stirred at room temperature overnight. The reaction mixture was then poured into water and extracted with DCM. The organic layer was washed with water, dried over $MgSO_4$, and the solvent was removed under reduced pressure. The crude mixture was then purified by silica gel

chromatography eluted with hexane:ethyl acetate (9:1) to afford Compound 9 in an 87 % yield. ^{1}H-NMR (500 MHz, CDCl3): δ (ppm) 7.46 (d, 2H), 7.15 (s, 2H), 7.06 (d, 4H), 4.011 (m, 2H), 3.39 (m, 2H), 1.58 (m, 2H), 1.25 (m, 32H), 0.84 (m, 12H). ^{13}C-NMR (100 MHz, CDCl3): δ (ppm) 164.81, 142.94, 136.57, 135.40, 128.54, 127.91, 125.00, 122.75, 53.09, 36.48, 31.88, 31.28, 30.92, 29.72, 28.54, 26.36, 23.00, 22.98, 14.23. MS (MALDI-TOF) *m*/*z* 822.90 (M+), calcd 822.84.

TPTQ: Compound 9 (1 eq), $Pd(PPh_3)_4$ (0.05 eq), and AcOK (3 eq) was dissolved in DMA (150 mL). The mixture was degassed for 30 min and then refluxed for 4 h. The reaction mixture was then poured into water and extracted with DCM. The organic layer was washed with water, dried over $MgSO_4$, and the solvent was removed under reduced pressure. The crude mixture was then purified by silica gel chromatography eluted with hexane:ethyl acetate (9:1) to afford TPTQ as a yellow solid in an 80% yield. ^{1}H-NMR (500 MHz, CDCl3): δ (ppm) 7.76 (d, 2H), 7.74 (s, 2H), 7.43 (d, 2H), 4.40 (br, 4H), 2.02 (m, 2H), 1.24-1.34 (m, 32H), 0.82-0.91 (m, 12H). ^{13}C-NMR (100 MHz, CDCl3): δ (ppm) 158.81, 144.41, 132.31, 131.91, 127.52, 125.65, 119.43, 110.27, 46.16, 37.06, 31.96, 31.71, 29.89, 29.39, 27.17, 23.31, 22.77, 14.28, 14.22. MS (MALDI-TOF) *m*/*z* 661.09 (M+), calcd 661.01.

Br-TPTQ-Br: TPTQ (1 eq) was dissolved in chloroform, and the solution cooled to 0 °C in the dark. Br_2 (10 eq) was then added dropwise, after which the solution was warmed to room temperature and stirred for 4 hours. The reaction mixture was poured into an aqueous solution of Na_2SO_3 and extracted with chloroform. The organic layer was dried with $MgSO_4$, and the solvent was removed under reduced pressure. The crude mixture was recrystallized from dichloromethane/methanol to give a yellow solid in quantitative yield. ^{1}H-NMR (500 MHz, CDCl3): δ (ppm) 7.73 (s, 2H), 7.59 (s, 2H), 4.36 (br, 4H), 1.98 (m, 2H), 1.25-1.40 (m, 32H), 0.86-0.92 (m, 12H). ^{13}C-NMR (100 MHz, CDCl3): δ (ppm) 156.92, 144.90, 132.09, 131.89, 129.72,

118.25, 114.24, 109.58, 45.83, 36.93, 31.95, 31.63, 29.85, 29.30, 27.22, 23.22, 22.71, 14.16. MS (MALDI-TOF) *m*/*z* 818.87 (M+), calcd 818.81.

General Procedure for Semi-Ladder Copolymers: A mixture of Br-TPTI-Br/Br-TPTQ-Br monomer (1 eq) and Carbazole/Fluorene comonomer (1 eq), K_2CO_3 (4 eq), Aliquat 336 (3 drops), and $Pd(PPh_3)_4$ (0.05 eq) were dissolved in 4ml of toluene/H_2O (10:1). The mixture was degassed for 30 minutes and then refluxed for 72 hours. After cooling to room temperature, the mixture was passed through Celite and precipitated in methanol. The polymer fibers were then washed by Soxhlet extraction with methanol, acetone, hexane, and chloroform. The final polymer was obtained after reprecipitation of chloroform fraction in methanol.

TPTI-CC: Yield: 89 %. ^{1}H-NMR (500 MHz, $C_2D_2Cl_4$): δ (ppm) 6.6-9.0 (br, 10H), 3.60-4.85 (br, 6H), 2.0-2.35 (br, 3H), 1.15-1.75 (m, 40H), 0.72-1.11 (m, 18H). Elemental Analysis calculated for $[C_{60}H_{79}N_3O_2S_2]n$: C: 76.79; H: 8.49; N: 4.48. Found: C: 75.39; H: 8.17; N: 4.13.

TPTI-F: Yield: 82%. ^{1}H-NMR (500 MHz, $CDCl_3$): δ (ppm) 8.92 (s, 2H) 7.30-8.01 (br, 8H), 4.33 (br, 4H), 2.14 (br, 6H), 1.20-1.51 (m, 32H), 0.61-1.05 (m, 42H). Elemental Analysis calculated for $[C_{69}H_{96}N_2O_2S_2]n$: C: 78.96; H: 9.22; N: 2.67. Found: C: 77.63; H: 9.06; N: 2.69.

TPTQ-CC: Yield: 73%. No NMR spectra could be obtained due to solubility issues. Elemental Analysis calculated for $[C_{60}H_{79}N_3O_2S_2]n$: C: 76.79; H: 8.49; N: 4.48; O: 3.41; S: 6.83. Found: C: 75.01; H: 8.51; N: 4.16.

TPTQ-F: Yield: 93 %.^{1}H-NMR (500 MHz, CDCl3): δ (ppm) 8.07 (s, 2H) 7.45-7.85 (br, 8H), 4.51 (br, 4H), 2.12 (br, 6H), 1.20-1.50 (m, 32H), 0.60-1.05 (m, 42H). Elemental Analysis calculated for $[C_{69}H_{96}N_2O_2S_2]n$: C: 78.96; H: 9.22; N: 2.67; O: 3.05; S: 6.11. Found: C: 75.89; H: 8.99; N: 2.48.

2.5.2 Optical analysis

UV-Vis spectra were obtained using a Shimadzu UV-2401PC UV-Vis spectrophotometer. Fluorescence spectra were measured using a Horiba FluoroLog fluorometer at the University of Chicago MRSEC MPML. Time-dependent fluorescence decay spectra were measured using an ISS Chronos BH fluorometer at the University of Chicago MRSEC MPML. The instrument response function was estimated using a standard 1% LUDOX solution from Sigma Aldrich. Exponential decay fitting was performed using the software provided with the instrument.

2.5.3 X-ray analysis

GIWAXS measurements were performed employing the 8ID-E beamline of the Advanced Photon Source at the Argonne National Laboratory with a radiation wavelength of 1.1354 Å. The samples were prepared on a polished silicon wafer covered with PEDOT:PSS. The same solvent and annealing protocols were used in the device fabrication process.

2.5.4 Device Fabrication

Our OLET devices were assembled in a bottom-gate top-contact (BG-TC) configuration. B doped silicon wafers with 300 nm silicon nitride were purchased from University Wafers and used as substrates. Wafers were cut into 14×19 mm slides and ultrasonicated in acetone and isopropanol for 15 min each. Afterward, they were dried using compressed dry nitrogen. Silicon wafers were then surface modified with octadecyltrichlorosilane (OTS). Towards this end, silicon wafers were placed in a glass petri dish, and one drop of octadecyltrichlorosilane was added. It was then put in a vacuum oven at 120°C for 1 hour and then cooled down to room temperature. Chloroform solution (5 mg mL^{-1}) of DPP-DTT was spin-coated on a rotating substrate at 1500

rpm/60 seconds and annealed at 120°C for 30 min in a glove box. This yielded a DPP-DTT layer with a thickness of around 30 nm. Emissive polymers were then dissolved in *p*-xylene with a concentration of 10 mg mL^{-1} and spin-coated onto DPP-DTT at 2000 rpm for 40 seconds. Polymer films were then annealed at 120°C for 30 min in a glove box. Then $PFN^{+}BIm4^{-}$ was dissolved in methanol with a concentration of 2 mg mL^{-1}. After filtration, the $PFN^{+}BIm4^{-}$ layer was spin-coated onto the active layer at 7000 rpm for 30 seconds. Polymer films were then annealed at 60°C for 20 min in air and then transferred back to the glove box for thermal deposition of source-drain electrodes. 30 nm of gold was deposited in a vacuum chamber under $<10^{-6}$ Torr pressure through a shadow mask purchased from Ossila Ltd.

Our OLED device had a structure as follows: ITO/PEDOT:PSS/DPP-DTT/emissive layer/$PFN^{+}BIm_4^{-}$/Ca/Al. ITO glass was ultrasonicated in chloroform, acetone, and isopropanol for 15 minutes each and then dried using compressed nitrogen. It was then cleaned in UV/ozone for 20 minutes. PEDOT:PSS from Heraeus was then spin-coated onto the ITO glass at 6000 rpm for 60 seconds and then annealed in a vacuum oven at 95°C. The addition of DPP-DTT, emissive, and $PFN^{+}BIm_4^{-}$ layers was identical to the protocol described for OLET. 20 nm calcium and 80 nm aluminum were then thermally evaporated in a vacuum chamber under $<10^{-6}$ Torr pressure through a shadow mask with a defined device area of 3.14 mm^2.

2.5.5 Device Measurements

All the devices were tested in a nitrogen glovebox in the dark. Two-channel SMU Keithley 2612A was used to test the output and transfer characteristics of our devices. The photodiode FDS100-CAL purchased from Thorlabs was calibrated with OLED of known irradiance based on the same emissive layer as the OLET. The irradiance of OLED was then measured using a

calibrated integrating sphere AvaSphere-50-IRRAD and AvaSpec-ULS2048 spectrometer. The photocurrent from the calibrated photodiode placed right in front of the operating device was used to calculate the brightness of our OLET device and the photon flux. Lambertian emission was assumed. The number of injected electrons was calculated from the source-drain current. EQE was calculated as the ratio of photon flux to the number of injected electrons per second.

2.6 References

(1) Zhang, C.; Chen, P.; Hu, W. Organic Light-Emitting Transistors: Materials, Device Configurations, and Operations. *Small*. 2016, pp 1252–1294.

(2) Liu, C. F.; Liu, X.; Lai, W. Y.; Huang, W. Organic Light-Emitting Field-Effect Transistors: Device Geometries and Fabrication Techniques. *Advanced Materials*. 2018.

(3) Yuan, D.; Sharapov, V.; Liu, X.; Yu, L. Design of High-Performance Organic Light-Emitting Transistors. *ACS Omega*. 2019.

(4) Zaumseil, J. Recent Developments and Novel Applications of Thin Film, Light-Emitting Transistors. *Advanced Functional Materials*. 2019.

(5) Muccini, M.; Toffanin, S. *Organic Light-Emitting Transistors: Towards the Next Generation Display Technology*; 2016.

(6) Hepp, A.; Heil, H.; Weise, W.; Ahles, M.; Schmechel, R.; von Seggern, H. Light-Emitting Field-Effect Transistor Based on a Tetracene Thin Film. *Phys. Rev. Lett.* **2003**, *91* (15), 157406.

(7) Zaumseil, J.; Donley, C. L.; Kim, J. S.; Friend, R. H.; Sirringhaus, H. Efficient Top-Gate, Ambipolar, Light-Emitting Field-Effect Transistors Based on a Green-Light-Emitting Polyfluorene. *Adv. Mater.* **2006**.

(8) Chen, H.; Xing, X.; Miao, J.; Zhao, C.; Zhu, M.; Bai, J. W.; He, Y.; Meng, H. Highly Efficient Flexible Organic Light Emitting Transistor Based on High-k Polymer Gate Dielectric. *Adv. Opt. Mater.* **2020**.

(9) Jung, I. H.; Zhao, D.; Jang, J.; Chen, W.; Landry, E. S.; Lu, L.; Talapin, D. V.; Yu, L. Development and Structure/Property Relationship of New Electron Accepting Polymers Based on Thieno[2′,3′:4,5]Pyrido[2,3-g]Thieno[3,2-c]Quinoline-4,10-Dione for All-Polymer Solar Cells. *Chem. Mater.* **2015**, *27* (17), 5941–5948.

(10) Adegoke, O. O.; Jung, I. H.; Orr, M.; Yu, L.; Goodson, T. Effect of Acceptor Strength on Optical and Electronic Properties in Conjugated Polymers for Solar Applications. *J. Am. Chem. Soc.* **2015**.

(11) Cao, Y.; Guo, Z. H.; Chen, Z. Y.; Yuan, J. S.; Dou, J. H.; Zheng, Y. Q.; Wang, J. Y.; Pei, J. Pentacyclic Aromatic Bislactam-Based Conjugated Polymers: Constructed by Beckmann Rearrangement and Application in Organic Field-Effect Transistor. *Polym. Chem.* **2014**.

(12) Jung, I. H.; Lo, W.; Jang, J.; Chen, W.; Landry, E. S.; Lu, L.; Talapin, D. V; Yu, L.; Zhao, D. Synthesis and Search for Design Principles of New Electron Accepting Polymers for All-Polymer Solar Cells Synthesis and Search for Design Principles of New Electron Accepting Polymers for All-Polymer Solar Cells. **2014**.

(13) Jin, M.; Zhu, Z. C.; Liao, Q. Y.; Li, Q. Q.; Li, Z. Dendronized Polymers with High FTC-Chromophore Loading Density: Large Second-Order Nonlinear Optical Effects, Good Temporal and Thermal Stability. *Chinese J. Polym. Sci. (English Ed.* **2020**.

(14) Wu, Y.; Wu, D.; Zhao, H.; Li, J.; Li, X.; Wang, Z.; Wang, H.; Zhu, F.; Xu, B. Synthesis and Properties of Hyperbranched Polymers for Polymer Light Emitting Devices with Sunlight-Style White Emission. *RSC Adv.* **2019**.

(15) Wang, Z.; Wang, C.; Gan, Q.; Cao, Y.; Yuan, H.; Hua, D. Donor-Acceptor-Type Conjugated Polymer-Based Multicolored Drug Carriers with Tunable Aggregation-Induced Emission Behavior for Self-Illuminating Cancer Therapy. *ACS Appl. Mater. Interfaces* **2019**.

(16) Zheng, C.; Zhong, C.; Collison, C. J.; Spano, F. C. Non-Kasha Behavior in Quadrupolar Dye Aggregates: The Red-Shifted H-Aggregate. *J. Phys. Chem. C* **2019**.

(17) Spano, F. C. The Spectral Signatures of Frenkel Polarons in H- And J-Aggregates. *Acc. Chem. Res.* **2010**.

(18) Spano, F. C.; Silva, C. H- and J-Aggregate Behavior in Polymeric Semiconductors. *Annu. Rev. Phys. Chem.* **2014**.

(19) Terenziani, F.; Painelli, A.; Katan, C.; Charlot, M.; Blanchard-Desce, M. Charge Instability in Quadrupolar Chromophores: Symmetry Breaking and Solvatochromism. *J. Am. Chem. Soc.* **2006**.

(20) Seo, J. H.; Namdas, E. B.; Gutacker, A.; Heeger, A. J.; Bazan, G. C. Solution-Processed Organic Light-Emitting Transistors Incorporating Conjugated Polyelectrolytes. *Adv. Funct. Mater.* **2011**.

(21) Usta, H.; Sheets, W. C.; Denti, M.; Generali, G.; Capelli, R.; Lu, S.; Yu, X.; Muccini, M.; Facchetti, A. Perfluoroalkyl-Functionalized Thiazole-Thiophene Oligomers as N-Channel Semiconductors in Organic Field-Effect and Light-Emitting Transistors. *Chem. Mater.* **2014**.

(22) Gwinner, M. C.; Kabra, D.; Roberts, M.; Brenner, T. J. K.; Wallikewitz, B. H.; McNeill, C. R.; Friend, R. H.; Sirringhaus, H. Highly Efficient Single-Layer Polymer Ambipolar Light-Emitting Field-Effect Transistors. *Adv. Mater.* **2012**.

(23) Capelli, R.; Toffanin, S.; Generali, G.; Usta, H.; Facchetti, A.; Muccini, M. Organic Light-Emitting Transistors with an Efficiency That Outperforms the Equivalent Light-Emitting Diodes. *Nat. Mater.* **2010**.

Chapter 3

Developing Coiled Semi-Ladder Polymer Systems for use in Multi-Layered OLET Devices

3.1 Background

The previous chapter described how semi-ladder polymer systems employed in concert with multi-layered OLET devices could yield promising results. More specifically, we employed an electron-deficient thieno[2',3':5,6]pyrido[3,4-g]thieno[3,2-c]isoquinoline-5,11(4H,10H)-dione (TPTI) and thieno[2',3':4,5]pyrido[2,3-g]thieno[3,2-c]quinoline-4,10-dione (TPTQ) based ladder-type system as comonomers in a linear semi-ladder polymer system. We found that all four of our synthesized polymers were electroluminescent. Additionally, for one of our polymeric systems (TPTI-F), we obtained an excellent EQE of 2.8%, which is among the highest in solution-processed OLET devices. [1,2]

The TPTI monomer employed exhibits a structure in which the carbonyl group connects to the central benzene ring, which tuned the electron density distribution, as shown in **Figure 3.1**. The orientation of amide bonds in TPTI was then altered synthetically, which will change the electronic properties of the resulting electron-accepting monomer TPTQ. This molecule is a positional isomer of our previously synthesized TPTI monomer. In TPTQ, the amide linkage

positioning is switched, and the carbonyl group of the amide bond is now linked to peripheral thiophene instead of the central phenyl ring.

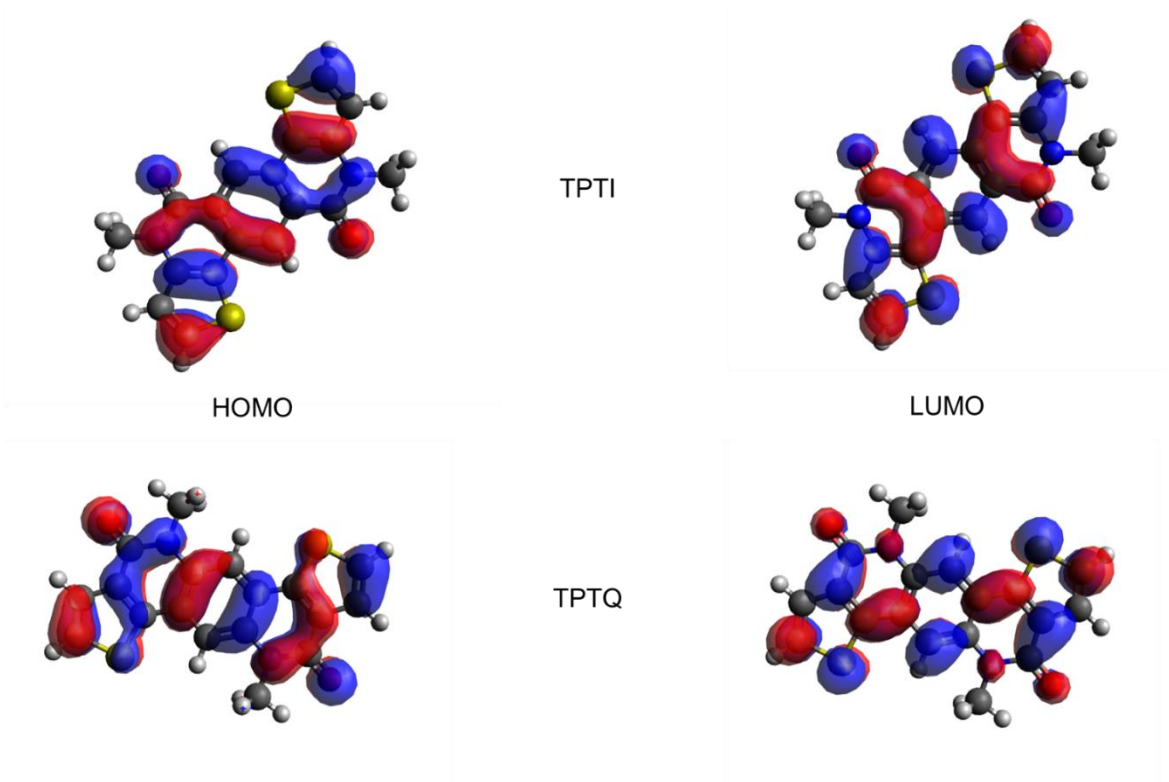

Figure 3.1: DFT results for TPTI and TPTQ small molecules

To further understand the structure-property relationship within this semi-ladder polymer system, we synthesized both monomers and copolymerized them with carbazole. In contrast with the carbazole monomer employed in the previous chapter, we functionalized the carbazole monomers here with Bpin moiety at 3 and 6 positions, para to the carbazole N. This would make the resulting polymers coiled and give them dramatically different optoelectronic properties as we will describe below. Then we will employ these polymers in multi-layered solution-processed OLET devices.

3.2 Results and Discussion

3.2.1 Synthesis

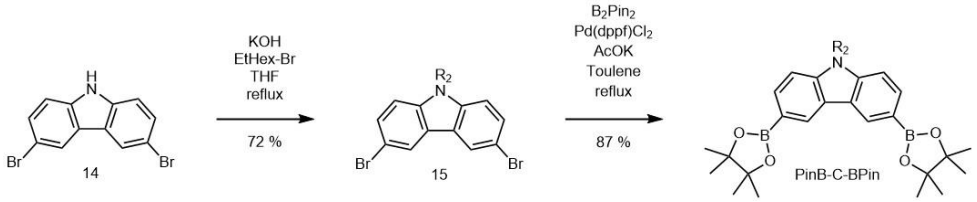

Scheme 3.1: Synthesis of carbazole comonomer

The synthetic strategy for dibrominated TPTI and dibrominated TPTQ monomers is shown in **Schemes 2.1 and 2.2** in Chapter 2 and is described there. The synthetic scheme for the carbazole comonomer is shown here (**Scheme 3.1**). [3–5] It is virtually identical to that of the carbazole comonomer in the previous chapter except for the bromines' positioning in the starting carbazole. Once we synthesized all three comonomers, we set up the Suzuki coupling condensation reaction, as shown in **Scheme 3.2**. The difference between these two polymers from those in Chapter 2 is in the weak intramolecular pi-pi interaction. Here the positioning of the starting carbazole was such that it forced the resulting polymers into coiled foldamers. Additionally, the HOMO of the resulting polymers will be closer to the HOMO of the donor monomer (carbazole), and the LUMO of the polymer will be closer to the LUMO of the accepting monomer (TPTI/TPTQ).

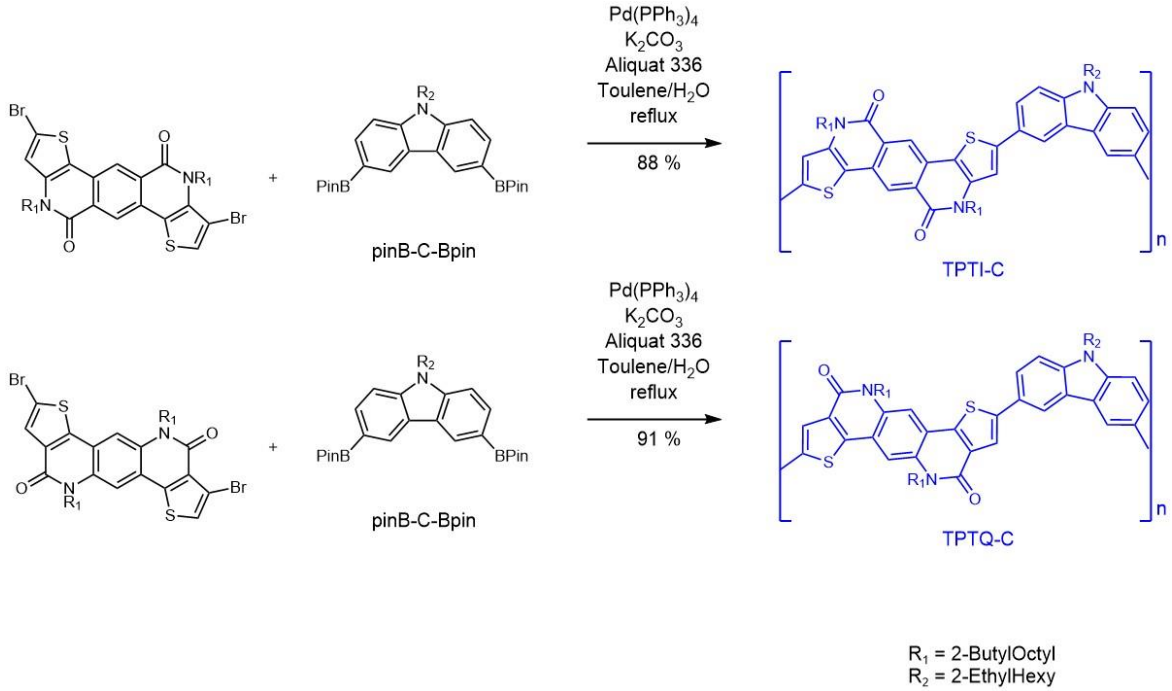

Scheme 3.2: Synthesis of coiled polymers

3.2.2 Basic Characterizations

Table 3.1: Physical and Optoelectronic properties of coiled polymers

Polymer	HOMO (eV)	LUMO (eV)	Bandgap E_g (eV)	PLQY (%)	M_w	M_n	PDI
TPTI-C	-5.11[a]/-4.77[b]	-3.09[d]/-1.78[b]	2.99[b]/2.02[c]	21	17797	14070	1.26
TPTQ-C	-5.44[a]/-5.03[b]	-3.19[d]/-2.41[b]	2.62[b]/2.25[c]	30	91767	32823	2.80

[a] Measured from the cyclic voltammetry, [b] Bandgap E_g calculated from DFT, [c] Bandgap E_g calculated from the onset of the film absorption, [d] LUMO energy levels are calculated as HOMO of the polymer from CV + E_g from the onset of film absorption

Following synthesis, we obtained polymer molecular weights and polydispersity indices (PDI) by employing gel-permeation chromatography (GPC). Both the polymers here exhibited sufficient molecular weights and relatively narrow polydispersity indices (PDI) (**Table 3.1**). However, there were significant differences between the two polymers: For instance, polymer TPTQ-C had a weight-average molecular weight of around 92000 Daltons, five times higher than its TPTI counterpart. Similarly, TPTQ-Cs' PDI was twice in magnitude than that of TPTI-C. Additionally, all of the polymers were soluble in common organic solvents.

PLQYs' of both our coiled polymers here are relatively low and are around the same magnitude as their non-coiled counterparts synthesized in the previous chapter. None the less, the highest PLQY obtained in this series of polymers is 30%, which is around 50% lower than that of TPTQ-F synthesized previously. We calculated the HOMO/LUMO energy levels and the polymer

system bandgaps based on the onset of the oxidation potential of thin films in Cyclic Voltammetry and the optical bandgap based on the onset absorbance in the UV-Vis absorbance spectra of thin films (**Table 3.1**). The experimentally calculated bandgap of TPTQ-C is 0.23 eV higher than its TPTI counterpart. Additionally, identical to the trend established in the previous chapter, HOMO/LUMO orbital energies of TPTQ-C polymer are downshifted relative to its TPTI counterpart. This corresponds to the stronger electron-withdrawing ability of TPTQ. [6–8]

3.2.3 DFT Results

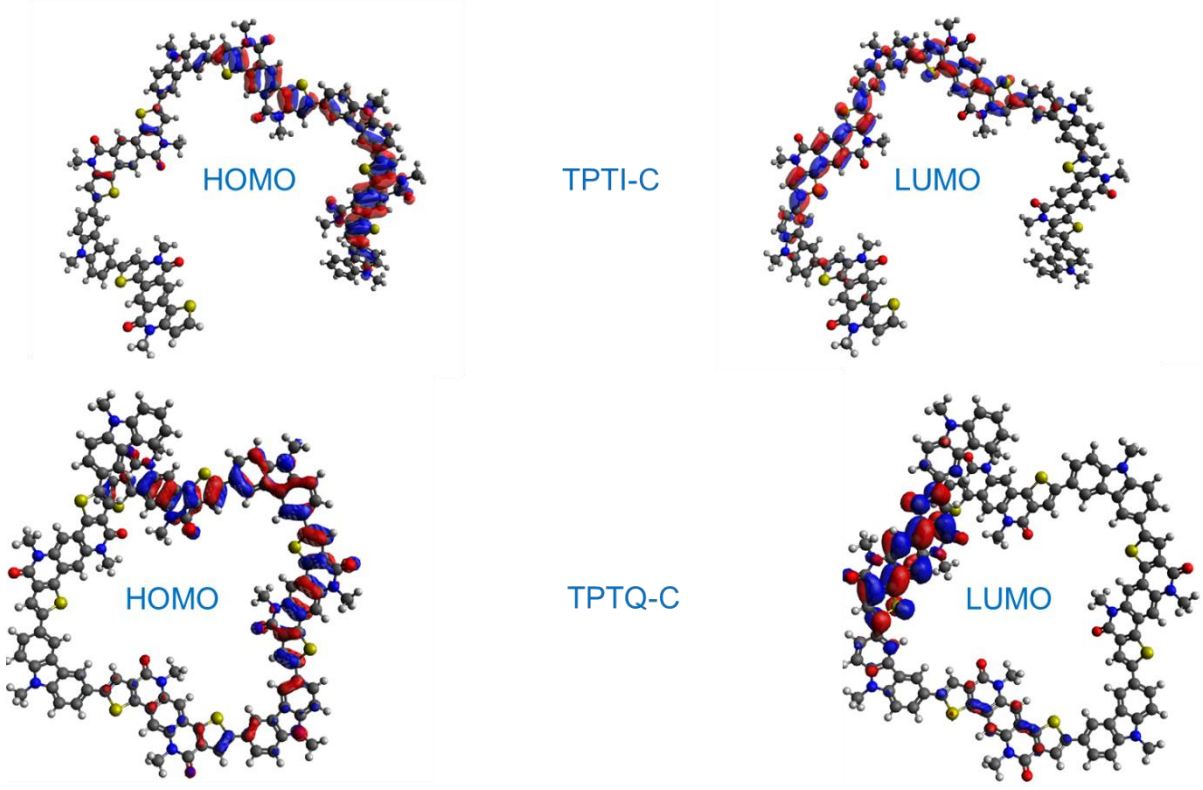

Figure 3.2: DFT results for coiled polymers

A similar trend is observed for DFT (B3LYP method employing 6-31g** basis set) calculated energy levels and bandgaps. DFT optimized molecular geometries (**Figure 3.2**) confirm that while all four polymers described previously exhibit linear structures, polymers TPTI-C and TPTQ-C behave as coiled foldamers. Polymer TPTI-C exhibits highly delocalized frontier

molecular orbitals, which extend over four out of eight monomers units in the structure. Frontier molecular orbital distribution for TPTQ-C, however, is drastically different. While TPTQ-C has a HOMO delocalized over five monomer units, its LUMO appears highly localized over a single TPTQ monomer unit.

3.2.4 Optical Characterizations

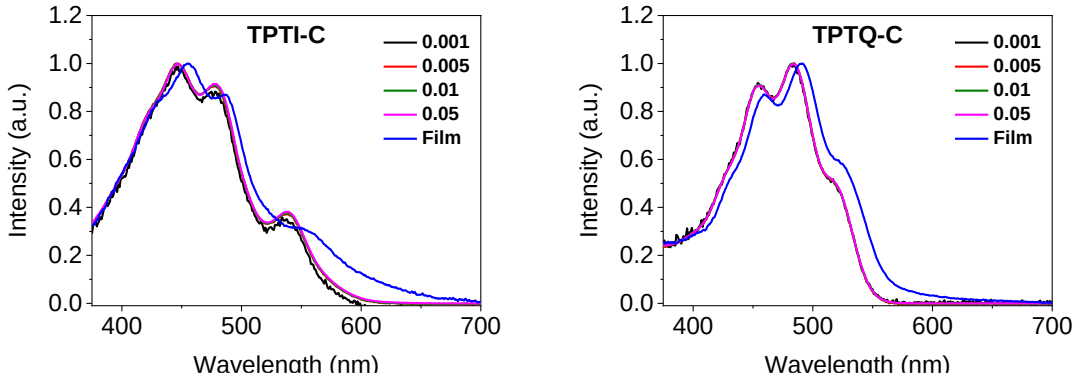

Figure 3.3: UV-Vis absorption spectra for coiled polymers

We recorded the UV-Vis absorption spectra at different concentrations for both of our polymers (**Figure 3.3**). Polymer TPTQ-C has intense absorption around 375 to 600 nm range, while the polymer TPTI-C exhibits a slightly red-shifted spectrum in the range 375 to 700 nm. The shape of the film absorption spectra is similar, albeit a bit broadened, to their solution analogs for reasons described previously. The solution absorption spectra of TPTI-C exhibits three concentration-independent absorption peaks at 447, 478, and 539 nm, which correspond to 0-2, 0-1, and 0-0 transitions, respectively. These peaks are slightly red-shifted in TPTI-C thin film. Additionally, while the I_A^{0-0}/I_A^{0-1} ratio remains unchanged, the I_A^{0-1}/I_A^{0-2} ratio decreases in solid-state.

TPTQ-C also exhibits concentration-independent solution spectra with 0-1 as the most intense peak followed by 0-2 and 0-0 peaks. This indicates that H-aggregation exists even at the

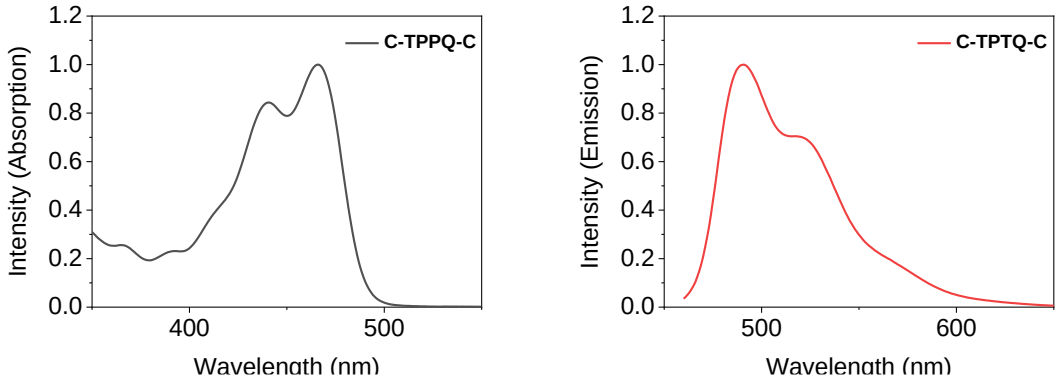

Figure 3.4: UV-Vis absorption and Emission spectra for TPTQ model compound

level of a single polymer chain, which is evidence for polymer folding, as demonstrated in our previous work. [9] As discussed previously, this is also supported by our DFT calculations. To further support this conclusion, we synthesized a dimer model compound where the central TPTQ moiety connects to two carbazoles in the same position as in the polymer TPTQ-C. These molecules do not have folded helical structures; however, they still exhibit a strong 0-0 transition in dilute solutions (**Figure 3.4**). For this reason, the UV-Vis absorption spectrum for TPTQ-C indicates the formation of H-aggregates at the level of a single polymer chain, which is only possible in folded conformation. Its thin-film spectrum, additionally, is slightly red-shited with a slight increase in the $I_{0\text{-}0/0\text{-}1}$ ratio.

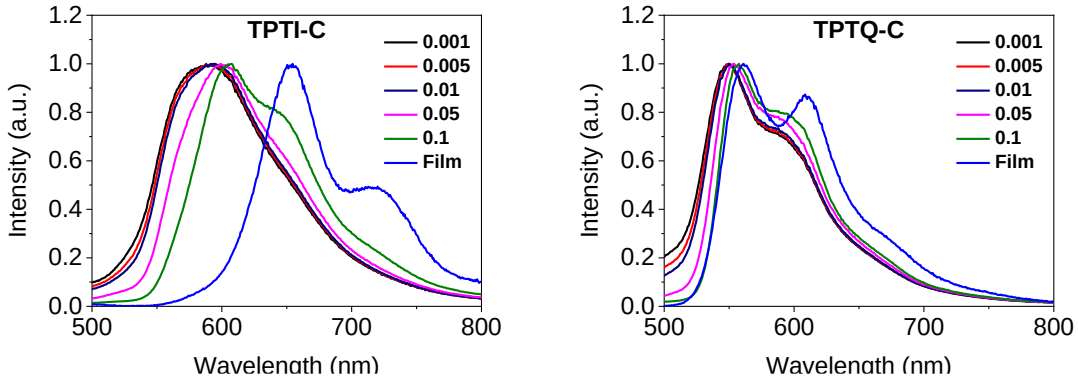

Figure 3.5: Emission spectra for coiled polymers

We also performed concentration-dependent photoluminescence measurements (**Figure 3.5**) to understand polymeric aggregation and to gather further evidence for our hypothesis. For

TPTI-C, the 0-0 and 0-1 emission peaks are slightly red-shifted with increasing concentration to 605 and 647 nm. Moreover, the I_A^{0-0}/I_A^{0-1} ratio decreases gradually with increasing concentration, with the 0-0 peak disappearing entirely in the solid-state thin film. This is consistent with H-aggregation. [10–12]

Emission spectra of TPTQ-C exhibit slight red-shifts with increasing concentration and are further red-shifted in thin-films. The 0-1 transition peaks are evident in even the most dilute solutions, and their intensity increases with increasing concentration and then further in thin-films. This seems to contradict the formation of H-aggregates, which generally exhibits blue-shifts with increasing concentration. However, as discussed in the previous chapter, compounds exhibiting quadrupole interactions can exhibit red-shits in H-aggregates. [10–12]

Table 3.2: Time-resolved fluorescence decay measurements for coiled polymers

Polymer	**τ1 (ns)**	**Fraction 1 (%)**	**τ2 (ns)**	**Fraction 2 (%)**
TPTI-C	1.42	74	0.48	26
TPTQ-C	2.14	100		

We performed time-resolved fluorescence decay measurements on our polymer solutions (**Table 3.2**). Following the measurements, we incorporated fluorescence decay curves on our raw data and calculated fluorescence lifetimes. Polymer TPTQ-C was found to exhibit a first-order exponential decay curve (lifetime = 2.14 ns). Polymer TPTI-C, however, exhibited a second-order exponential decay behavior indicating at least two relaxation pathways. In both cases, the first fluorescence lifetime values, at least, seemed to be consistent with H-aggregated foldamers in which exciton delocalization extends the lifetime.

3.2.5 GIWAX Results

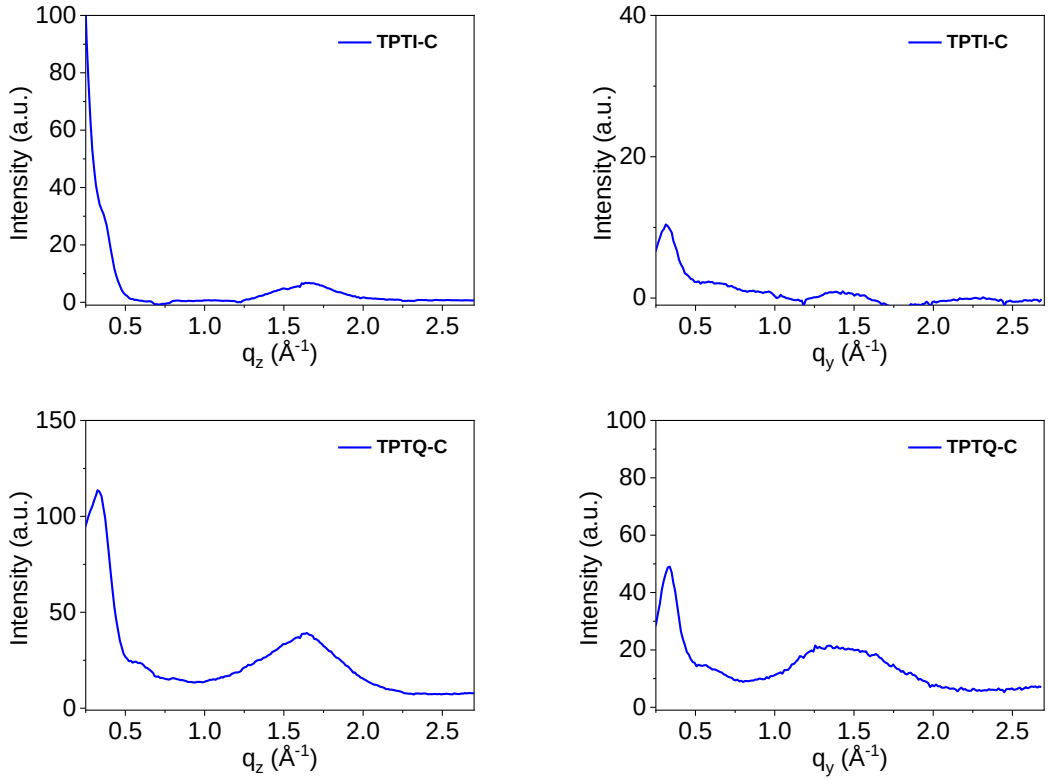

Figure 3.6: Linecuts of 2D GIWAX profiles for coiled polymers

Additionally, we performed Grazing-incidence wide-angle X-ray scattering (GIWAXS) experiments to elucidate additional molecular packing information. The linecuts of their 2D scattering profiles along in-plane and out-of-plane orientations are shown in **Figure 3.6**. Our studies suggest that polymer TPTI-C exhibits weak crystallinity with loose molecular packing: TPTI-C had pi-pi stacking distances of 3.9 Å. Loose molecular packing is consistent with H-aggregation in which branched alkyl chains on the TPTI moiety are in close contact with each other. Polymer TPTQ-C is also relatively amorphous, with a slight preference for face-on packing. Again these results were consistent with previously determined intramolecular H-aggregation.

3.3 Device Fabrication

3.3.1 OFET Fabrication

Table 3.3: Charge carrier mobility values for coiled polymers

Material	μ_h ($cm^2V^{-1}s^{-1}$)	μ_e ($cm^2V^{-1}s^{-1}$)
TPTI-C[a]	–	1.9×10^{-6}
TPTQ-C[a]	6.9×10^{-5}	-
TPTI-C[b]	2.4×10^{-2}	1.6×10^{-2}
TPTQ-C[b]	3.5×10^{-1}	5.1×10^{-1}

a Mobility calculated from OTS modified OFET devices; b Mobility calculated from OTS modified OLET devices.

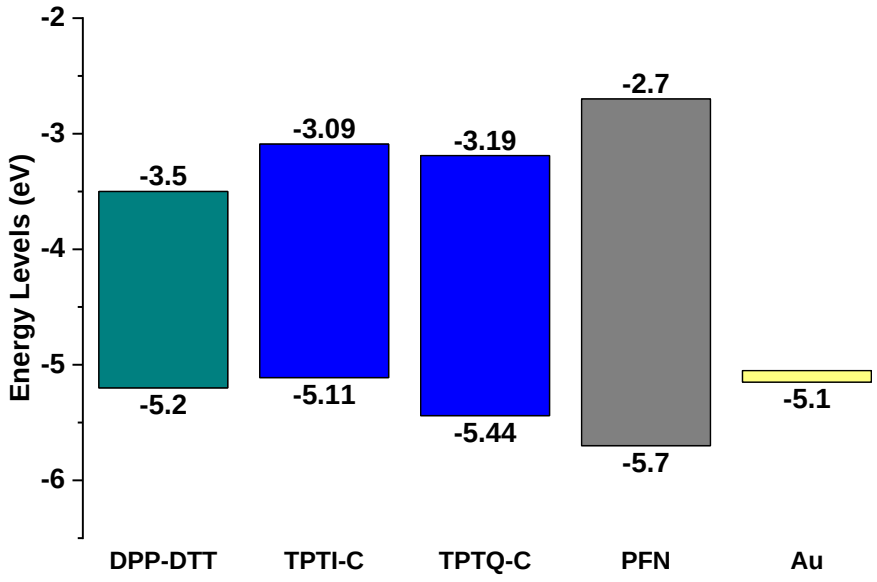

Figure 3.7: Energy Level diagram for coiled polymers

Before we fabricated any OLET device, it was necessary to quantify our polymeric materials' charge carrier mobilities. For this reason, we fabricated single-layered bottom-gate top-contact OFET devices with gold as source-drain electrodes and measured their mobilities (**Table 3.3**). Unfortunately, neither TPTI-C not TPTQ-C exhibits any form of ambipolar behavior in their OFET devices. Additionally, charge carrier mobilities for both polymers in single-layered devices are very poor. We noticed that the charge injection energy barrier for electrons is much higher than the energy barrier for holes (**Figure 3.7**). The work function of gold is -5.1 eV, which is better aligned with the HOMO energy levels where the hole injection occurs, rather than with the LUMO energy levels, which participate in electron injection. For these two reasons, neither of the devices exhibited any emission.

3.3.2 OLET Fabrication

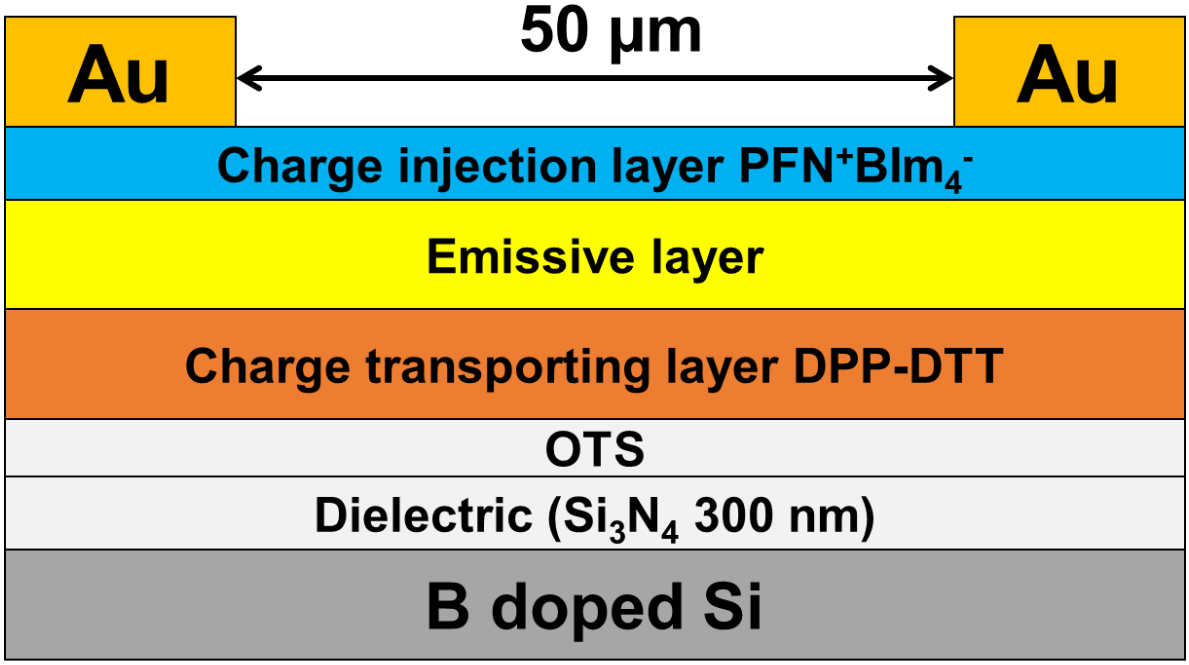

Figure 3.8: OLET Device architecture for coiled polymers

To address this issue, we employed a bottom-gate top-contact (BG-TC) device architecture to fabricate our OLET devices with a channel length (L) of 50 μm and channel width (W) of 18.2 mm. We fabricated these multi-layered solution-processed devices incorporating an electron injection layer, a charge transporting layer, an emissive layer, and a self-assembled monolayer (SAM) in a Si/Si_3N_4/OTS/DPP-DTT/Emissive layer/PFN^+BIm4^-/Au device geometry (**Figure 3.8**). Here, we employed p-doped silicon as a gate, followed by a high dielectric constant silicon nitride as a dielectric layer. Then *n*-octadecyltrichlorosilane was deployed as a SAM on top of Si_3N_4 through vapor deposition at 120 °C in a vacuum oven. This modification layer was necessary for two reasons: First, it would help reduce charge trapping. Second, it would help improve molecular stacking. Then we employed high mobility Poly[2,5-(2-octyldodecyl)-3,6-diketopyrrolopyrrole-alt-5,5- (2,5-di(thien-2-yl)thieno [3,2-b]thiophene)] (DPP-DTT) as a charge transporting layer which was followed by our semi-ladder polymer emissive layer. We coated this layer from the solvents orthogonal to those that dissolve DPP-DTT and then annealed at 100 °C. [13]

DPP-DTT layer was necessary as our emissive layer had low intrinsic mobility, which would have been detrimental to device performance. Additionally, the HOMO of DPP-DTT matches well with the HOMO of the emissive layers, which should facilitate hole injection. From the energy level diagram (**Figure 3.7**), it is clear that the LUMO energy levels of our emissive layer were aligned too high relative to the work function of Au. This meant that the electron injection energy barrier could be as high as 2.0 eV. For this reason, we employed [9,9′ -bis [6″-(N, N,N-trimethylammonium) hexyl] fluorene-alt-co-phenylene] tetrakis (imidazolyl) borate (PFN^+ $BIm4^-$) as an electron injection layer whose ionic effect lowered the electron injection barrier. [14] This was followed by vacuum depositing gold as source-drain electrodes.

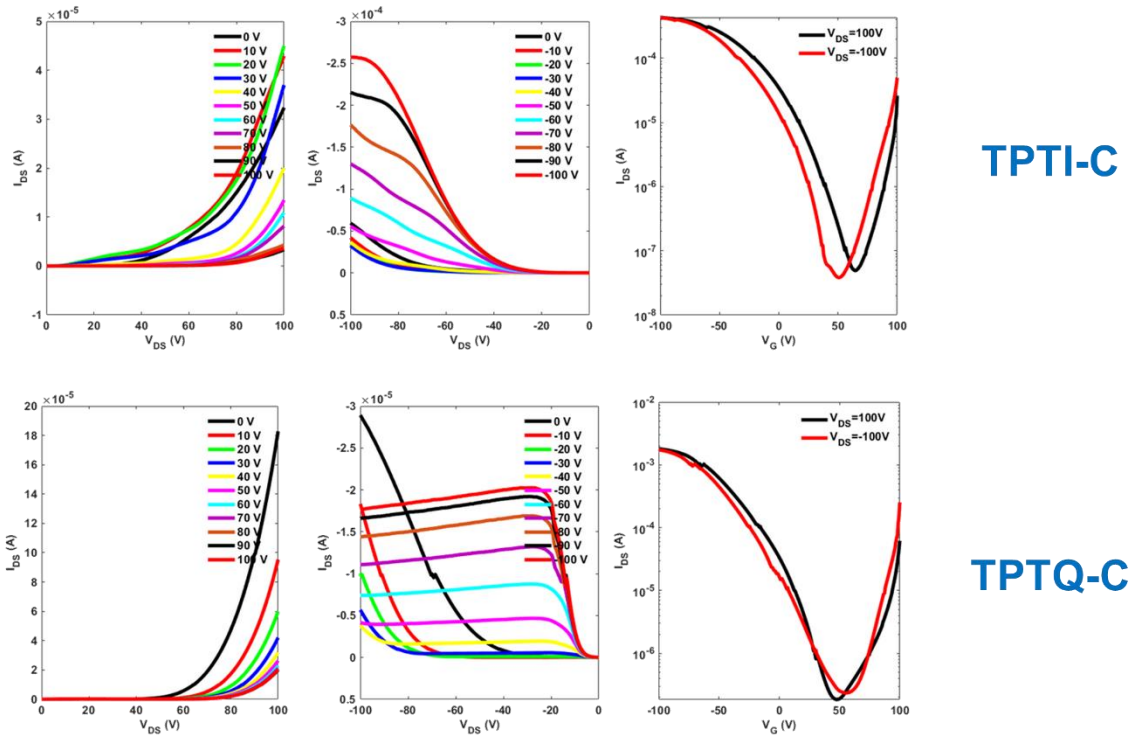

Figure 3.9: Transfer and output curves for coiled polymers

We measured the source-drain current-voltage curves at both negative and positive gate voltages to understand electron and hole transport. The V-shaped transfer curves in **Figure 3.9** indicate that all of our devices exhibit ambipolar charge transport behavior. Fortunately, as is evident in **Table 3.3**, the charge transport is relatively balanced with mobilities several orders of magnitude larger than for single-layered devices. It is clear that charge transport in the device occurs primarily at the interface between DPP-DTT and Si_3N_4.

More importantly, both devices exhibited strong emission, albeit near the drain electrodes instead of the channels' middle (**Figure 3.10**). Of the two polymers, TPTQ-C exhibits the brightest emission (200 nW), equivalent to the highest performing devices fabricated by Capelli. [15] This is a significant difference from the TPTI/TPTQ system, in which the linear polymer TPTI-F exhibits the best performance. This polymer is known to form a folded structure, which helps avoid

emission quenching due to weak aggregation. It is clear that such foldamers offer a compromise between charge carrier mobility and light emission towards achieving optimized device performance. Additional investigation into the light emission revealed that all three polymers' electroluminescence spectra were very similar to their corresponding photoluminescence spectra. This similarity suggests that emissive centers for photoluminescence and electroluminescence are similar if not identical.

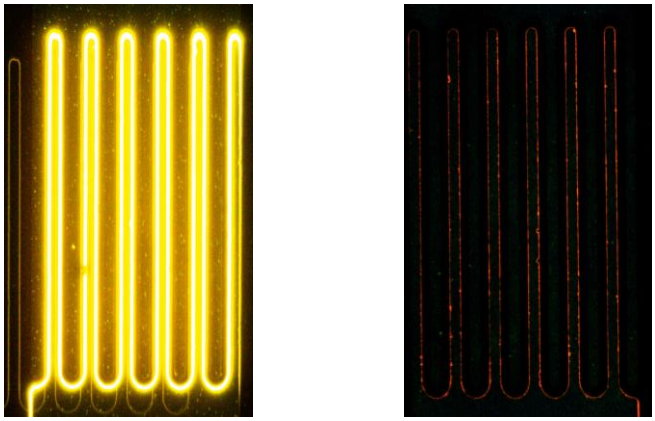

Figure 3.10: Electroluminiscence for coiled polymers

We calculated the EQE of our devices by measuring the calibrated reverse-biased photodiodes' photocurrent (**Figure 3.11**). This was done along the gate voltages corresponding to the brightest emission mode in these devices (+20 to -100 V). One can observe three distinct light-emitting modes in such systems. When employing positive gate voltages, light emission is observed as a consequence of major charge carrier electrons recombining with minor charge carrier holes. Decreasing the gate voltage also decreases the number of injected charge carriers, reducing light emission intensity. As the gate voltages approach negative values, major/minor carrier roles are reversed, with hole transport becoming the dominant mode. None the less, both devices

exhibited very low EQEs around 10^{-3}%. However, this EQE stays roughly constant over a wide voltage range, which is a plus because EQE tends to decrease at voltages that are either very high or very low.

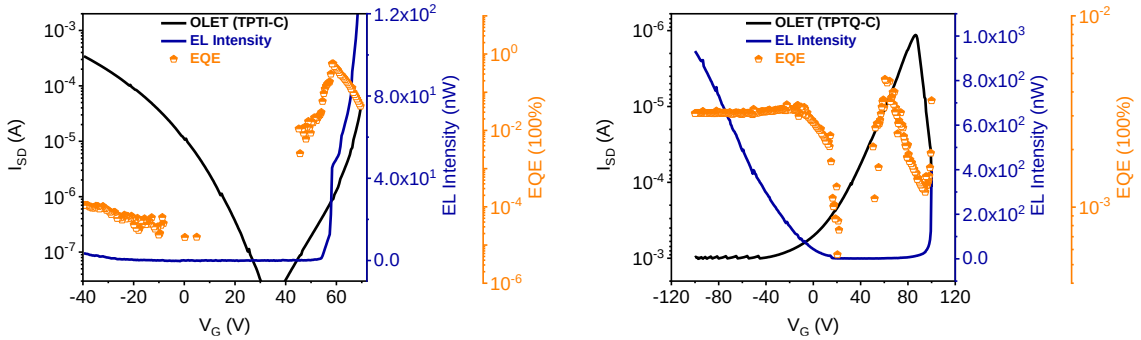

Figure 3.11: EQE and EL intensity for coiled polymers

3.4 Conclusion

In this work, we established that D-A semi-ladder copolymer TPTQ-C exhibits a coiled foldamer structure due to strong non-covalent interactions. Ring fusion in semi-ladder systems introduces some degree of planarity that extends effective conjugation length, leading to more controllable bandgaps, better delocalization of frontier molecular orbitals, and by extension, better intramolecular charge transport. The emission intensity of TPTQ-C validates this assertion. Also, foldamers force the polymer to self-assemble in a coiled fashion with substantial intramolecular orbital overlap and, by extension, improving charge transport. Thus, it is not surprising that the resulting device exhibits balanced emission and mobility, both of which are necessary for satisfactory device performance. EL intensity of the OLETs is strong, a direct consequence of the molecular structure of the active layer as well as device architecture. Our results clearly indicate that employing a coiled foldamer is a promising design strategy for optoelectronic materials.

3.5 Materials and Methods

See the previous chapter

3.5.1 Synthesis

Br-TPTI-Br: See the previous chapter

Br-TPTQ-Br: See the previous chapter

C-TPTQ-C: Br-TPTQ-Br (1 eq), Carbazole-BPin (3 eq), K_2CO_3 (4 eq), Aliquat 336 (3 drops), and $Pd(PPh_3)_4$ (0.05 eq) were dissolved in 6ml of Toluene/H_2O (10:1). The mixture was degassed for 30 minutes and refluxed overnight. After cooling to room temperature, the mixture was poured into water and extracted with DCM. The organic layer was dried with $MgSO_4$, and the solvent was removed under reduced pressure. The crude mixture was purified by column chromatography on silica gel with hexane:ethyl acetate (9:1) to get a yellow-green compound in a 56% yield. ^{1}H-NMR (500 MHz, CDCl3): δ (ppm) 8.27 (s, 2H), 8.06 (d, 2H). 7.94 (s, 2H), 7.73 (d, 2H), 7.59 (s, 2H), 7.47 (t, 2H), 7.33 (m, 6H), 4.43 (br, 4H), 4.03 (d, 4H), 2.06 (m 4H), 1.11-1.61 (m, 64 H), 0.86 (m, 24H). MS (MALDI-TOF) *m*/*z* 1327.94 (M+), calcd 1328.06.

General Procedure for Semi-Ladder Copolymers: A mixture of Br-TPTI-Br/ Br-TPTQ-Br monomer (1 eq) and Carbazole comonomer (1 eq), K_2CO_3 (4 eq), Aliquat 336 (3 drops), and $Pd(PPh_3)_4$ (0.05 eq) were dissolved in 4ml of Toluene/H_2O (10:1). The mixture was degassed for 30 minutes and then refluxed for 72 hours. After cooling to room temperature, the mixture was passed through Celite and precipitated in methanol. The polymer fibers were then washed by Soxhlet extraction with methanol, acetone, hexanes, and chloroform. The final polymer was obtained after reprecipitation of chloroform fraction in methanol.

TPTI-C: Yield: 88 %. ^{1}H-NMR (500 MHz, $C_2D_2Cl_4$): δ (ppm) 6.6-9.0 (br, 10H), 3.50-5.20 (br, 6H), 1.98-2.34 (br, 3H), 1.16-1.74 (m, 40H), 0.72-1.11 (m, 18H). Elemental Analysis calculated for $[C_{60}H_{79}N_3O_2S_2]n$: C: 76.79; H: 8.49; N: 4.48. Found: C: 75.46; H: 8.47; N: 4.28.

TPTQ-C: Yield: 91 %. ^{1}H-NMR (500 MHz, C2D2Cl4): δ (ppm) 6.84-8.66 (br, 10H), 4.67-5.42 (br, 2H), 3.55-4.68 (br, 4H), 1.96-2.32 (m, 3H), 1.17-1.87 (m, 40H), 0.68-1.08 (m, 18H). Elemental Analysis calculated for $[C_{60}H_{79}N_3O_2S_2]n$: C: 76.79; H: 8.49; N: 4.48; O: 3.41; S: 6.83. Found: C: 75.75; H: 8.67; N: 4.21.

3.5.2 Optical analysis

See the previous chapter

3.5.3 X-ray analysis

See the previous chapter

3.5.4 Device Fabrication

See the previous chapter

3.5.5 Device Measurements

See the previous chapter

3.6 References

(1) Yuan, D.; Awais, M. A.; Sharapov, V.; Liu, X.; Neshchadin, A.; Chen, W.; Yu, L. Highly Emissive Semi-Ladder-Type Copolymers, Aggregation State, and Solution-Processed Organic Light-Emitting Transistor. *Chem. Mater.* **2020**.

(2) Yuan, D.; Awais, M. A.; Sharapov, V.; Liu, X.; Neshchadin, A.; Chen, W.; Bera, M.; Yu, L. Foldable Semi-Ladder Polymers: Novel Aggregation Behavior and High-Performance Solution-Processed Organic Light-Emitting Transistors. *Chem. Sci.* **2020**.

(3) Jin, M.; Zhu, Z. C.; Liao, Q. Y.; Li, Q. Q.; Li, Z. Dendronized Polymers with High FTC-Chromophore Loading Density: Large Second-Order Nonlinear Optical Effects, Good Temporal and Thermal Stability. *Chinese J. Polym. Sci. (English Ed.* **2020**.

(4) Wu, Y.; Wu, D.; Zhao, H.; Li, J.; Li, X.; Wang, Z.; Wang, H.; Zhu, F.; Xu, B. Synthesis and Properties of Hyperbranched Polymers for Polymer Light Emitting Devices with Sunlight-Style White Emission. *RSC Adv.* **2019**.

(5) Wang, Z.; Wang, C.; Gan, Q.; Cao, Y.; Yuan, H.; Hua, D. Donor-Acceptor-Type Conjugated Polymer-Based Multicolored Drug Carriers with Tunable Aggregation-Induced Emission Behavior for Self-Illuminating Cancer Therapy. *ACS Appl. Mater. Interfaces* **2019**.

(6) Jung, I. H.; Lo, W.; Jang, J.; Chen, W.; Landry, E. S.; Lu, L.; Talapin, D. V; Yu, L.; Zhao, D. Synthesis and Search for Design Principles of New Electron Accepting Polymers for All-Polymer Solar Cells Synthesis and Search for Design Principles of New Electron Accepting Polymers for All-Polymer Solar Cells. **2014**.

(7) Carlotti, B.; Cai, Z.; Kim, H.; Sharapov, V.; Madu, I. K.; Zhao, D.; Chen, W.; Zimmerman, P. M.; Yu, L.; Goodson, T. Charge Transfer and Aggregation Effects on the Performance of Planar vs Twisted Nonfullerene Acceptor Isomers for Organic Solar Cells. *Chem. Mater.* **2018**.

(8) Jung, I. H.; Zhao, D.; Jang, J.; Chen, W.; Landry, E. S.; Lu, L.; Talapin, D. V.; Yu, L. Development and Structure/Property Relationship of New Electron Accepting Polymers Based on Thieno[2′,3′:4,5]Pyrido[2,3-g]Thieno[3,2-c]Quinoline-4,10-Dione for All-Polymer Solar Cells. *Chem. Mater.* **2015**, *27* (17), 5941–5948.

(9) Fauvell, T. J.; Zheng, T.; Jackson, N. E.; Ratner, M. A.; Yu, L.; Chen, L. X. Photophysical and Morphological Implications of Single-Strand Conjugated Polymer Folding in Solution. *Chem. Mater.* **2016**.

(10) Zheng, C.; Zhong, C.; Collison, C. J.; Spano, F. C. Non-Kasha Behavior in Quadrupolar Dye Aggregates: The Red-Shifted H-Aggregate. *J. Phys. Chem. C* **2019**.

(11) Spano, F. C. The Spectral Signatures of Frenkel Polarons in H- And J-Aggregates. *Acc. Chem. Res.* **2010**.

(12) Spano, F. C.; Silva, C. H- and J-Aggregate Behavior in Polymeric Semiconductors. *Annu. Rev. Phys. Chem.* **2014**.

(13) Li, J.; Zhao, Y.; Tan, H. S.; Guo, Y.; Di, C. A.; Yu, G.; Liu, Y.; Lin, M.; Lim, S. H.; Zhou, Y.; et al. A Stable Solution-Processed Polymer Semiconductor with Record High-Mobility for Printed Transistors. *Sci. Rep.* **2012**.

(14) Seo, J. H.; Namdas, E. B.; Gutacker, A.; Heeger, A. J.; Bazan, G. C. Solution-Processed Organic Light-Emitting Transistors Incorporating Conjugated Polyelectrolytes. *Adv. Funct. Mater.* **2011**.

(15) Capelli, R.; Toffanin, S.; Generali, G.; Usta, H.; Facchetti, A.; Muccini, M. Organic Light-Emitting Transistors with an Efficiency That Outperforms the Equivalent Light-Emitting Diodes. *Nat. Mater.* **2010**.

Chapter 4

Single-Atom Substitution Enhances Efficiency of Multi-Layered OLET Devices

4.1 Background

In the previous chapter, we learned that helical structures are beneficial for emission and charge transport properties in TPTQ based OLET devices. While TPTQ-C exhibited bright emission, its external quantum yield, however, was very poor. One of the reasons for that might have been the presence of heavy atoms such as sulfur in the polymeric system. The heavy atoms essentially induce radiationless intersystem crossing from a vibrationally active singlet (S1) state to an isoenergetic triplet state (T1) as a consequence of spin-orbit coupling. This causes a shift in electron energy levels due to electromagnetic interactions between the electronic spin and the magnetic field generated by electrons' orbit around the nucleus. [1]

Previously, our group had established that replacing N in the center of benzotriazole based 10-ringed ladder molecule with sulfur and then selenium substantially lowered the photoluminescent quantum yield. [2] To put this in perspective, PLQY decreased from 70% in nitrogen-based ladder molecule to 31% and 4% when we replaced just one nitrogen atom in the system with sulfur and then selenium, respectively.

This fluorescence quenching phenomenon, known as the heavy atom effect, was first studied by Perrin in 1926. [3] Since then, it has been explored in meticulous detail by several groups. This phenomenon can happen in two ways: Internal heavy atom effect occurs when the heavy atom is a part of the fluorescent chromophore in question. [4] External heavy atom effect occurs when the heavy atom is distinct from the emissive chromophore. [5]

The internal heavy atom effect has been demonstrated in several previous studies. [6,7] For instance, Klan studied this effect in BODIPY derivatives in detail by measuring fluorescence and intersystem crossing quantum yields as a function of H, Cl, Se, and Te atom substitution. As expected, fluorescence quantum yields decreased with increasing atomic mass as intersystem crossing quantum yields increased. Heavy atoms essentially help increase the rate of intersystem crossing from a short lifetime singlet to a prolonged lifetime triplet state from where the molecule decays non-radiatively. Thus, the ability to flip electronic spin by heavy atoms is intricately tied with their potential for fluorescence quenching.

Therefore, we hypothesized that replacing sulfur atoms in TPTQ will improve OLET performance. For this reason, we synthesized electron-accepting furo[3,2-c]furo[2',3':4,5]pyrido[2,3-g]quinoline-4,10-dione (FFPQ) comonomer. This comonomer is identical to TPTQ except that both the sulfur atoms have been replaced with oxygen. [8,9] By synthesizing furan-based versions of TPTQ polymers, we hoped to improve our systems' device performance and establish structure-property interrelationship.

4.2 Results and Discussion

4.2.1 Synthesis

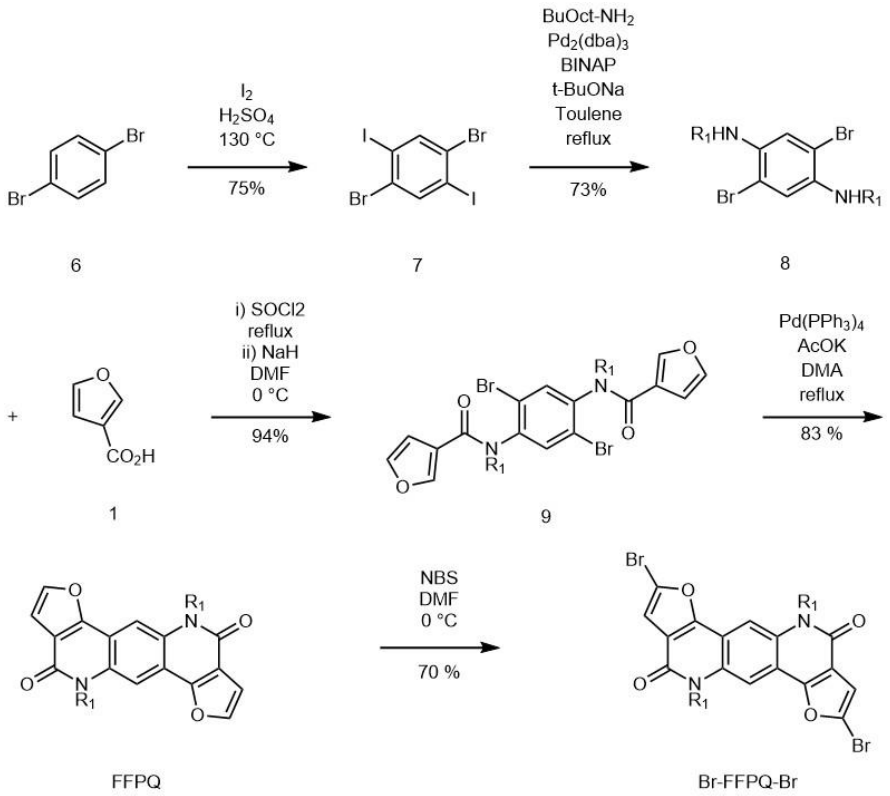

Scheme 4.1: Synthesis of Br-FFPQ-Br

We synthesized our di brominated furo[3,2-c]furo[2',3':4,5]pyrido[2,3-g]quinoline-4,10-dione (FFPQ) monomer following a protocol (**Scheme 4.1**) virtually identical to **Scheme 2.2** employed previously to synthesize di brominated TPTQ in Chapter 2. [10–12] The only difference in the schemes is that we employed the furan equivalent of 3-thiophenecarboxylic acid in the latest iteration of our synthesis. The syntheses of our fluorene/carbazoles-based comonomers are described in **Schemes 2.3** and **3.1** and will not be repeated here. [13–15] Similarly, we employed the Suzuki coupling condensation reaction of electron-withdrawing dibrominated FFPQ with electron-donating carbazoles and fluorene (**Scheme 4.2**) to synthesize our polymers. As in the previous chapters, polymer FFPQ-C is cross conjugated, while polymers FFPQ-CC and FFPQ-F are fully conjugated.

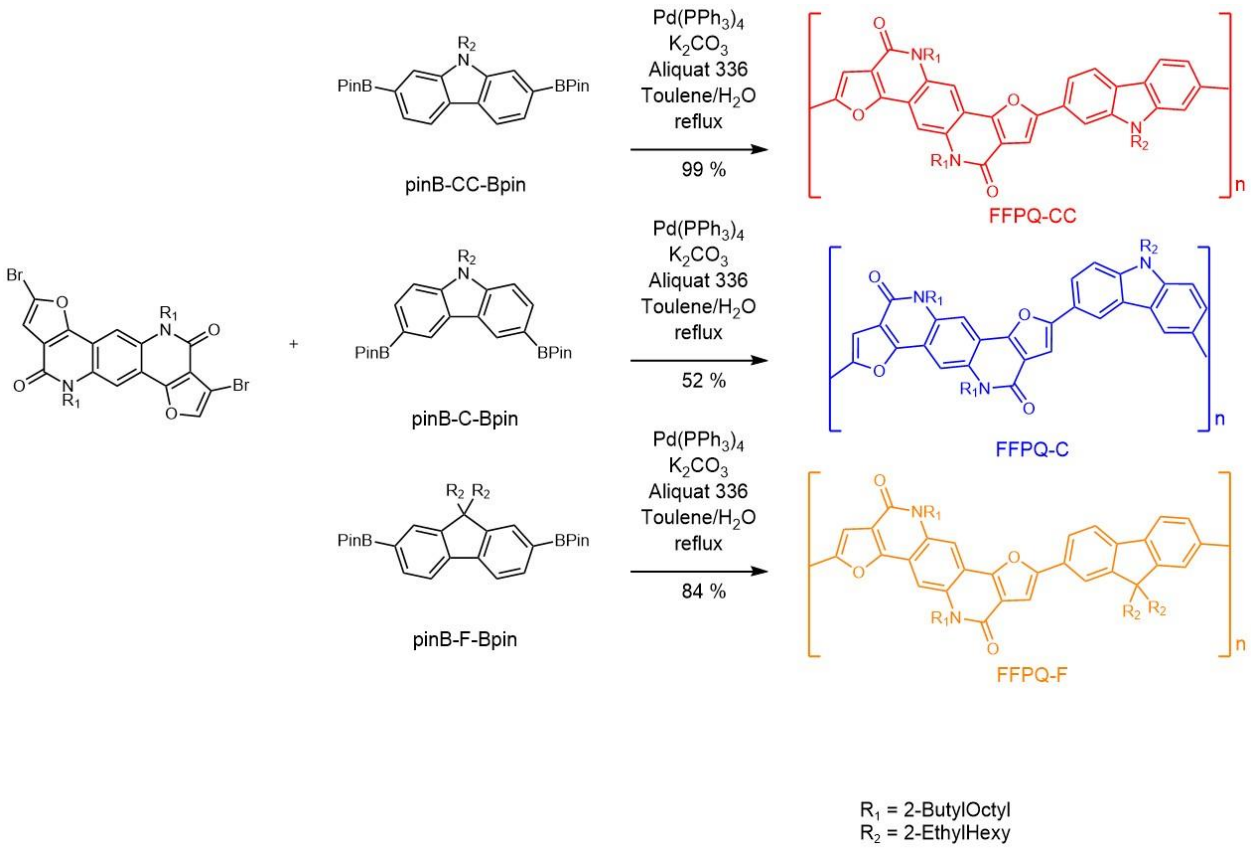

Scheme 4.2: Synthesis of FFPQ polymers

4.2.2 Basic Characterizations

Table 4.1: Physical and Optoelectronic properties of FFPQ polymers

Polymer	HOMO (eV)	LUMO (eV)	Bandgap E_g (eV)	PLQY (%)	M_w	M_n	PDI
FFPQ-CC	-5.48[a]/-5.06[b]	-3.07[d]/-2.23[b]	2.83[b]/2.41[c]	73	20407	14634	1.39
FFPQ-C	-5.42[a]/-4.90[b]	-3.04[d]/-1.92[b]	2.98[b]/2.38[c]	50	50836	28835	1.76

Table 4.1: Physical and Optoelectronic properties of FFPQ polymers *(continued)*

FFPQ-F	-5.67[a]/-5.09[b]	-3.19[d]/-2.32[b]	2.77[b]/2.48[c]	97	33651	29511	1.14

[a] Measured from the cyclic voltammetry, [b] Bandgap E_g calculated from DFT, [c] Bandgap E_g calculated from the onset of the film absorption, [d] LUMO energy levels are calculated as HOMO of the polymer from CV + E_g from the onset of film absorption

The resultant polymers were then characterized, the results of which are summarized in **Table 4.1**. All three polymers were soluble in organic solvents such as toluene, p-xylene, and chloroform. Additionally, GPC results indicated that all three polymers had sizable molecular weights ranging from 20 to 50k daltons with relatively narrow polydispersity indices.

We performed photoluminescence quantum yield measurements on all three of our polymers in dilute chloroform solution. We found that the fluorene based FFPQ-F exhibited the highest quantum yield in this series. However, as opposed to the TPTQ series, the PLQY trend observed for the carbazole polymers in the FFPQ series was the exact opposite, where the linear FFPQ-CC exhibited significantly higher quantum yield than coiled FFPQ-C. As expected, the FFPQ polymers' quantum yields were markedly higher than their corresponding TPTQ counterparts. This was a clear demonstration of the advantages associated with eliminating the internal heavy atom effect. This advantage is best demonstrated in FFPQ-F, which exhibited an impressive 97% photoluminescent quantum efficiency, one of the highest reported in the literature.

As in the previous chapters, we calculated the HOMO energy levels based on thin films' onset oxidation potential in cyclic voltammetry with a ferrocene reference. Compared to the TPTQ series, HOMO/LUMO energy levels and bandgaps were slightly higher for their corresponding

FFPQ polymers. Within the FFPQ series, both carbazole polymers had very similar frontier molecular orbital energy levels and bandgaps. FFPQ-F had HOMO/LUMO energy levels that were shifted slightly lower and bandgap that was marginally higher. This was most likely due to the relatively poor electron donor ability of fluorene compared to carbazole.

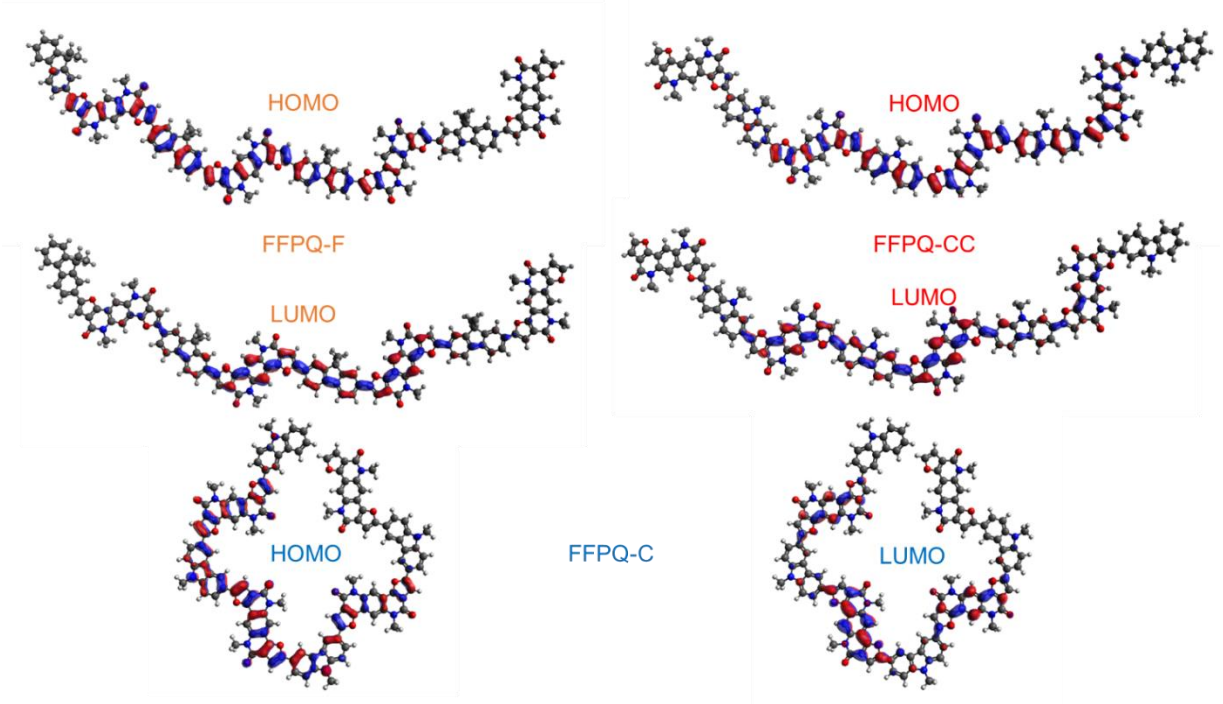

Figure 4.1: DFT results for FFPQ polymers

4.2.3 DFT Results

The DFT calculations based on the B3LYP method employing a 6-31g** basis set indicated that HOMO/LUMO energy levels and bandgaps followed roughly similar trends as experimentally derived results. Additionally, DFT optimized molecular geometries exhibit the same trends as the TPTQ series (**Figure 4.1**), where FFPQ-F and FFPQ-CC exhibit liner structures while FFPQ-C exhibits a coiled configuration. Additionally, all three polymers exhibit extensively delocalized HOMO/LUMO orbitals. More precisely, these orbitals are distributed over 5 out of 8 monomer units, similar to the orbital distribution over the TPTQ series of polymers.

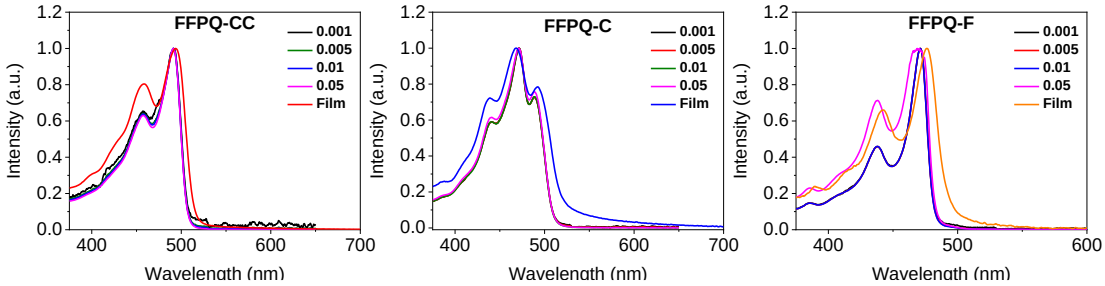

Figure 4.2: UV-Vis absorption spectra for FFPQ polymers

4.2.4 Optical Characterizations

We also performed concentration-dependent UV-Vis absorption measurements of our set of three polymers in solution-state and solid-state thin film. The spectra obtained following these measurements are shown in **Figure 4.2**. The solution absorption spectra for both FFPQ-C and FFPQ-CC exhibits an intense absorption over the range from 375 to 520 nm. FFPQ-C, however, has a slightly narrow absorption range from 375 to 490 nm. Their film absorption spectra exhibit a similar spectral shape, albeit red-shifted over a broader range of wavelengths than their corresponding solution spectra. However, the magnitude of this red-shift is different for each polymer, with FFPQ-C exhibiting the most red-shifted peaks followed by FFPQ-F and then FFPQ-CC.

The polymer FFPQ-CC exhibits an absorption spectrum that is almost independent of solution concentration. Here, the 0-0 transition peak is the most intense, followed by the 0-1 transition peak. Moreover, their intensity ratios do not change with decreasing concentration, indicating that H-aggregation exists even at a single polymer chain level. In thin-film, however, these intensities slightly vary, with the $I_A^{0\text{-}0}/I_A^{0\text{-}1}$ ratio decreasing slightly. None the less, 0-0 remains the most intense peak.

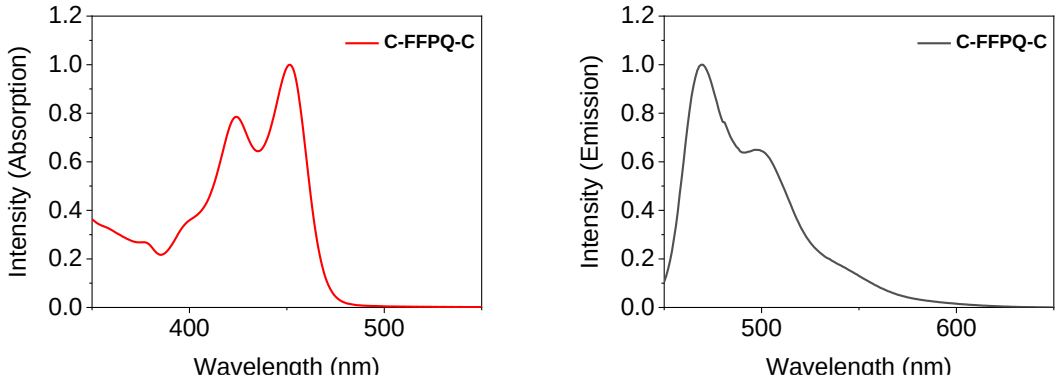

Figure 4.3: UV-Vis absorption and Emission spectra for FFPQ model compound

The polymer FFPQ-C exhibits slightly different spectral features. The 0-1 transition is the most intense absorption peak, followed by 0-0 and then 0-2 peaks. Its solution absorption spectrum remains independent of concentration until 0.01 mg/mL when 0-0 and 0-2 peaks slightly increase in intensity and becoming more intense in the thin-film spectrum. Again, this indicates that H-aggregation exists even at the level of a single polymeric chain and provides evidence for polymer folding. [16] Further evidence for this comes from the solution absorbance spectrum of the model compound (**Figure 4.3**), where the 0-0 transition peak is the most intense, followed by the 0-1 transition peak.

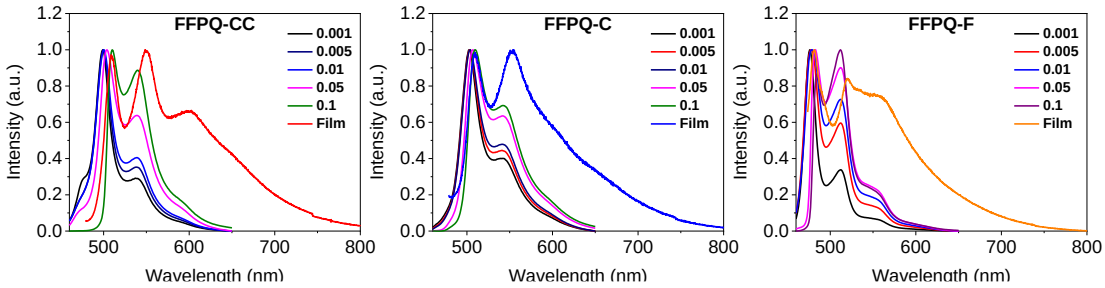

Figure 4.4: Emission spectra of FFPQ polymers

Polymer FFPQ-F, however, exhibits markedly different spectral features. Here 0-0 transition peak is the most intense, followed by the 0-1 transition peak. These peaks remain independent of concentration until 0.01 mg/mL when 0-1 peak increases in intensity as the polymer

concentration increases. Further increase in concentration reduces this intensity, as is evident in its thin-film spectrum. Nonetheless, 0-0 remains the most intense transition indicating J-aggregation.

The emission spectra (**Figure 4.4**) of our three polymers further strengthen our aggregation hypothesis. The spectra for FFPQ-C are red-shifted with increasing concentration and are further red-shifted in thin-film. The most dilute solutions' spectrum exhibits an intense 0-0 transition peak and a weak 0-1 transition peak. However, the I_A^{0-0}/I_A^{0-1} ratio decreases with increasing concentration as 0-1 becomes the most intense peak in thin-film. We observed the same three trends for FFPQ-CC emission spectra. However, the thin-film emission spectrum for FFPQ-CC exhibits one additional feature: Here, we can also observe a 0-2 transition peak absent in FFPQ-C and the solution spectra of FFPQ-CC. Nonetheless, all these trends indicate the formation of H-aggregates in both of these polymers. The emission spectrum of FFPQ-F, however, is remarkably different. Although it exhibits similar red-shifts and decreasing I_A^{0-0}/I_A^{0-1} ratio with increasing concentration, the 0-0 transition peak remains the most intense peak in thin films by far, indicating J-aggregate formation.

Table 4.2: Summary of I_A^{0-0}/I_A^{0-1} ratio for FFPQ polymers at different temperatures

T (°C)	FFPQ-CC	FFPQ-C	FFPQ-F
9	1.95	2.03	2.54
0	2.00	2.15	2.52
10	2.00	2.18	2.51

Table 4.2: Summary of I_A^{0-0}/I_A^{0-1} ratio for FFPQ polymers at different temperatures *(continued)*

20	2.02	2.18	2.46

Additionally, we performed temperature-dependent emission spectra of our polymers in THF and calculated the I_A^{0-0}/I_A^{0-1} ratios, the results of which are summarized in **Table 4.2**. It has been established that the I_A^{0-0}/I_A^{0-1} ratio will increase with increasing temperature for H-aggregates and decrease for J-aggregates. [17–19] Based on this and our concentration-dependent absorption and emission results, our carbazole polymers have H-aggregation while our fluorene polymer has J-aggregation. This was followed by carrying out time-resolved fluorescence decay measurements and calculating fluorescence lifetimes (**Table 4.3**). All of our polymers exhibit double exponential decay behavior indicating the presence of multiple relaxation pathways with fluorescence lifetimes ranging from 0.59 to 2.44 ns.

Table 4.3: Time-resolved fluorescence decay measurements for FFPQ polymers

Polymer	**τ1 (ns)**	**Fraction 1 (%)**	**τ2 (ns)**	**Fraction 2 (%)**
FFPQ-C	0.77	25	2.44	75
FFPQ-CC	0.84	57	1.8	43
FFPQ-F	0.59	91	1.35	9

4.2.5 GIWAX Results

Grazing incidence wide-angle X-ray scattering (GIWAXS) experiments were performed

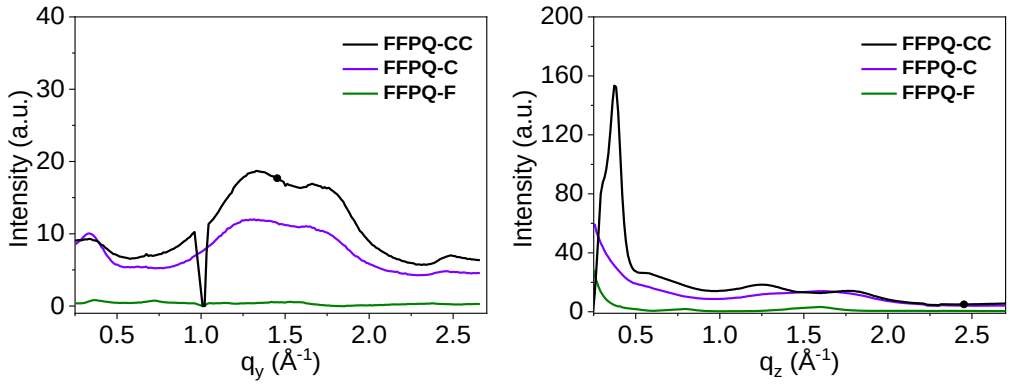

Figure 4.5: Linecuts of 2D GIWAX profiles for FFPQ polymers

to probe the solid-state structure on PEDOT:PSS coated silicon wafers. The 2D scattering profiles and linecuts along in-plane and out-of-plane directions are shown in **Figure 4.5**. We found that all three of our polymers were relatively amorphous, with a slight preference for face-on packing. Of the three polymers, FFPQ-CC was the most crystalline, with sharp peaks along both y and z axes. Not surprisingly, FFPQ-CC exhibited the shortest pi-pi stacking distance of 3.57 Å among all three polymers. The other two polymers failed to exhibit any distinguishable peaks in their 2D GIWAX profiles. The longer pi-pi stacking distances of the other two polymers confirm this observation as they exhibited distances of 3.89 Å and 3.95 Å for polymers FFPQ-C and FFPQ-F, respectively.

4.3 Device Fabrication

4.3.1 OFET Fabrication

Table 4.4: Charge carrier mobility values for FFPQ polymers

Material	**μ_h ($cm^2V^{-1}s^{-1}$)**	**μ_e ($cm^2V^{-1}s^{-1}$)**
FFPQ-CC[a]	1.58×10^{-5}	-

Table 4.4: Charge carrier mobility values for FFPQ polymers *(continued)*

FFPQ-C[a]	5.2×10^{-6}	-
FFPQ-F[a]	-	-
FFPQ-CC[b]	4.7×10^{-2}	6.4×10^{-2}
FFPQ-C[b]	3.2×10^{-1}	7.8×10^{-1}
FFPQ-F[b]	3.2×10^{-4}	6.3×10^{-4}

a Mobility calculated from OTS modified OFET devices; b Mobility calculated from OTS modified OLET devices

We firstly fabricated single-layered bottom-gate top-contact OFET devices and measured their mobilities. These values are summarized in **Table 4.4**. It is evident that none of the polymers exhibited any measure of ambipolarity in single-layered OFET devices. Additionally, fluorene-

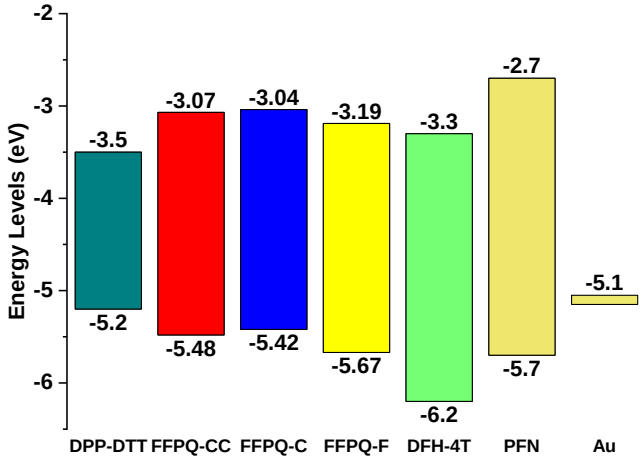

Figure 4.6: Energy Level diagram for FFPQ polymers

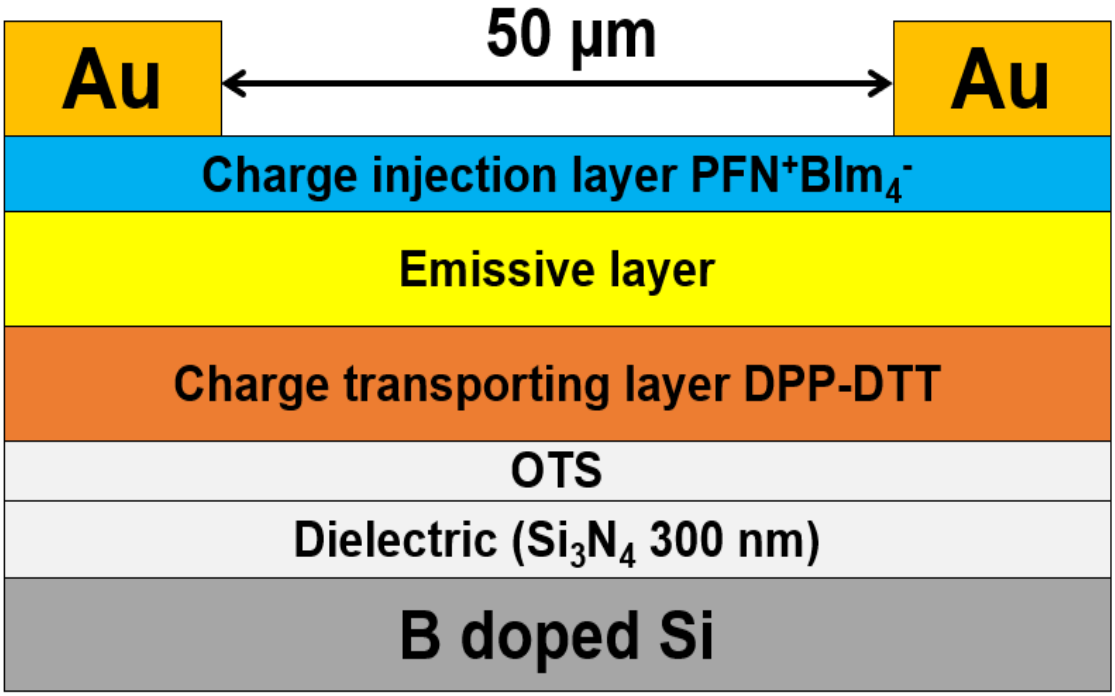

Figure 4.7: OLET Device architecture for FFPQ polymers

based polymer FFPQ-F failed to demonstrate any field-effect mobility at all. However, its carbazole based counterparts FFPQ-CC and FFPQ-C did exhibit minimal hole mobility. This could be a direct consequence of two factors. First, none of the polymers exhibited any degree of crystallinity in their 2D GIWAX profiles. Additionally, as is evident in **Figure 4.6**, the energetic barrier for hole injection from gold is much lower than the electron injection barrier. Therefore we only see p-type behavior and no emission in our single-layered polymer systems.

4.3.2 OLET Fabrication

As demonstrated in the previous chapters, it was necessary to employ a multi-layered device architecture. The overall device architecture in **Figure 4.7** was as follows: Si/Si_3N_4/OTS/DPP-DTT/Emissive layer/PFN^+BIm4^-/Au. The results of the measurements in the form of output and transfer curves, respectively, are shown in **Figure 4.8**. All three of our devices

exhibited V-shaped transfer curves indicating ambipolar charge transport at the interface of dielectric and charge transport layers. More importantly, as shown in **Table 4.4,** our multi-layered OLET hole/electron mobilities are several orders of magnitude higher than the hole/electron mobilities of our single layered OFET devices. This would be a critical factor in our device performance.

A cursory examination of our polymers' electroluminescence spectra showed a striking resemblance to its corresponding solid-state thin-film photoluminescence spectrum. We then

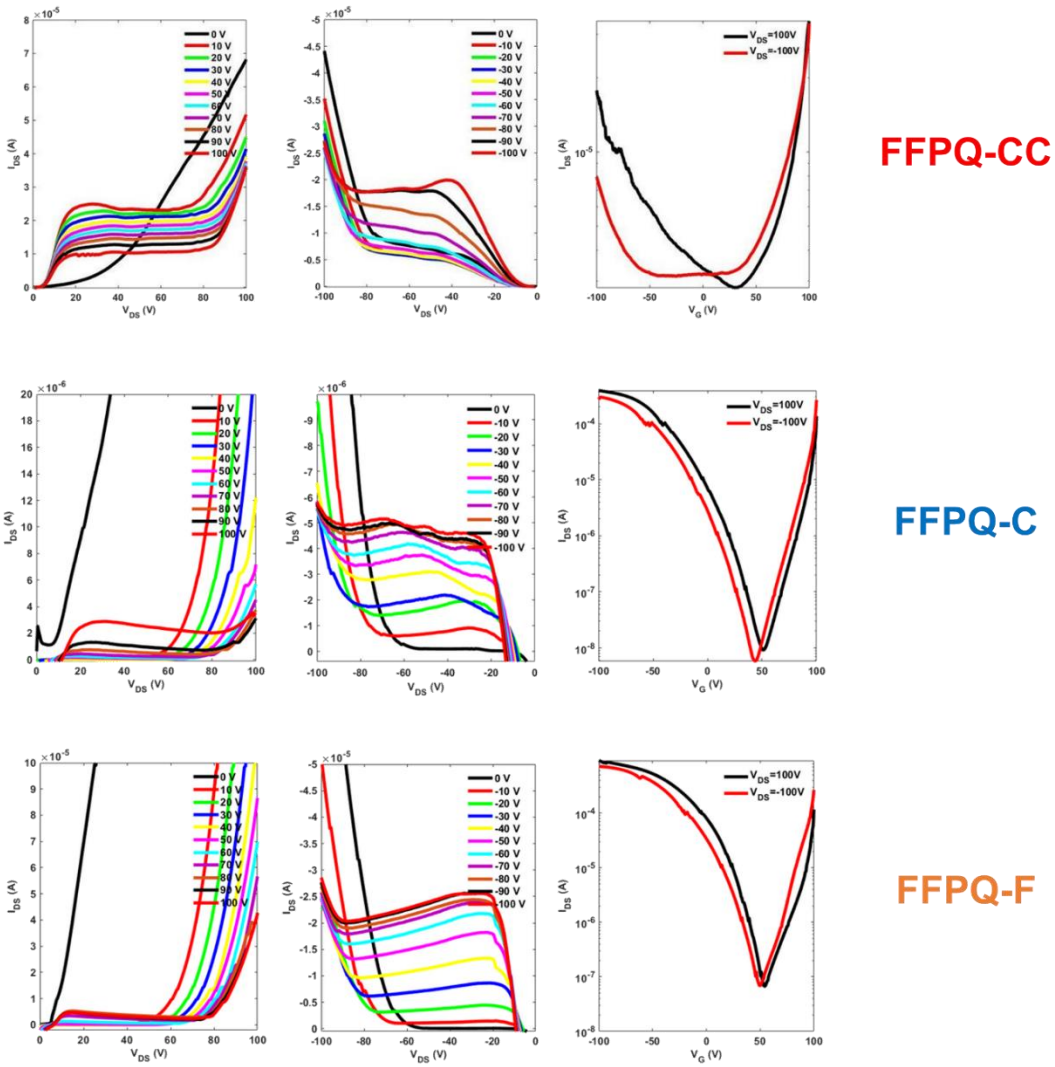

Figure 4.8: Transfer and output curves for FFPQ polymers

moved on to measure the source-drain input current of our OLET devices in concert with the output photocurrent emanating from a reverse-biased photodiode. Based on this, we calculated the luminescence intensity as well as the EQE of our devices. All three of our polymers exhibited bright green (**Figure 4.9**) emission, which was most intense in response to the negative gate voltages where holes are the majority carriers.

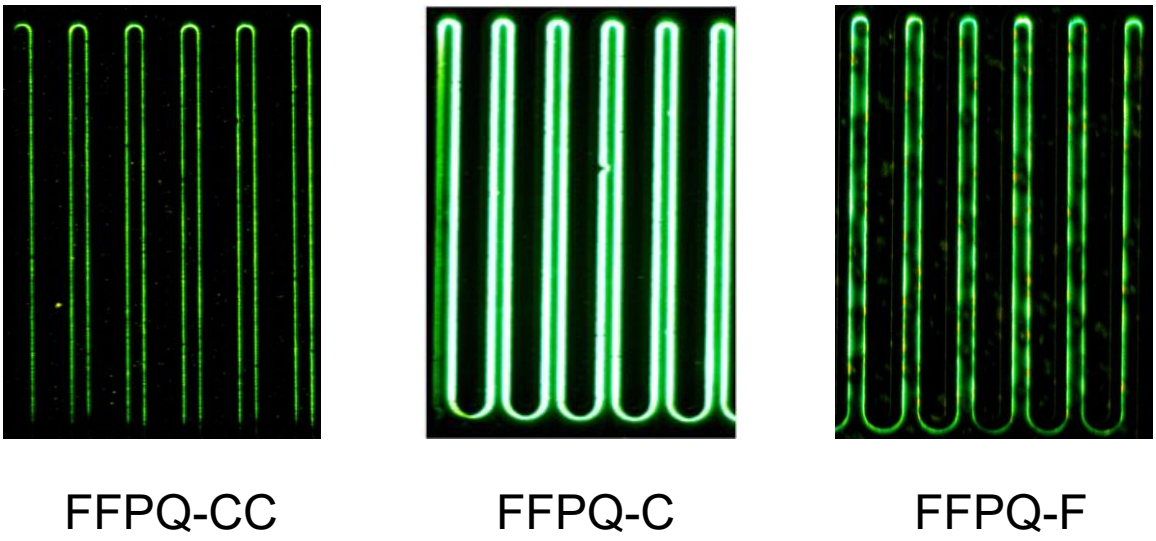

Figure 4.9: Electroluminescence for FFPQ polymers

Among these three, the device corresponding to the polymer FFPQ-C was the brightest and exhibited a luminescence intensity of 216 nW. Additionally, we measured the EQE of our devices along gate voltages exhibiting the brightest emission and found that the device corresponding to polymer FFPQ-C exhibited an EQE of 3.5% (**Figure 4.10**). This was more than three orders of

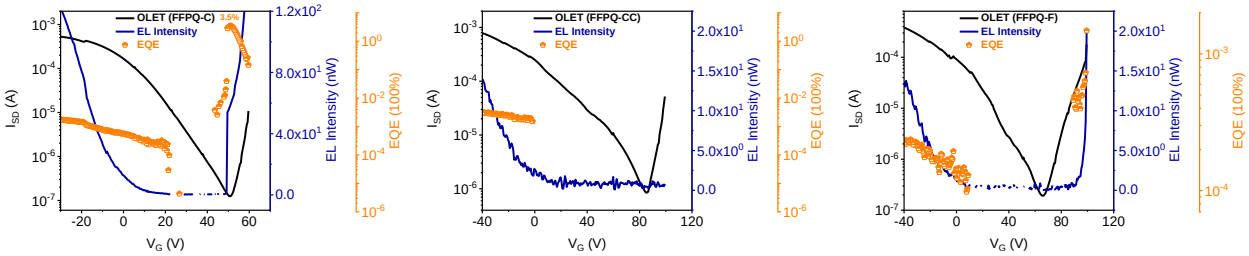

Figure 4.10: EQE and EL intensity for FFPQ polymers

magnitude higher than the EQE of the corresponding tri-layered OLED devices. Unfortunately, the rest of the OLET devices exhibited an EQE of around 10^{-3}%.

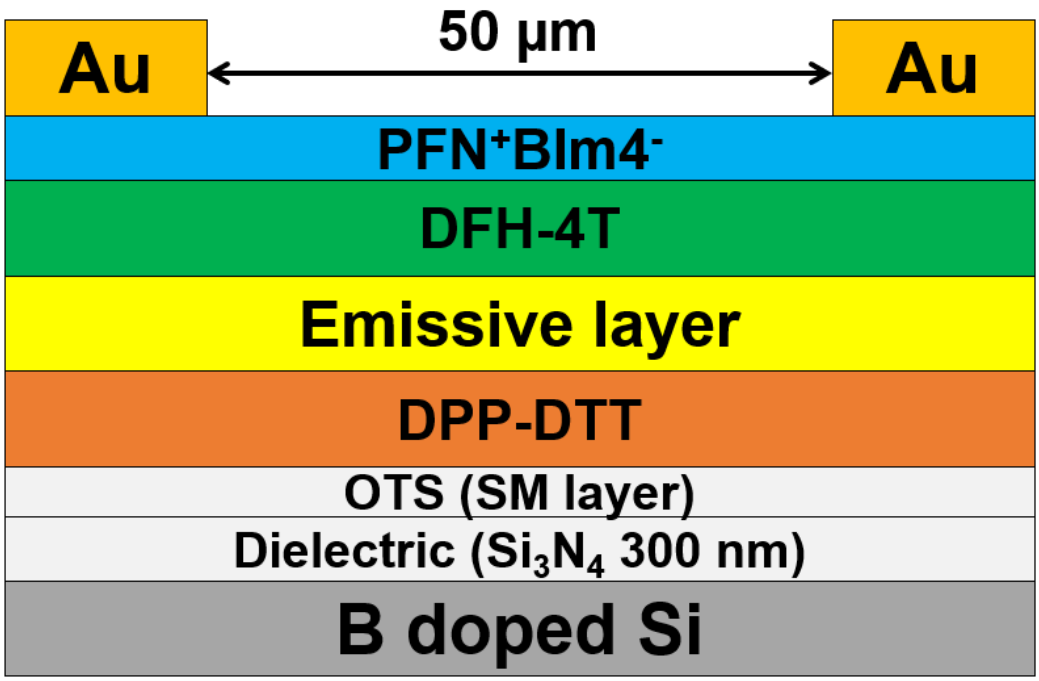

Figure 4.11: Optimized OLET Device architecture for FFPQ polymers

4.3.3 OLET Optimization

Since the FFPQ-C system showed the most promising results, we focused further optimization efforts on this polymer. As is evident in **Figure 4.9**, the $PFN^{+}BIm_4^{-}$ layer failed in the transport of electrons, as a result of which the charge carriers in the DPP-DTT layer were forced to combine near the drain electrode. This narrowed the emission zone near the drain electrode, led to exciton quenching on gold, and by extension, a low EQE. To address this issue, we inserted another charge (electron) transporting layer 5,5‴-Bis(tridecafluorohexyl)-2,2′:5′,2″:5″,2‴-quaterthiophene (DFH-4T) between the electron injection layer and the emissive layer (**Figure 4.11**). Crucially, this layer exhibited high electron mobility of 0.5 $cm^2V^{-1}s^{-1}$, and its energy levels aligned well with those of FFPQ-C. Significantly, although its HOMO (-6.3 eV) was

much lower than the HOMO of the emissive layer, its LUMO (-3.3 eV) aligned well with that of FFPQ-C. Thus, the emission zone in our new devices (**Figure 4.12**) extended over the entire length of the device, which was in sharp contrast with the emission zone in our previous device. More importantly, the device parameters corresponding to the new architecture were substantially improved. Not only did we obtain an impressive EQE of 6.9%, but we also obtained an EL intensity of 2332 nW, which are among the highest values reported to date.

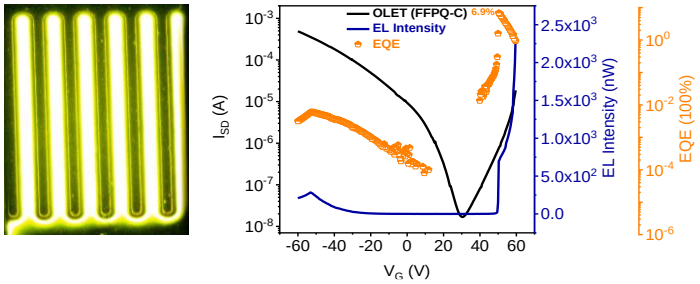

Figure 4.12: EQE and EL intensity for FFPQ-C

Interestingly, the most promising EQE was observed for the polymer with the lowest photoluminescence in solution. Clearly, improving just photoluminescence without a corresponding improvement in charge transport characteristics is not the correct approach. In this case, we were able to substantially enhance charge transport characteristics with the aid of the additional DFH-4T layer, which improved the EQE and enhanced the light emission distribution. This ensured that the charge carriers could combine in the middle of the channel and avoid quenching via the gold electrodes.

4.4 Conclusion

In this chapter, we sought to address the critical research problem facing researchers in the field of organic light-emitting transistors that is achieving simultaneous photoluminescence and charge carrier mobility in a single system, which would then lead to electroluminescence. Here,

we fused together the lessons learned in the previous chapters towards achieving high-performance devices. For instance, in Chapter 2, we validated that the multi-layered device structure used in concert with semi-ladder polymer systems did indeed exhibit substantial promise. These two strategies would be a recurring theme throughout this thesis. Next, in Chapter 3, we confirmed that the TPTQ series of polymers, especially the one with a coiled foldamer-like structure, allows us to access high mobility without compromising on emission performance.

In this chapter, we sought to blend the advantages offered by folded semi-ladder polymers in a multi-layered OLET device and then eliminated the emission quenching due to the internal heavy atom effect. More importantly, it was the first time that anyone specifically reduced the heavy atom effect in the context of light-emitting transistors. It was thus a combination of all the favorable factors described above that led to an EQE of 6.9% and an EL intensity of 2332 nW. These are among the highest values reported in the literature.

4.5 Materials and Methods

See Chapter 2

4.5.1 Synthesis

Compound 7: See Chapter 2

Compound 8: See Chapter 2

Compound 11: A solution of Compound 10 (4 eq) was dissolved in thionyl chloride (20 mL) and refluxed overnight. Afterward, the solvent was removed under reduced pressure to yield an acyl chloride as a white solid. It was then dissolved in DMA (20 mL) and added dropwise to a suspension of Compound 8 (1 eq), NaH (4 eq), and DMA (30 mL) at 0 °C. The reaction mixture was stirred at 100 °C overnight. The reaction mixture was then poured into water and extracted with DCM. The organic layer was washed with water, dried over $MgSO_4$, and the solvent was removed under reduced pressure. The crude mixture was then purified by silica gel chromatography eluted with hexane:ethyl acetate (9:1) to afford Compound 9 in a 94 % yield. ^{1}H-NMR (500 MHz, CDCl3): δ (ppm) 7.57 (d, 4H), 7.29 (s, 2H), 7.19 (d, 2H), 6.2 (s, 2H), 4.15 (d, 2H), 3.34 (dd, 2H), 1.33 (m 34H), 0.88 (m, 12H). ^{13}C-NMR (100 MHz, CDCl3): δ (ppm) 163.51, 163.09, 144.94, 142.90, 142.60, 142.46, 136.03, 135.91, 135.85, 123.32, 121.93, 121.82, 110.55, 110.53, 52.76, 36.77, 36.66, 36.49, 36.45, 31.89, 31.82, 31.80, 31.76, 31.71, 31.50, 31.36, 31.13, 29.69, 28.81, 28.61, 28.51, 28.49, 26.59, 26.41, 26.31, 26.29, 23.04, 23.02, 22.99, 22.67, 22.65. MS (MALDI-TOF) *m*/*z* 790.89 (M+), calcd 790.72.

FFPQ: Compound 11 (1 eq), $Pd(PPh_3)_4$ (0.05 eq), and AcOK (3 eq) was dissolved in DMA (150 mL). The mixture was degassed for 30 min and then refluxed for 4 h. The reaction mixture was

then poured into water and extracted with DCM. The organic layer was washed with water, dried over $MgSO_4$, and the solvent was removed under reduced pressure. The crude mixture was then purified by silica gel chromatography eluted with hexane:ethyl acetate (9:1) to afford FFPQ as a yellow solid in an 83% yield. ^{1}H-NMR (500 MHz, CDCl3): δ (ppm) 8.04 (s, 2H), 7.69 (d, 2H), 7.14 (d, 2H), 4.44 (br, 4H), 20.8 (m, 2H), 1.44 (m, 32H), 0.88 (m, 12H). ^{13}C-NMR (100 MHz, CDCl3): δ (ppm) 159.45, 154.21, 144.64, 132.73, 116.57, 114.37, 109.15, 107.22, 46.15, 36.63, 31.87, 31.74, 31.46, 29.70, 29.01, 26.79, 23.11, 22.61, 14.13. MS (MALDI-TOF) *m*/*z* 629.1 (M+), calcd 628.90.

Br-FFPQ-Br: FFPQ (1 eq) was dissolved in DMF, and the solution cooled to 0 °C in the dark. NBS (2.2 eq) in DMF was then added dropwise, after which the solution was warmed to room temperature and stirred overnight. The reaction mixture was poured into water and extracted with chloroform. The organic layer was dried with $MgSO_4$, and the solvent was removed under reduced pressure. The crude mixture was recrystallized from dichloromethane/methanol to give a yellow solid in 70 % yield. ^{1}H-NMR (500 MHz, CDCl3): δ (ppm) 7.96 (s, 2H), 7.05 (s, 2H), 4.41 (br, 4H), 2.02 (m, 2H), 1.25-1.46 (m, 32H), 0.84-0.93 (m, 12H). ^{13}C-NMR (100 MHz, CDCl3): δ (ppm) 158.17, 154.76, 132.62, 126.77, 118.58, 113.76, 110.86, 107.22, 45.95, 36.79, 31.84, 31.52, 29.71, 29.12, 26.87, 23.11, 22.64, 14.19. MS (MALDI-TOF) *m*/*z* 786.75 (M+), calcd 786.69.

C-FFPQ-C: Br-FFPQ-Br (1 eq), Carbazole-BPin (3 eq), K_2CO_3 (4 eq), Aliquat 336 (3 drops), and $Pd(PPh_3)_4$ (0.05 eq) were dissolved in 6ml of Toluene/H_2O (10:1). The mixture was degassed for 30 minutes and refluxed overnight. After cooling to room temperature, the mixture was poured into water and extracted with DCM. The organic layer was dried with $MgSO_4$, and the solvent was removed under reduced pressure. The crude mixture was purified by column chromatography on silica gel hexane:ethyl acetate (9:1) mixture to get yellow-green solid in 43% yield. ^{1}H-NMR (500

MHz, CDCl3): δ (ppm) 8.53 (s, 2H), 8.16 (d, 2H). 8.09 (s, 2H), 7.94 (d, 2H), 7.51 (t, 2H), 7.42 (t, 4H), 7.33 (s, 2H), 7.30 (t, 2H), 4.56 (br, 4H), 4.15 (d, 4H), 2.01 (m 4H), 1.01-1.71 (m, 64 H), 0.88 (m, 24H). MS (MALDI-TOF) *m*/*z* 1295.89 (M+), calcd 1295.94.

General Procedure for Semi-Ladder Copolymers: A mixture of Br-FFPQ-Br monomer (1 eq) and Carbazole/Fluorene comonomer (1 eq), K_2CO_3 (4 eq), Aliquat 336 (3 drops), and $Pd(PPh_3)_4$ (0.05 eq) were dissolved in 4ml of Toluene/H_2O (10:1). The mixture was degassed for 30 minutes and then refluxed for 72 hours. After cooling to room temperature, the mixture was passed through Celite and precipitated in methanol. The polymer fibers were then washed by Soxhlet extraction with methanol, acetone, hexanes, and chloroform. The final polymer was obtained after reprecipitation of chloroform fraction in methanol.

FFPQ-C: Yield: 99 %. ^{1}H-NMR (500 MHz, CDCl3): δ (ppm) 6.51-8.62 (m, 10H), 3.60-5.51 (m, 6H), 0.51-2.35 (m 61H).

FFPQ-CC: Yield: 52 %. ^{1}H-NMR (500 MHz, CDCl3): δ (ppm) 6.40-8.35 (br, 10H), 3.30-5.35 (m, 6H), 0.42-2.35 (m 61H).

FFPQ-F: Yield: 84 %. δ (ppm) 8.18 (s, 2H), 7.96 (s, 2H), 7.88 (s, 4H), 7.45 (s, 2H), 4.59 (br, 4H), 2.26 (br, 6H), 1.20-1.75 (m, 32H), 0.40-1.05 (m, 42H).

4.5.2 Optical analysis

See Chapter 2

4.5.3 X-ray analysis

See Chapter 2

4.5.4 Device Fabrication

For the optimized OLET device, a hot chloroform solution of DFH-4T with a concentration of 2 mg mL^{-1} was spin-coated onto a fast rotating emissive layer at 4000 rpm/60 seconds and then transferred to a vacuum oven to remove the solvent. Then $PFN^{+}BIm4^{-}$ was dissolved in methanol with a concentration of 2 mg mL^{-1}. After filtration, the $PFN^{+}BIm4^{-}$ layer was spin-coated onto the active layer at 7000 rpm for 30 seconds yielding a thickness of less than 10 nm. Polymer films were then annealed at 60°C for 20 min in air and then transferred back to the glove box for thermal deposition of source-drain electrodes. 30 nm of gold was deposited in a vacuum chamber under $<10^{-6}$ Torr pressure through a shadow mask purchased from Ossila Ltd.

For OLED device fabrication, see Chapter 2

4.5.5 Device Measurements

See Chapter 2

4.6 References

(1) Worsfold, P.; Townshend, A.; Poole, C.; Miró, M. *Encyclopedia of Analytical Science*; 2019.

(2) Cai, Z.; Zhang, N.; Awais, M. A.; Filatov, A. S.; Yu, L. Synthesis of Alternating Donor-Acceptor Ladder-Type Molecules and Investigation of Their Multiple Charge-Transfer Pathways. *Angew. Chemie* **2018**.

(3) Perrin, F. Polarization of Light of Fluorescence, Average Life of Molecules. *J. Phys. Radium* **1926**.

(4) Mcclure, D. S. Triplet-Singlet Transitions in Organic Molecules. Lifetime Measurements of the Triplet State. *J. Chem. Phys.* **1949**.

(5) Nairn, J. A.; Braun, C. L.; Caluwe, P.; Szwarc, M. Fluorescence Quenching as a Tool for Studies of Rates of Intramolecular Encounters. *Chem. Phys. Lett.* **1978**.

(6) Al Anshori, J.; Slanina, T.; Palao, E.; Klán, P. The Internal Heavy-Atom Effect on 3-Phenylselanyl and 3-Phenyltellanyl BODIPY Derivatives Studied by Transient Absorption Spectroscopy. *Photochem. Photobiol. Sci.* **2016**.

(7) Berberan-Santos, M. N. External Heavy-Atom Effect on Fluorescence Kinetics. *PhysChemComm* **2000**.

(8) Yuan, D.; Awais, M. A.; Sharapov, V.; Liu, X.; Neshchadin, A.; Chen, W.; Bera, M.; Yu, L. Foldable Semi-Ladder Polymers: Novel Aggregation Behavior and High-Performance Solution-Processed Organic Light-Emitting Transistors. *Chem. Sci.* **2020**.

(9) Yuan, D.; Awais, M. A.; Sharapov, V.; Liu, X.; Neshchadin, A.; Chen, W.; Yu, L. Highly Emissive Semi-Ladder-Type Copolymers, Aggregation State, and Solution-Processed Organic Light-Emitting Transistor. *Chem. Mater.* **2020**.

(10) Jung, I. H.; Zhao, D.; Jang, J.; Chen, W.; Landry, E. S.; Lu, L.; Talapin, D. V.; Yu, L. Development and Structure/Property Relationship of New Electron Accepting Polymers Based on Thieno[2′,3′:4,5]Pyrido[2,3-g]Thieno[3,2-c]Quinoline-4,10-Dione for All-Polymer Solar Cells. *Chem. Mater.* **2015**, *27* (17), 5941–5948.

(11) Jung, I. H.; Lo, W.; Jang, J.; Chen, W.; Landry, E. S.; Lu, L.; Talapin, D. V; Yu, L.; Zhao, D. Synthesis and Search for Design Principles of New Electron Accepting Polymers for All-Polymer Solar Cells Synthesis and Search for Design Principles of New Electron Accepting Polymers for All-Polymer Solar Cells. **2014**.

(12) Adegoke, O. O.; Jung, I. H.; Orr, M.; Yu, L.; Goodson, T. Effect of Acceptor Strength on Optical and Electronic Properties in Conjugated Polymers for Solar Applications. *J. Am. Chem. Soc.* **2015**.

(13) Usluer, O.; Demic, S.; Egbe, D. A. M.; Birckner, E.; Tozlu, C.; Pivrikas, A.; Ramil, A. M.; Sariciftci, N. S. Fluorene-Carbazole Dendrimers: Synthesis, Thermal, Photophysical and Electroluminescent Device Properties. *Adv. Funct. Mater.* **2010**.

(14) Wu, Y.; Wu, D.; Zhao, H.; Li, J.; Li, X.; Wang, Z.; Wang, H.; Zhu, F.; Xu, B. Synthesis and Properties of Hyperbranched Polymers for Polymer Light Emitting Devices with Sunlight-Style White Emission. *RSC Adv.* **2019**.

(15) Wang, Z.; Wang, C.; Gan, Q.; Cao, Y.; Yuan, H.; Hua, D. Donor-Acceptor-Type Conjugated Polymer-Based Multicolored Drug Carriers with Tunable Aggregation-Induced Emission Behavior for Self-Illuminating Cancer Therapy. *ACS Appl. Mater. Interfaces* **2019**.

(16) Fauvell, T. J.; Zheng, T.; Jackson, N. E.; Ratner, M. A.; Yu, L.; Chen, L. X. Photophysical and Morphological Implications of Single-Strand Conjugated Polymer Folding in Solution. *Chem. Mater.* **2016**.

(17) Spano, F. C. The Spectral Signatures of Frenkel Polarons in H- And J-Aggregates. *Acc. Chem. Res.* **2010**.

(18) Spano, F. C.; Silva, C. H- and J-Aggregate Behavior in Polymeric Semiconductors. *Annu. Rev. Phys. Chem.* **2014**.

(19) Zheng, C.; Zhong, C.; Collison, C. J.; Spano, F. C. Non-Kasha Behavior in Quadrupolar Dye Aggregates: The Red-Shifted H-Aggregate. *J. Phys. Chem. C* **2019**.

Chapter 5

Developing Benzotriazole Based Semi-Ladder Polymer Systems for use in Multi-Layered OLET Devices

5.1 Background

The previous three chapters investigated the photophysical properties of polymers based on either TPTQ or its positional isomer TPTI. [4,5] These polymers exhibit light emission in green and yellow colors. It is known that three primary colors: red, green, and blue, are needed to make a broad spectrum of colors required for a full-color display. However, the limited conjugation length of the chromophore TPTQ and TPTI makes any further color change difficult.

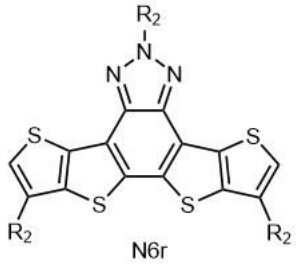

N6r

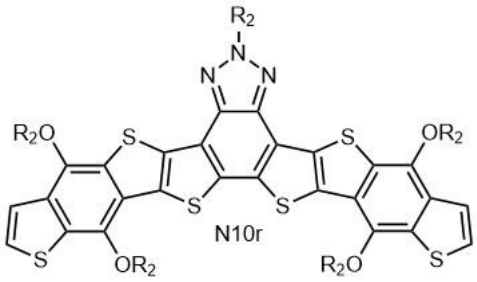

N10r

Figure 5.1: Chemical structure of N6r and N10r

None the less, the themes illustrated in those chapters were general and could be applied to a broad series of compounds. For this reason, we chose to develop benzotriazole based ladder-type compounds N6r and N10r (**Figure 5.1**), which were structurally distinct from the TPTQ/TPTI/FFPQ series of monomers used in the previous chapters and exhibit more flexibility in changing the conjugation length of the chromophore. These compounds also offered other advantages. For instance, the N10r monomer had a 69.7% PLQY in chloroform solution and exhibited a single molecular conductance value of 1.7 $\times 10^{-4}$ G_0, indicating the potential for exhibiting decent semiconductivity in the resulting polymers. [6] For this reason, we synthesized electron-accepting dibrominated N6r and N10r comonomers and copolymerized them with carbazole to form several polymers. We then investigated their structure-property relationship.

5.2 Results and Discussion

5.2.1 Synthesis

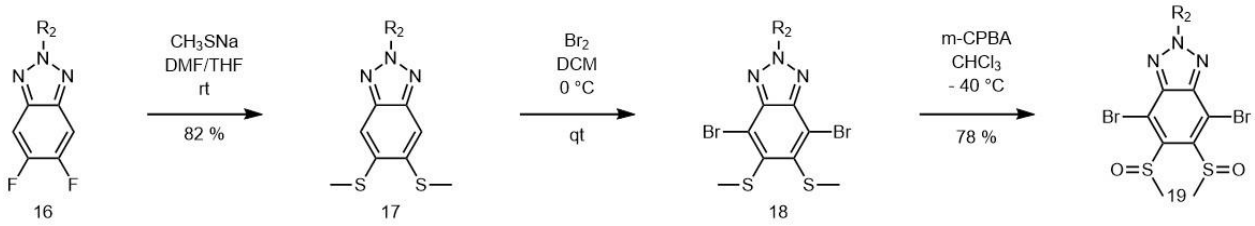

Scheme 5.1: Synthesis of Benzotriazole monomer

The di-brominated N6r and N10r were synthesized according to **Scheme 5.1** from alkylated and difluorinated benzotriazole (Compound 16). [6] Compound 16 was then subjected to a nucleophilic aromatic substitution with sodium thiomethoxide ($NaSCH_3$) in dimethylformamide/tetrahydrofuran (DMF/THF) mixture to yield Compound 17. This was brominated to yield dibrominated benzotriazole (Compound 18), which was then oxidized to Compound 19 using meta chloroperoxybenzoic acid (m-CPBA) at -40 °C. Compound 19 was

treated to a mono borylated thiophene (Compound 20) in a 1:2 ratio via Suzuki coupling condensation reaction to yield the intermediate Compound 21 (**Scheme 5.2**). This compound then underwent electrophilic aromatic substitution cyclization reaction via the aid of sulfinyl groups on the central benzotriazole moiety to yield a methyl sulfonium salt intermediate, which was then treated with pyridine to yield N6r. The N6r was then treated with N-Bromosuccinimide (NBS) to give the final monomer Br-N6r-Br. Synthesis of Br-N10r-Br also started from Compound 19, which was treated with Tips protected and mono styannylated benzodithiophene (Compound 22) in a 1:2 ratio via Stille coupling condensation reaction to yield Compound 23. Compound 23 was converted to Br-N10r-Br via ring-closing and bromination reactions, which were virtually identical to those used to synthesize Br-N6r-Br discussed previously.

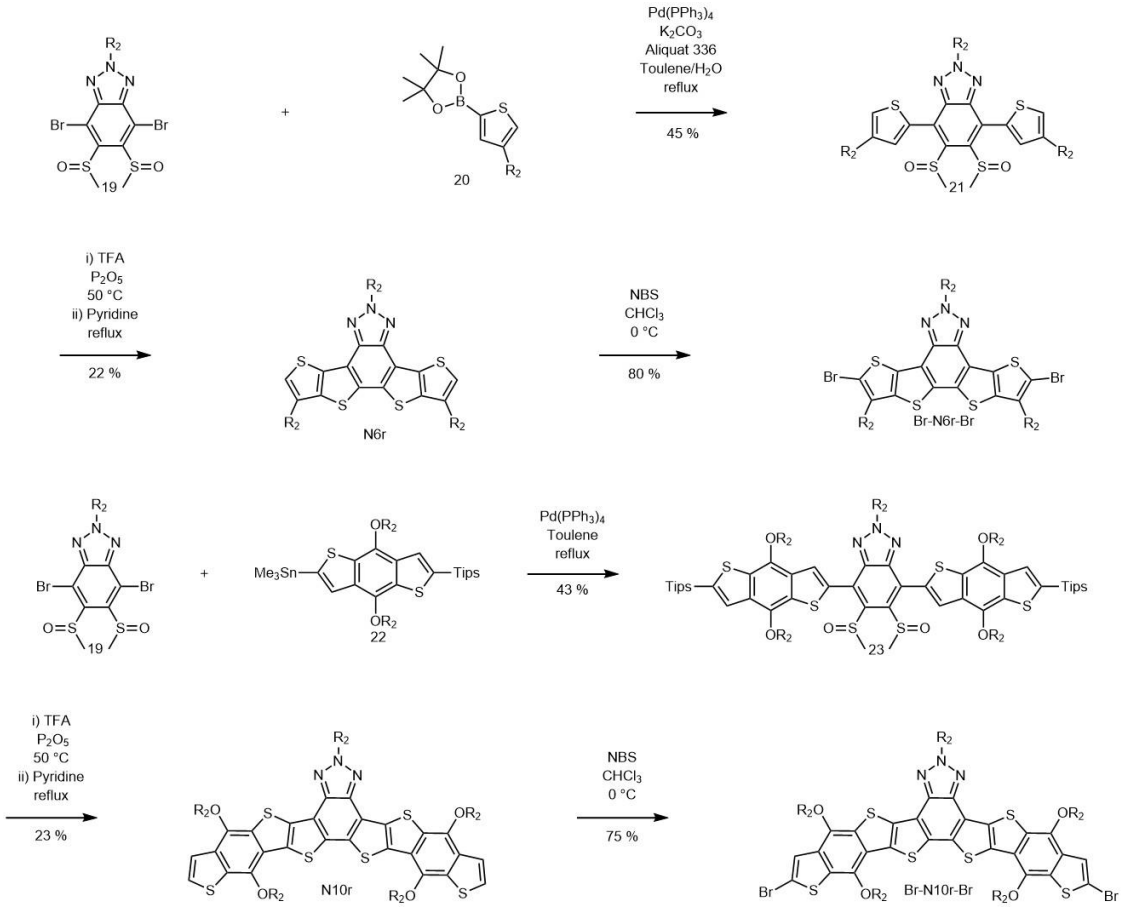

Scheme 5.2: Synthesis of Br-N6r-Br and Br-N10r-Br

The syntheses of both our carbazoles-based comonomers are described in **Schemes 2.3** and **3.1** and will not be repeated here. [7–9] Similarly, we employed the Suzuki coupling condensation reaction of electron-withdrawing dibrominated N6r and N10r with electron-donating carbazoles (**Scheme 5.3**) to synthesize our polymers. As in the previous chapters, polymers N6r-C and N10r-C are cross conjugated, while polymers N6r-CC and N10r-CC are fully conjugated.

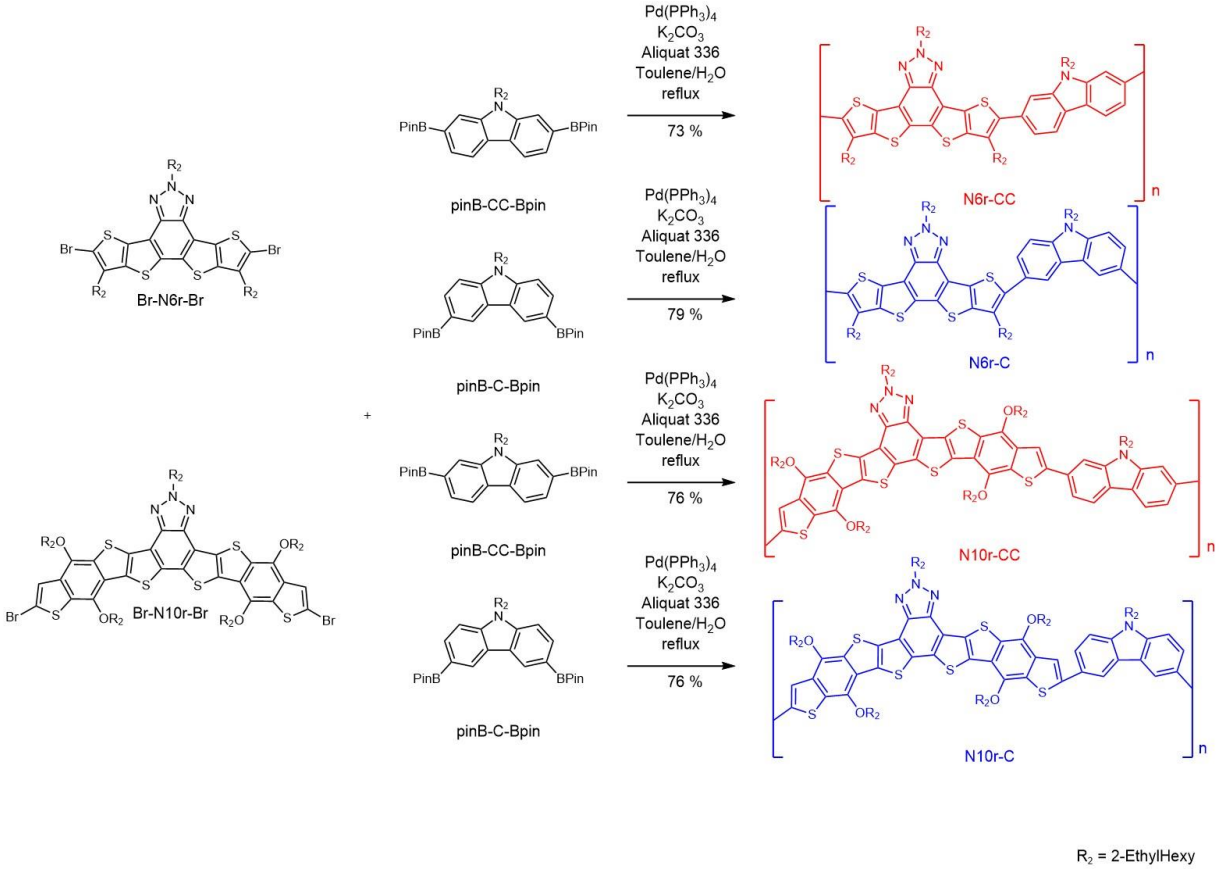

Scheme 5.3: Synthesis of Benzotriazole polymers

5.2.2 Basic Characterizations

As compared to the polymers in the three previous chapters, all of our polymers here had very low molecular weights (**Table 5.1**), which correspond to less than ten repeating units. While only one reaction was carried out for each of the polymers, this was likely an issue of low reactivity of the starting benzotriazole based monomers. Additionally, while the polymers were soluble in

chloroform, they failed to exhibit decent solubility in toluene or xylene, which would be consequential in the device fabrication process later.

Table 5.1: Physical and Optoelectronic properties of Benzotriazole polymers

Polymer	HOMO (eV)	LUMO (eV)	Bandgap E_g (eV)	PLQY (%)	Mw	Mn	PDI
6Nr-C	-5.34[a]/-4.76[b]	-2.68[d]/-1.62[b]	3.14[b]/2.66[c]	63.2	7153	7997	1.12
6Nr-CC	-5.41[a]/-4.87[b]	-2.89[d]/-1.87[b]	3.00b/2.52[c]	80.6	4652	5516	1.18
10Nr-C	-5.12[a]/-4.07[b]	-2.87[d]/-2.35[b]	1.72[b]/2.25[c]	24.6	5284	7406	1.40
10Nr-CC	-5.08[a]/-4.85[b]	-2.79[d]/-2.13[b]	2.72[b]/2.29[c]	20.5	9535	10670	1.12

[a] Measured from the cyclic voltammetry, [b] Bandgap E_g calculated from DFT, [c] Bandgap E_g calculated from the onset of the film absorption, [d] LUMO energy levels are calculated as HOMO of the polymer from CV + E_g from the onset of film absorption

PLQY measurements were carried out in chloroform solution using Rhodamine B as a standard. Of these four polymers, N6r-CC exhibited the highest quantum yield of 80.6%, followed by 63.2% for N6r-C (**Table 5.1**). These quantum yields match with the best polymers synthesized in the previous chapters. However, the polymers corresponding to the more extended ladder compound exhibited lower quantum yields of around 20%.

We performed cyclic voltammetry experiments on all four of our polymers to deduce the HOMO energy levels (**Figure 5.2**). Towards these ends, the polymer solution was coated onto the

working electrode, and the current was measured as the voltage was incrementally increased from 0 to 1.5 V, and then back to 0 V. All four polymers exhibited oxidation peaks in their cyclic voltagrams. However, these peaks were only quasi reversible as the ratio between the areas under the oxidation peak and the back peak was less than unity. This is normal among organic conjugated polymers. The HOMO energy levels were then calculated in reference to ferrocene according to the following formula: $E_{HOMO} = -(E_{ONSET} + 4.8 - E_{Fc})eV$. Similarly, we tried to calculate the LUMO energy levels by employing a reverse voltage sweep at negative voltages. Unfortunately, the voltage range employed failed to elicit a significant current response, and for this reason, we employed another method to calculate the LUMO energy levels (**Table 5.1**).

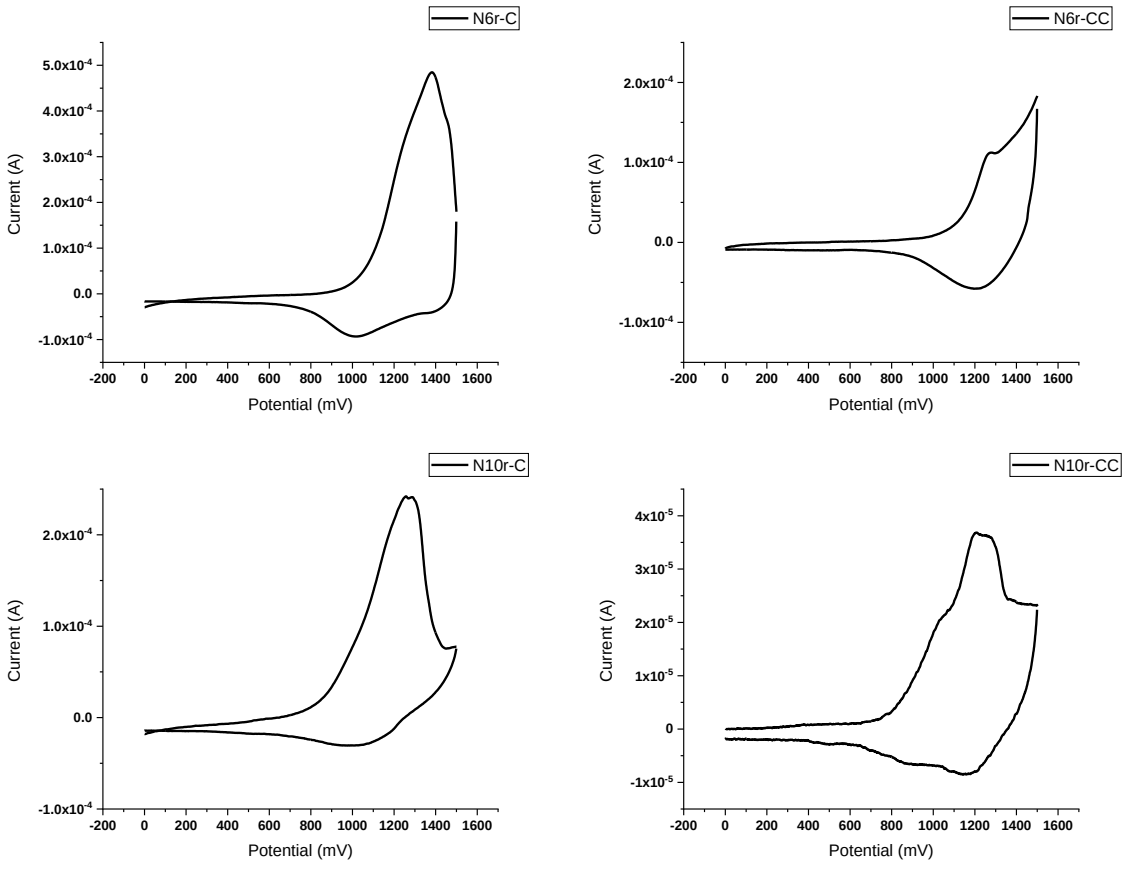

Figure 5.2: CV spectra for Benzotriazole polymers

The LUMO energy levels and bandgaps were also calculated (**Table 5.1**). As expected, polymers corresponding to the 10-ringed repeating unit had narrower bandgaps than those corresponding to the 6-ringed repeating unit. This difference of approximately 0.25 eV was anticipated as a consequence of a more extended conjugation length of N10r. The LUMO energy levels of all four polymers were roughly the same. The bandgap difference resulted from a difference in HOMO energy levels where polymers corresponding to N6r monomer had deeper HOMOs.

5.2.3 Thermal Characterizations

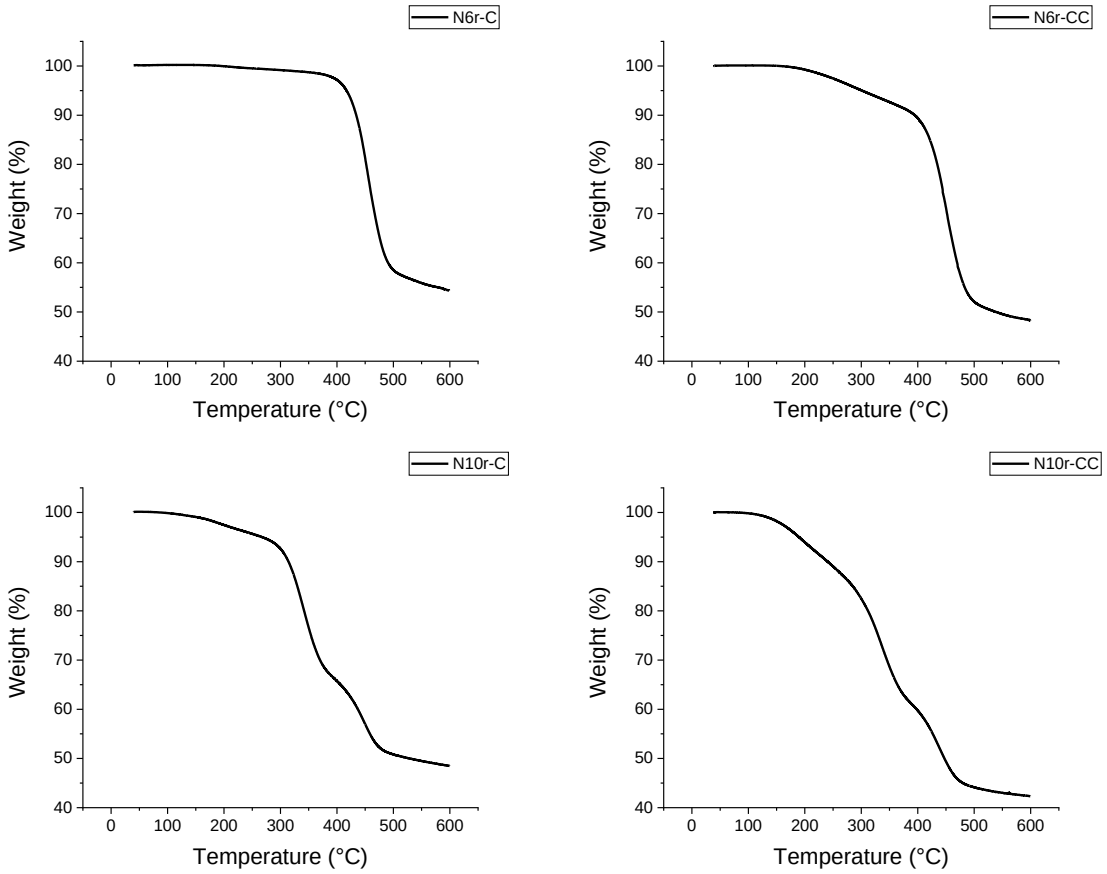

Figure 5.3: TGA spectra for Benzotriazole polymers

We carried out thermogravimetric analysis (TGA) (**Figure 5.3**) and differential scanning calorimetry (DSC) (**Figure 5.4**) to understand the stability and thermal properties of our polymers.

As seen in the TGA spectrum, all four of our polymers are relatively stable under thermal annealing conditions (120 °C) and beyond. Only when the temperature is increased beyond 250 °C, do we see a noticeable mass loss. DSC measurements were performed from 0 to 250 °C for all four polymers. For polymer N6r-C, we see glass transition temperature (T_g) at 75 °C and crystallization point (T_c) at 150 °C. For N6r-CC, we see T_g at 40 °C and T_c at 85 °C. Similarly, we observed T_g at 78 and 40 °C and T_c at 150 and 90 °C for polymers N10r-C and N10r-CC, respectively.

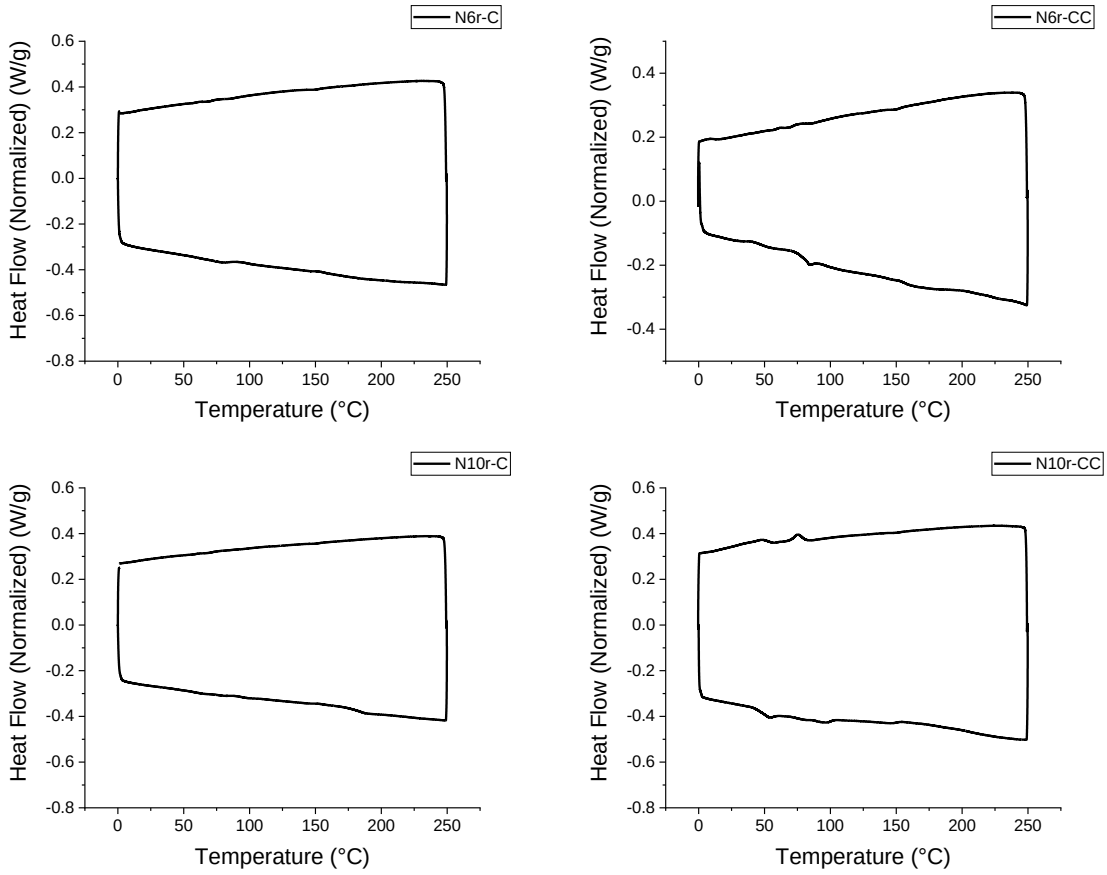

Figure 5.4: DSC spectra for Benzotriazole polymers.

5.2.4 DFT Results

DFT optimized molecular geometry results indicated linear polymeric backbones for N6r-CC and N10r-CC and coiled polymeric backbones for N6r-C and N10r-C. This was to be expected as our carbazole monomer was functionalized at different positions to achieve curvature for N6r-

C and N10r-C polymers. This was done to improve OLET performance, as explained in Chapters 3 and 4.

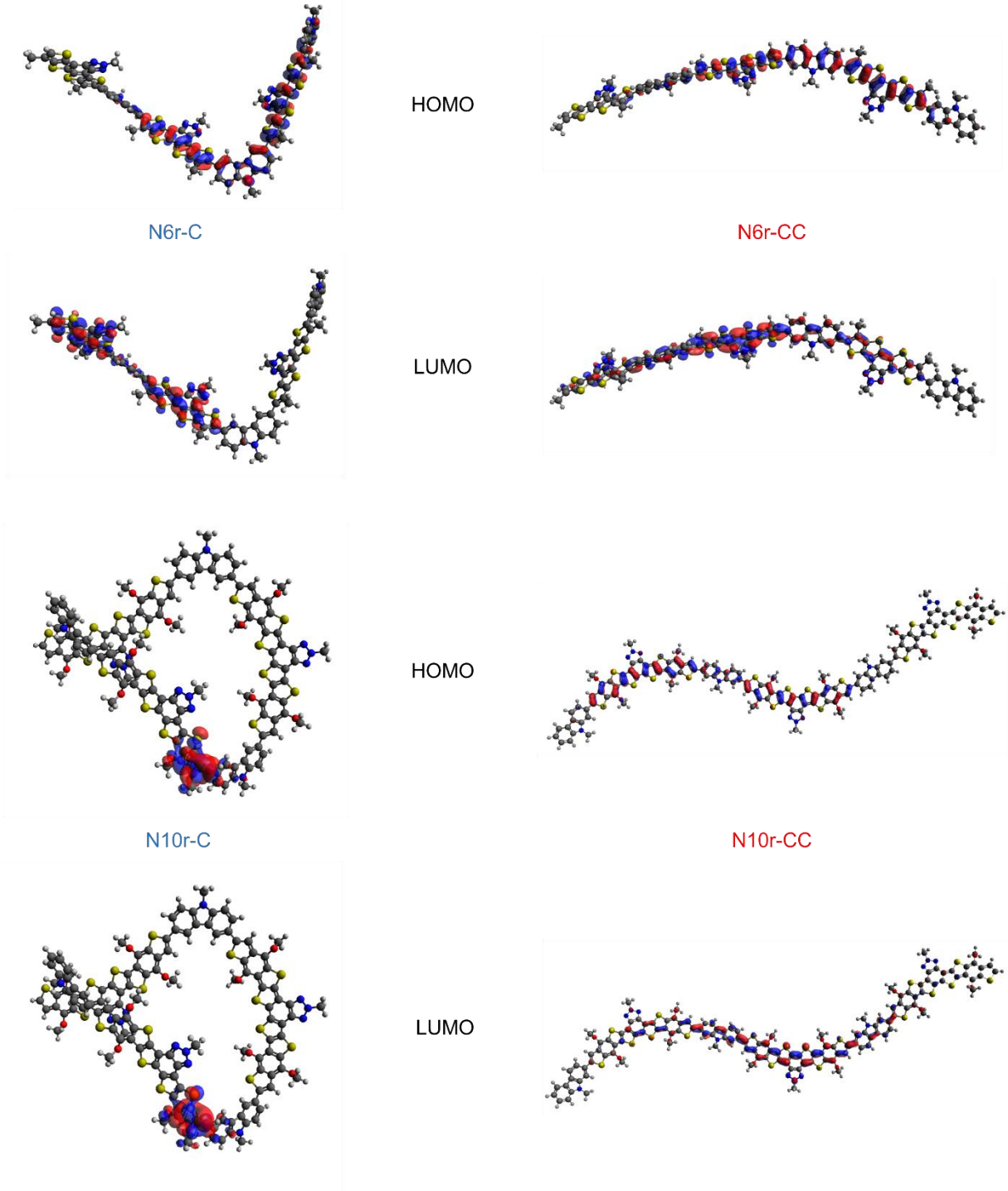

Figure 5.5: DFT results for Benzotriazole polymers

5.2.5 Optical Characterizations

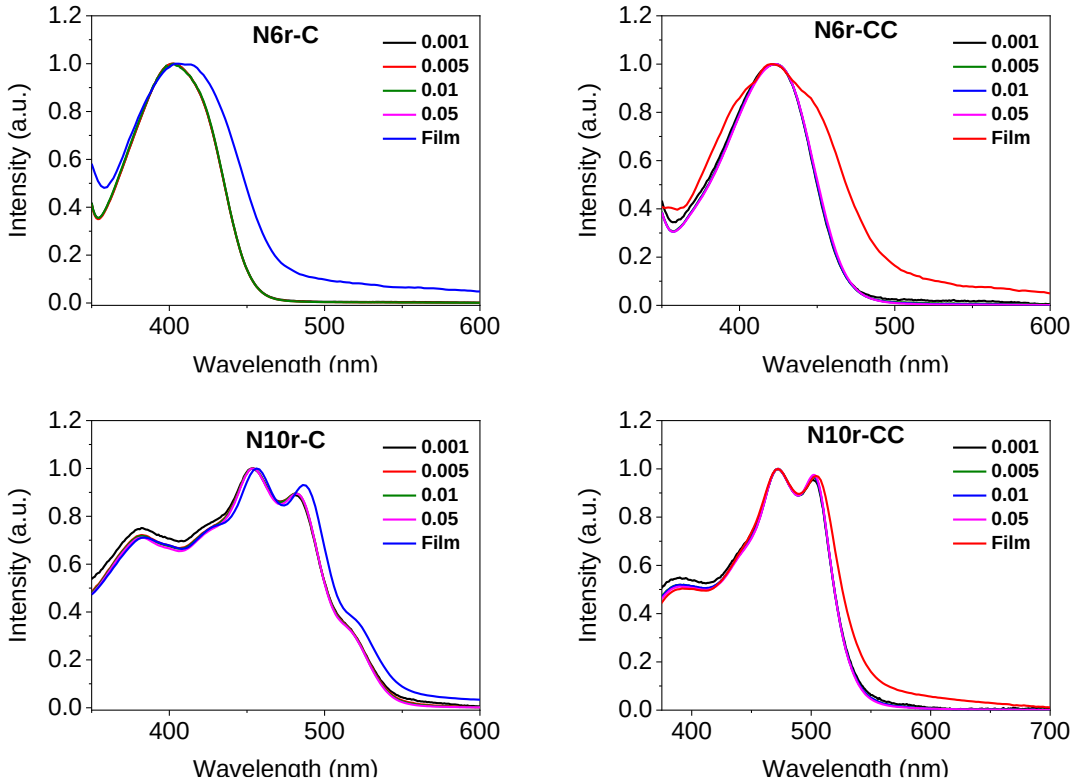

Figure 5.6: UV-Vis absorption spectra for Benzotriazole polymers

The concentration-dependent UV-Vis absorption spectra for all four polymers are shown in **Figure 5.6**. Both N6r-C and N6r-CC polymers exhibit one broad solution absorption peak that is independent of concentration. The absorption peak for N6r-C is further broadened and redshifted in its thin-film spectrum. The film absorption spectrum for the polymer N6r-CC, however, exhibits a different set of characteristics. Here, we see 0-0 and 0-2 shoulders in addition to the primary 0-1 peak.

Like the absorption spectra for N6r polymers, the absorption spectra for both N10r polymers are also concentration-independent. However, unlike the absorption spectra for N6r polymers, the absorption spectra for N10r polymers exhibits fine structure. For instance, the spectrum for N10r-C exhibits 0-0, 0-1, and 0-2 peaks, with the 0-2 peak being the most intense, followed by 0-1 and then 0-0 peaks. Also, its thin-film spectrum shows a very slight red-shift with

an increase in the I_A^{0-1}/I_A^{0-2} ratio. However, the polymer N10r-CC exhibits only 0-0 and 0-1 peaks and not a 0-2 peak. Additionally, there is a slight increase in the I_A^{0-0}/I_A^{0-1} ratio in its thin-film spectrum.

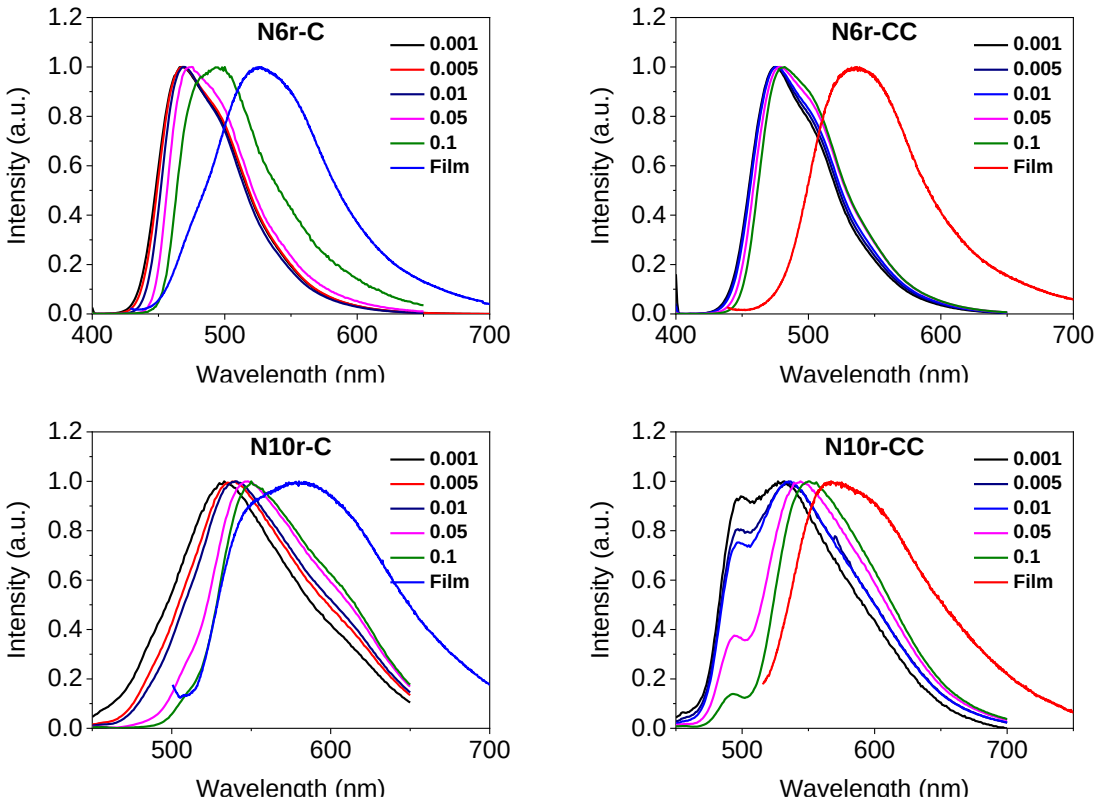

Figure 5.7: Emission spectra for Benzotriazole polymers

We further performed concentration-dependent photoluminescence measurements (**Figure 5.7**) to understand polymeric aggregation. Before we apply the rules concerning the vibronic signatures as per Frenkel exciton theory, it is necessary to note two significant differences between these four polymers and those synthesized in the previous chapters. The first difference concerns the structural symmetry of this new series of polymers, or more accurately, the lack thereof. For instance, all polymers synthesized in the previous chapters integrated centrosymmetric TPTI/TPTQ/FFPQ monomers, and if the resulting polymer exhibited a trans symmetry, the inversion center would be retained. This meant that the resulting polymers were quadropolar dyes

and could exhibit non-Kasha behavior, such as redshifted H-aggregates. [10–12] However, all four polymers synthesized in this chapter lack an inversion center, even in the trans configuration, and therefore exhibit traditional Kasha behavior. The second difference concerns the low molecular weight of all four polymers, making folding and, by extension, intramolecular interactions slightly more challenging.

The emission spectra of polymer N6r-C exhibit a single intense 0-0 transition in both solution and thin-film. While there is no red-shift with increasing concentration until 0.01 mg/mL, there is a slight red-shift as the concentration increases to 0.05 mg/mL and a significant red-shift as we increase the concentration further. The solid-state thin-film spectrum exhibits an additional red-shift. This is all indicative of J-aggregation. A similar trend can be observed for the polymer N10r-C as the polymer spectra exhibit red-shifts with increasing concentration and then further red-shifts in thin-films. Therefore we can conclude that N10r-C also exhibits J-aggregation. This makes sense since both the polymers are coiled and would prefer intrachain aggregation, which is characteristic of J aggregates in Kasha-model. [13]

A different set of trends is observed for polymers N6r-CC and N10r-CC. Taking polymer N6r-CC as an example, we see two groups of peaks in the solution spectrum. A 0-0 peak at 475 nm and a 0-1 shoulder peak at around 500 nm. Here we see no red-shifts with increasing concentration. However, we do see a decrease in the I_A^{0-0}/I_A^{0-1} ratio with increasing concentration. Additionally, we see both 0-0 and 0-1 peaks completely suppressed in thin-film spectra, with 0-2 being the dominant peak. This is indicative of interchain H-aggregation. We observe a similar set of trends for polymer N10r-CC. Two sets of peaks in solution spectra appear as a 0-0 peak at 490 nm and a 0-1 peak at 530 nm. A decrease in I_A^{0-0}/I_A^{0-1} ratio with increasing concentration was

observed, and the 0-0 peak was suppressed entirely in the thin film. This is again indicative of H-aggregation.

5.3 Device Fabrication

5.3.1 OFET Fabrication

Table 5.2: Charge carrier mobility values for Benzotriazole polymers

Material	μ_h ($cm^2V^{-1}s^{-1}$)	μ_e ($cm^2V^{-1}s^{-1}$)
N6r-C[a]	7.2×10^{-5}	-
N6r-CC[a]	5.3×10^{-5}	-
N10r-C[a]	1.4×10^{-5}	-
N10r-CC[a]	6.2×10^{-6}	-
N6r-C[b]	3.0×10^{-1}	7.4×10^{-3}
N6r-CC[b]	-	-
N10r-C[b]	1.7×10^{-1}	2.7×10^{-3}
N10r-CC[b]	5.6×10^{-2}	1.5×10^{-3}

a Mobility calculated from OTS modified OFET devices; b Mobility calculated from OTS modified OLET devices.

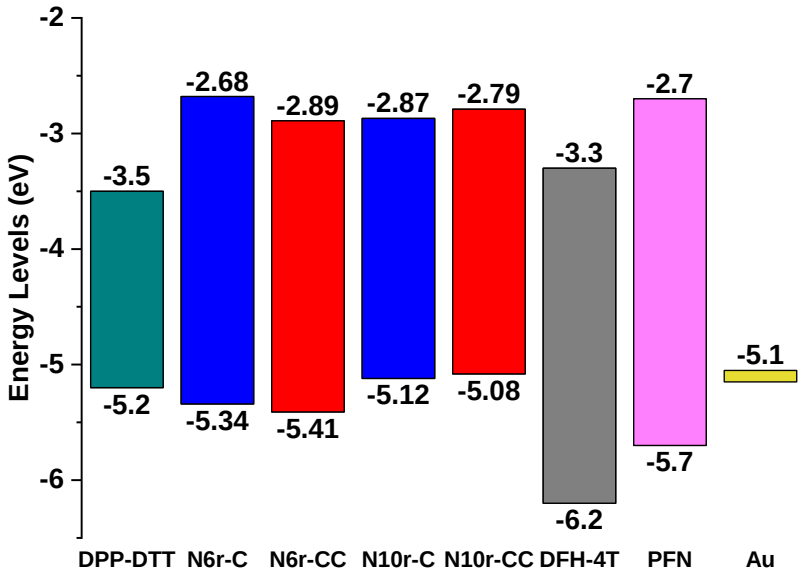

Figure 5.8: Energy Level diagram for Benzotriazole polymers.

We firstly fabricated single-layered bottom-gate top-contact OFET devices and measured their mobilities. These values are summarized in **Table 5.2**. It is clear from the data that all of these devices are p-type and, therefore, only exhibit hole mobility. This is understandable when you look at the energy level diagram in **Figure 5.8**. Here, the energetic barrier for hole injection from the gold electrode to the active layer in single-layered devices is around 0.25 eV. In comparison, the barrier for electron injection is an order of magnitude larger (~2.5 eV). Therefore, it is unlikely that any electrons would be able to surmount that barrier at room temperature. Additionally, we can notice that even the hole mobility in these devices is very low, and therefore it comes as no surprise that none of these devices exhibited any electroluminescence

5.3.2 OLET Fabrication

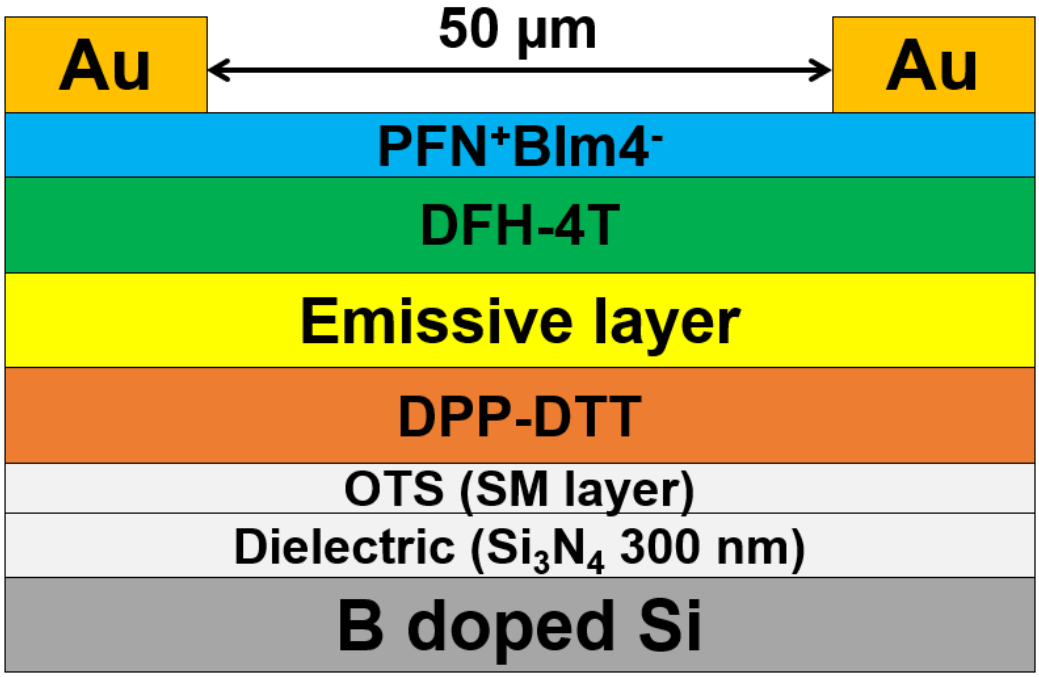

Figure 5.9: OLET Device architecture for Benzotriazole polymers

As shown previously, it was necessary to employ a multi-layered device architecture. The overall device architecture in **Figure 5.9** was as follows: Si/Si_3N_4/OTS/DPP-DTT/Emissive layer/DFH-4T/PFN^+BIm4^-/Au. The functionalities of these individual layers and components of our OLET device have been described in the previous chapters and will not be listed here.

To achieve the best possible OLET performance, we chose to employ the device architecture identical to the one used for the polymer FFPQ-C in the previous chapter. For this reason, the addition of the DFH-4T layer was necessary. This layer also exhibited decent electron mobility, which cannot be achieved with just a PFN^+BIm4^- layer.

Previously, the LUMO energy level of DFH-4T matched well with the LUMO energy level of FFPQ-C and helped with electron transport. However, in the case of our new polymer system, this wasn't the case and the energy levels differed by half an eV. We compared the polymer N6r-C OLET device with and without the DFH-4T layer. We wanted to test if the improvement in

electron mobility was enough to overcome the unfavorable energy barrier. As you can see in **Figure 5.10,** the emission intensity, while low by standards established previously, was definitely higher with an additional DFH-4T layer than without it.

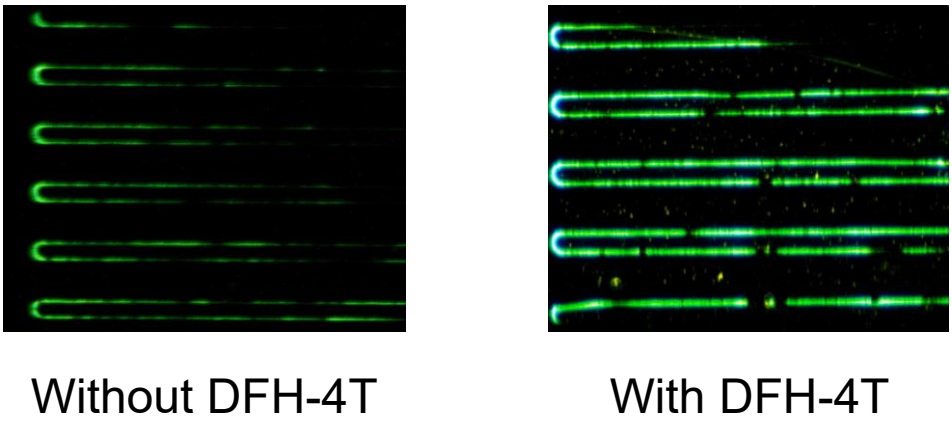

Figure 5.10: Electroluminescence for N6r-C with and without DFH-4T

Therefore, all future OLET devices for this series of polymers were fabricated with an additional DFH-4T layer. Unfortunately, as is evident in **Figure 5.11,** the rest of the polymers exhibited very weak emission. In fact, the emission was so weak that we failed to elicit a signal to calculate the EQE and EL intensity of our devices. This was a consequence of two factors, both of which were related to solubility. To prevent the DPP-DTT layer from dissolving, we employed orthogonal toluene to spin coat the emissive layer on top of the DPP-DTT layer. However, our polymer emissive layer was only poorly soluble in toluene, which meant that it was challenging to coat a layer thick enough for device purposes. This problem could be partially solved by employing the dual solvent method, which involved dissolving the emissive layer in chloroform, adding toluene, and then evaporating the chloroform solvent. However, the DFH-4T layer, which followed the emissive layer, was only soluble in chloroform, which would also dissolve the emissive layer underneath. For this reason, it was challenging to fabricate decent quality devices.

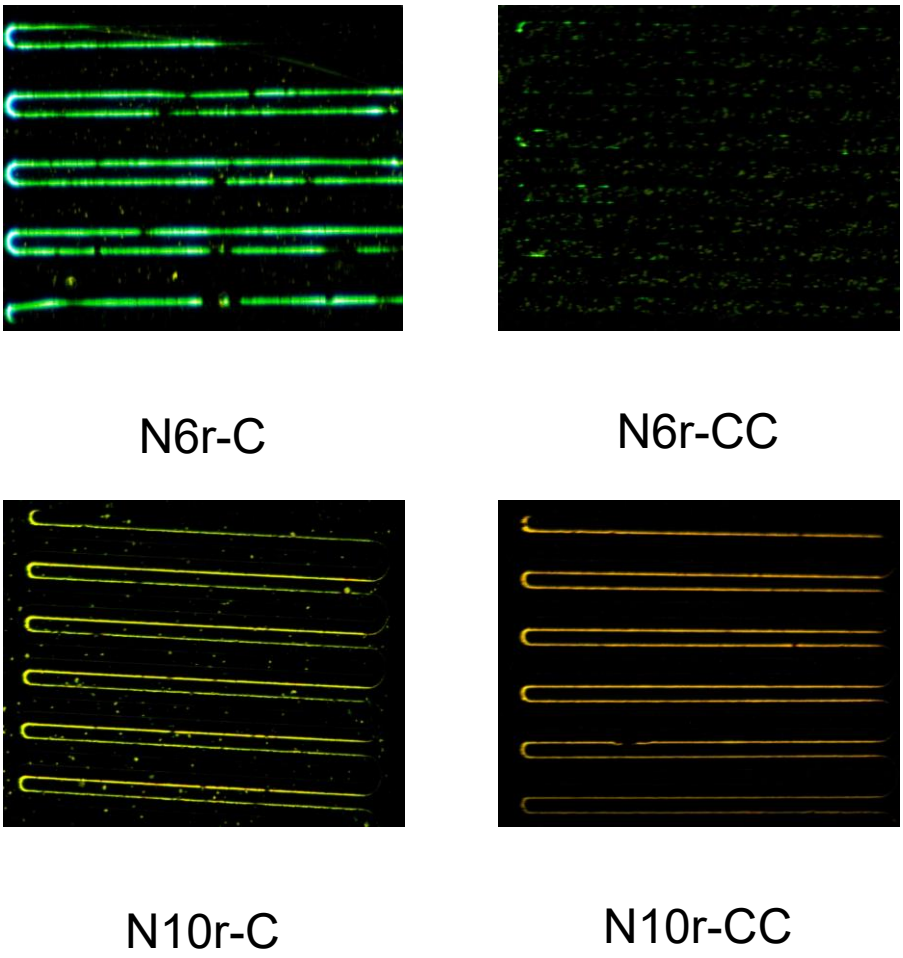

Figure 5.11: Electroluminescence for Benzotriazole polymers

However, our polymers' OLET devices did exhibit fairly decent charge transport mobilities despite poor emissive properties. To put it in perspective, the hole mobilities of this series of polymers were, on average, at least an order of magnitude larger than those of our polymers in the previous chapter. Among these four polymers, N6r-CC exhibited the highest PLQY in solution (80.6%). Therefore, it was somewhat surprising for its devices to exhibit the weakest emission. Again, the low solubility of N6r-CC is in play here, which would make the resulting emissive layers thin, and nonuniform and, therefore, the devices to be of unsatisfactory quality. Clearly, ethyl hexyl alkyl side chains were not enough to solubilize the polymers. Consequently, it would be wise to employ longer alkyl chains such as butyl octyl groups in the future.

5.4 Conclusion

This chapter describes the design and synthesis of four semi-ladder copolymers, N6r-C, N6r-CC, N10r-C, and N10r-CC. These polymer systems were chosen because we wanted to move away from the TPTI/TPTQ/FFPQ series of compounds and test an entirely new system. [14–16] It was found that slight chemical structure changes led to differences in energy levels, emission, and polymeric packing. While all four polymers exhibit suitable energy levels and decent charge carrier mobility, they failed to display decent emission. In fact, the emission was so poor that it was unable to register any discernable signal in the photodetector. Solubility issues and stringent orthogonal solvent requirements were the primary reasons for less than impressive performance. However, these results alone are not enough to rule out benzotriazole polymers as suitable systems for OLET applications. It is entirely possible that sidechain engineering can successfully address the solubility issues and yield impressive results.

5.5 Materials and Methods

Compounds 16, 20, and 22 were synthesized as per literature procedures. [17–19]

5.5.1 Synthesis

Compound 17: Compound 16 (1 eq) and CH_3SNa (3 eq) were suspended in a 10/20 ml DMF/THF mixture. The resulting suspension was stirred at room temperature for 2 hours, after which it was poured into water and extracted with diethyl ether. The organic layer was washed with water, dried over $MgSO_4$, and the solvent was removed under reduced pressure. The crude mixture was then purified by silica gel chromatography eluted with hexanes:DCM (1:1) to afford Compound 17 as colorless oil in an 82% yield. ^{1}H-NMR (500 MHz, CDCl3): δ (ppm) 7.58 (s, 2H), 4.56 (d, 2H), 2.52 (s, 6H), 2.17 (m, 1H), 1.27 (m, 8H), 0.90 (m, 6H). ^{13}C-NMR (100 MHz, CDCl3): δ (ppm) 143.2, 137.4, 113.8, 59.6, 40.5, 30.5, 28.5, 23.8, 22.8, 16.8, 14.0, 10.5.

Compound 18: Compound 17 (1 eq) was dissolved in DCM cooled to 0 °C in the dark. Bromine (10 eq) was then added dropwise, and the solution was stirred at room temperature overnight, after which it was poured into water and extracted with DCM. The organic layer was washed with saturated Na_2SO_3, dried over $MgSO_4$, and the solvent was removed under reduced pressure. The crude mixture was then purified by silica gel chromatography eluted with hexanes:DCM (1:1) to afford Compound 18 as a pale yellow oil in a quantitative yield. ^{1}H-NMR (500 MHz, CDCl3): δ (ppm) 4.68 (d, 2H), 2.56 (s, 6H), 2.30 (m, 1H), 1.33 (m, 8H), 0.93 (t, 3H), 0.86, (t, 3H). ^{13}C-NMR (100 MHz, CDCl3): δ (ppm) 144.0, 140.8, 119.4, 60.8, 40.3, 30.2, 28.2, 23.6, 22.9, 20.9, 14.0, 10.3.

Compound 19: Compound 18 (1 eq) was dissolved in 40 mL chloroform and cooled to -40 °C. m-CPBA (2 eq) was dissolved in 20 mL chloroform and added dropwise to a solution of Compound 18. After stirring at room temperature for 30 mins, the solution was quenched with $NaHCO_3$. The organic layer was washed with water, dried over $MgSO_4$, and the solvent was removed under reduced pressure. The crude mixture was then purified by silica gel chromatography eluted with DCM:ethyl acetate (1:1) to afford compound 19 as a white solid in a 78% yield. ^{1}H-NMR (500 MHz, CDCl3): δ (ppm) 4.70 (d, 2H), 3.36 (s, 3H), 3.30 (s, 3H), 2.25 (m, 1H), 1.30 (m, 8H), 0.91 (m, 3H), 0.86, (m, 3H). ^{13}C-NMR (100 MHz, CDCl3): δ (ppm) 143.9, 141.6, 113.1, 61.3, 40.4, 38.7, 30.2, 28.2, 23.7, 22.8, 14.0, 10.4. MS (MALDI-TOF) *m*/*z* 513.45 (M+), calcd 513.31.

Compound 21: Compound 19 (1 eq), Compound 20 (2.5 eq), K_2CO_3 (4 eq), Aliquat 336 (3 drops), and $Pd(PPh_3)_4$ (0.05 eq) were dissolved in 100 mL of Toluene/H_2O (10:1). The mixture was degassed for 30 minutes and refluxed overnight. After cooling to room temperature, the mixture was poured into water and extracted with DCM. The organic layer was dried with $MgSO_4$, and the solvent was removed under reduced pressure. The crude mixture was purified by column chromatography on silica gel with hexane:ethyl acetate (9:1) to get yellow oil in a 45% yield. ^{1}H-NMR (500 MHz, CDCl3): δ (ppm) 7.19 (d, 4H), 4.62 (m, 1H), 4.14 (m, 1H), 3.27 (s, 3H), 3.16 (s, 3H), 2.64 (m, 4H), 2.17 (m, 1H), 1.56 (m, 2H), 1.26 (m, 24H), 0.89 (m, 18H). MS (MALDI-TOF) *m*/*z* 744.29 (M+), calcd 744.19.

N6r: Compound 21 (1 eq) and P_2O_5 (10 eq) were suspended in 50 mL TFA. The mixture was stirred at 50 °C overnight. Then it was poured into 100 mL crushed ice and stirred vigorously to afford a red oil. The oil was isolated and dissolved in 50 mL pyridine. The resulting solution was refluxed overnight. After cooling to room temperature, the mixture was poured into water and extracted with DCM. The organic layer was dried with $MgSO_4$, and the solvent was removed under

reduced pressure. The crude mixture was purified by column chromatography on silica gel with hexanes:DCM (3:1) to afford compound N6r as a yellow oil in 22 % yield. ^{1}H-NMR (500 MHz, CDCl3): δ (ppm) 7.20 (s, 2H), 4.81 (d, 2H), 2.77 (d, 4H), 2.35 (m, 1H), 1.90 (m, 2H), 1.37 (m, 24H), 0.96 (m, 18H). MS (MALDI-TOF) *m*/*z* 680.03 (M+), calcd 680.10.

Br-N6r-Br: N6r (1 eq) was dissolved in chloroform, and the solution cooled to 0 °C in the dark. NBS (2.2 eq) in chloroform was then added dropwise, after which the solution was warmed to room temperature and stirred for 2 hours. The reaction mixture was then poured into water and extracted with chloroform. The organic layer was dried with $MgSO_4$, and the solvent was removed under reduced pressure. The crude mixture was purified by column chromatography on silica gel with hexanes:DCM (3:1) to afford compound Br-N6r-Br as a yellow solid in an 80% yield. ^{1}H-NMR (500 MHz, CDCl3): δ (ppm) 4.77 (d, 2H), 2.76 (d, 4H), 2.31 (m, 1H), 1.97 (m, 2H), 1.39 (m, 24H), 0.98 (m, 18H). MS (MALDI-TOF) *m*/*z* 837.81 (M+), calcd 837.90.

Compound 23: Compound 19 (1 eq), Compound 22 (2.5 eq)), and $Pd(PPh_3)_4$ (0.05 eq) were dissolved in 100 mL of Toluene. The mixture was degassed for 30 minutes and refluxed overnight. After cooling to room temperature, the mixture was poured into water and extracted with DCM. The organic layer was dried with $MgSO_4$, and the solvent was removed under reduced pressure. The crude mixture was purified by column chromatography on silica gel with hexane:ethyl acetate (9:1) to get Compound 23 as a yellow oil in a 43% yield. ^{1}H-NMR (500 MHz, CDCl3): δ (ppm) 7.75 (s, 2H), 7.73 (s, 2H), 4.64 (d, 2H), 4.33 (m, 8H), 3.43 (s, 6H), 2.25 (m, 1H), 1.87 (m, 4H), 1.45 (m, 46H), 1.25 (d, 36H), 1.07 (m, 12H), 0.97 (m, 12H), 0.93, (m, 3H), 0.86, (m, 3H). ^{13}C-NMR (100 MHz, CDCl3): δ (ppm) 144.7, 143.4, 137.6, 134.0, 133.6, 132.4, 130.9, 130.6, 128.6, 124.4, 76.0, 75.8, 60.9, 40.7, 30.7, 30.5, 30.4, 29.4, 29.3, 28.3, 24.0, 23.2, 18.7, 14.2, 11.9. MS (MALDI-TOF) *m*/*z* 1556.43 (M+), calcd 1555.59.

N10r: Compound 23 (1 eq) and P_2O_5 (10 eq) were suspended in 50 mL TFA. The mixture was stirred at 50 °C overnight. Then it was poured into 100 mL crushed ice and stirred vigorously to afford a red oil. The oil was isolated and dissolved in 50 mL pyridine. The resulting solution was refluxed overnight. After cooling to room temperature, the mixture was poured into water and extracted with DCM. The organic layer was dried with $MgSO_4$, and the solvent was removed under reduced pressure. The crude mixture was purified by column chromatography on silica gel with hexanes:DCM (3:1) to afford compound N10r as a yellow oil in 23 % yield. ^{1}H-NMR (500 MHz, CDCl3): δ (ppm) 7.56 (d, 2H), 7.45 (d, 2H), 4.89 (d, 2H), 4.40 (d, 4H), 4.30 (d, 4H), 2.44 (m, 1H), 2.18 (m, 2H), 1.93 (m, 4H), 1.71 (m, 12H), 1.50 (m, 26H), 1.19 (t, 6H), 1.10 (m, 21H), 0.97 (t, 3H). ^{13}C-NMR (100 MHz, CDCl3): δ (ppm) 145.2, 143.9, 138.3, 136.4, 132.7, 132.5, 129.8, 129.2, 126.0, 124.8, 126.4, 124.8, 120.6, 120.0, 76.4, 75.9, 59.5, 40.9, 40.8, 40.4, 30.5, 30.4, 29.3, 28.4, 24.0, 23.9, 23.8, 23.2, 23.0, 14.3, 14.1, 11.4. MS (MALDI-TOF) *m*/*z* 1179.71 (M+), calcd 1180.82.

Br-N10r-Br: N10r (1 eq) was dissolved in chloroform, and the solution cooled to 0 °C in the dark. NBS (2.2 eq) in chloroform was then added dropwise, after which the solution was warmed to room temperature and stirred for 2 hours. The reaction mixture was then poured into water and extracted with chloroform. The organic layer was dried with $MgSO_4$, and the solvent was removed under reduced pressure. The crude mixture was purified by column chromatography on silica gel with hexanes:DCM (3:1) to afford compound Br-N10r-Br as a yellow solid in a 75% yield. ^{1}H-NMR (500 MHz, CDCl3): δ (ppm) 7.31 (s, 2H), 4.82 (m, 2H), 4.19 (br, 8H), 2.39 (m, 1H), 2.12 (m, 4H), 1.72 (m, 40H), 1.10 (m, 30H). MS (MALDI-TOF) *m*/*z* 1338.68 (M+), calcd 1338.61.

General Procedure for Semi-Ladder Copolymers: A mixture of Br-N6r-Br/Br-N10r-Br monomer (1 eq), carbazole comonomer (1 eq), K_2CO_3 (4 eq), Aliquat 336 (3 drops), and $Pd(PPh_3)_4$ (0.05 eq) were dissolved in 4ml of Toluene/H_2O (10:1). The mixture was degassed for 30 minutes and then

refluxed for 72 hours. After cooling to room temperature, the mixture was passed through Celite and precipitated in methanol. The polymer fibers were then washed by Soxhlet extraction with methanol, acetone, hexanes, and chloroform. The final polymer was obtained after reprecipitation of chloroform fraction in methanol.

N6r-C: Yield: 73 %. ^{1}H-NMR (500 MHz, CDCl3): δ (ppm) 8.36 (br, 2H), 7.71 (br, 2H), 7.49 (br, 2H), 4.78 (br, 2H), 4.24 (br, 2H), 2.96 (br, 4H), 2.77 (br, 1H), 2.34 (br, 1H), 2.16 (br, 1H), 2.04 (br, 1H), 1.10-1.50 (m, 32H), 0.50-1.0 (m, 24H).

N6r-CC: Yield: 79 %. ^{1}H-NMR (500 MHz, CDCl3): δ (ppm) 8.18 (br 2H), 7.48 (br, 4H), 4.86 (br, 4H), 4.20 (br, 4H), 2.98 (br, 4H), 0.5-2.5 (br, 56H)

N10r-C: Yield: 76 %. ^{1}H-NMR (500 MHz, CDCl3): δ (ppm) 6.5-8.2 (br, 8H), 4.6-5.0 (br 4H), 3.6-4.5 (br, 8H), 0.5-2.5 (br, 90H).

N10r-CC: Yield: 76 %. ^{1}H-NMR (500 MHz, CDCl3): δ (ppm) 6.6-8.0 (br, 8H), 4.6-5.1 (br 4H), 3.8-4.5 (br, 8H), 0.8-2.5 (br, 90H).

5.5.2 Optical analysis

See Chapter 2

5.5.3 Device Fabrication

For OLET device fabrication, see the previous chapter

For OLED device fabrication, see Chapter 2

5.5.4 Device Measurements

See Chapter 2

5.6 References

(1) Gibson, G. L.; McCormick, T. M.; Seferos, D. S. Atomistic Band Gap Engineering in Donor-Acceptor Polymers. *J. Am. Chem. Soc.* **2012**, *134* (1), 539–547.

(2) Berberan-Santos, M. N. External Heavy-Atom Effect on Fluorescence Kinetics. *PhysChemComm* **2000**.

(3) Al Anshori, J.; Slanina, T.; Palao, E.; Klán, P. The Internal Heavy-Atom Effect on 3-Phenylselanyl and 3-Phenyltellanyl BODIPY Derivatives Studied by Transient Absorption Spectroscopy. *Photochem. Photobiol. Sci.* **2016**.

(4) Yuan, D.; Awais, M. A.; Sharapov, V.; Liu, X.; Neshchadin, A.; Chen, W.; Bera, M.; Yu, L. Foldable Semi-Ladder Polymers: Novel Aggregation Behavior and High-Performance Solution-Processed Organic Light-Emitting Transistors. *Chem. Sci.* **2020**.

(5) Yuan, D.; Awais, M. A.; Sharapov, V.; Liu, X.; Neshchadin, A.; Chen, W.; Yu, L. Highly Emissive Semi-Ladder-Type Copolymers, Aggregation State, and Solution-Processed Organic Light-Emitting Transistor. *Chem. Mater.* **2020**.

(6) Cai, Z.; Zhang, N.; Awais, M. A.; Filatov, A. S.; Yu, L. Synthesis of Alternating Donor-Acceptor Ladder-Type Molecules and Investigation of Their Multiple Charge-Transfer Pathways. *Angewandte Chemie - International Edition*. 2018.

(7) Usluer, O.; Demic, S.; Egbe, D. A. M.; Birckner, E.; Tozlu, C.; Pivrikas, A.; Ramil, A. M.; Sariciftci, N. S. Fluorene-Carbazole Dendrimers: Synthesis, Thermal, Photophysical and Electroluminescent Device Properties. *Adv. Funct. Mater.* **2010**.

(8) Wu, Y.; Wu, D.; Zhao, H.; Li, J.; Li, X.; Wang, Z.; Wang, H.; Zhu, F.; Xu, B. Synthesis and Properties of Hyperbranched Polymers for Polymer Light Emitting Devices with Sunlight-Style White Emission. *RSC Adv.* **2019**.

(9) Wang, Z.; Wang, C.; Gan, Q.; Cao, Y.; Yuan, H.; Hua, D. Donor-Acceptor-Type Conjugated Polymer-Based Multicolored Drug Carriers with Tunable Aggregation-Induced Emission Behavior for Self-Illuminating Cancer Therapy. *ACS Appl. Mater. Interfaces* **2019**.

(10) Spano, F. C.; Silva, C. H- and J-Aggregate Behavior in Polymeric Semiconductors. *Annu. Rev. Phys. Chem.* **2014**.

(11) Zheng, C.; Zhong, C.; Collison, C. J.; Spano, F. C. Non-Kasha Behavior in Quadrupolar Dye Aggregates: The Redshifted H-Aggregate. *J. Phys. Chem. C* **2019**.

(12) Spano, F. C. The Spectral Signatures of Frenkel Polarons in H- And J-Aggregates. *Acc. Chem. Res.* **2010**.

(13) Kasha, M. Characterization of Electronic Transitions in Complex Molecules. *Discussions*

of the Faraday Society. 1950.

(14) Jung, I. H.; Zhao, D.; Jang, J.; Chen, W.; Landry, E. S.; Lu, L.; Talapin, D. V.; Yu, L. Development and Structure/Property Relationship of New Electron Accepting Polymers Based on Thieno[2′,3′:4,5]Pyrido[2,3-g]Thieno[3,2-c]Quinoline-4,10-Dione for All-Polymer Solar Cells. *Chem. Mater.* **2015**, *27* (17), 5941–5948.

(15) Jung, I. H.; Lo, W.; Jang, J.; Chen, W.; Landry, E. S.; Lu, L.; Talapin, D. V; Yu, L.; Zhao, D. Synthesis and Search for Design Principles of New Electron Accepting Polymers for All-Polymer Solar Cells Synthesis and Search for Design Principles of New Electron Accepting Polymers for All-Polymer Solar Cells. **2014**.

(16) Adegoke, O. O.; Jung, I. H.; Orr, M.; Yu, L.; Goodson, T. Effect of Acceptor Strength on Optical and Electronic Properties in Conjugated Polymers for Solar Applications. *J. Am. Chem. Soc.* **2015**.

(17) Bin, H.; Zhang, Z. G.; Gao, L.; Chen, S.; Zhong, L.; Xue, L.; Yang, C.; Li, Y. Non-Fullerene Polymer Solar Cells Based on Alkylthio and Fluorine Substituted 2D-Conjugated Polymers Reach 9.5% Efficiency. *J. Am. Chem. Soc.* **2016**.

(18) Liu, C. F.; Jiu, Y.; Wang, J.; Yi, J.; Zhang, X. W.; Lai, W. Y.; Huang, W. Star-Shaped Single-Polymer Systems with Simultaneous RGB Emission: Design, Synthesis, Saturated White Electroluminescence, and Amplified Spontaneous Emission. *Macromolecules* **2016**.

(19) Fauvell, T. J.; Zheng, T.; Jackson, N. E.; Ratner, M. A.; Yu, L.; Chen, L. X. Photophysical and Morphological Implications of Single-Strand Conjugated Polymer Folding in Solution. *Chem. Mater.* **2016**.

APPENDICES

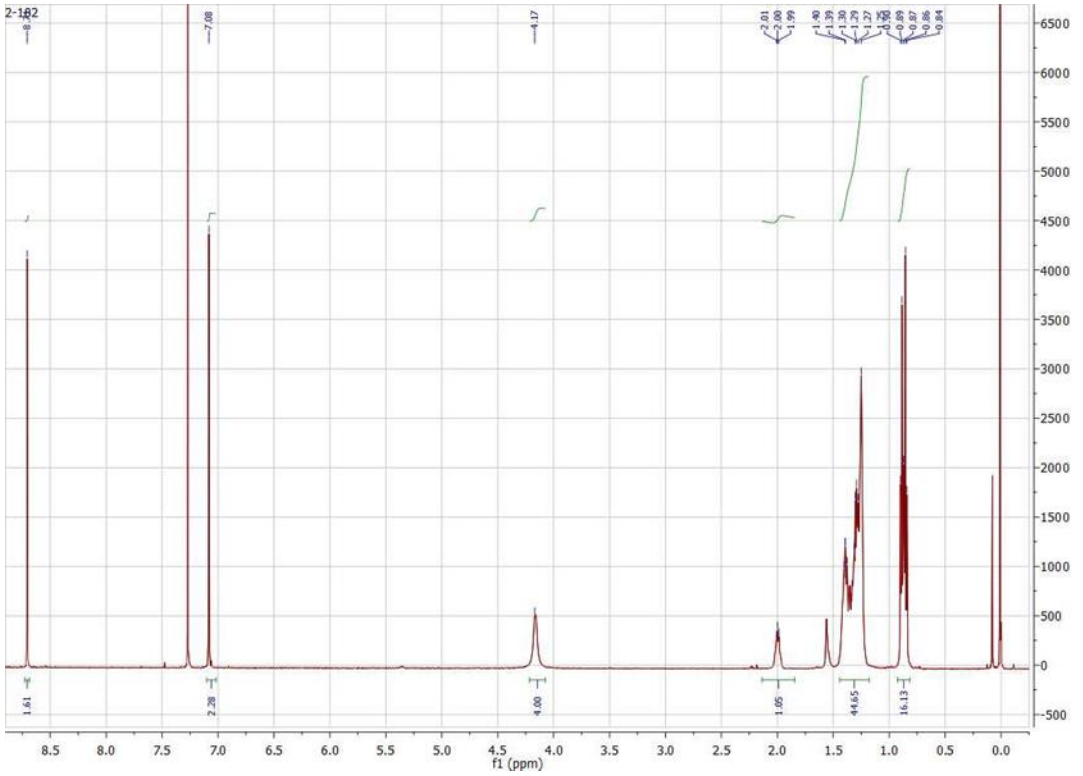

Appendix 1: ^{1}H NMR for Br-TPTI-Br

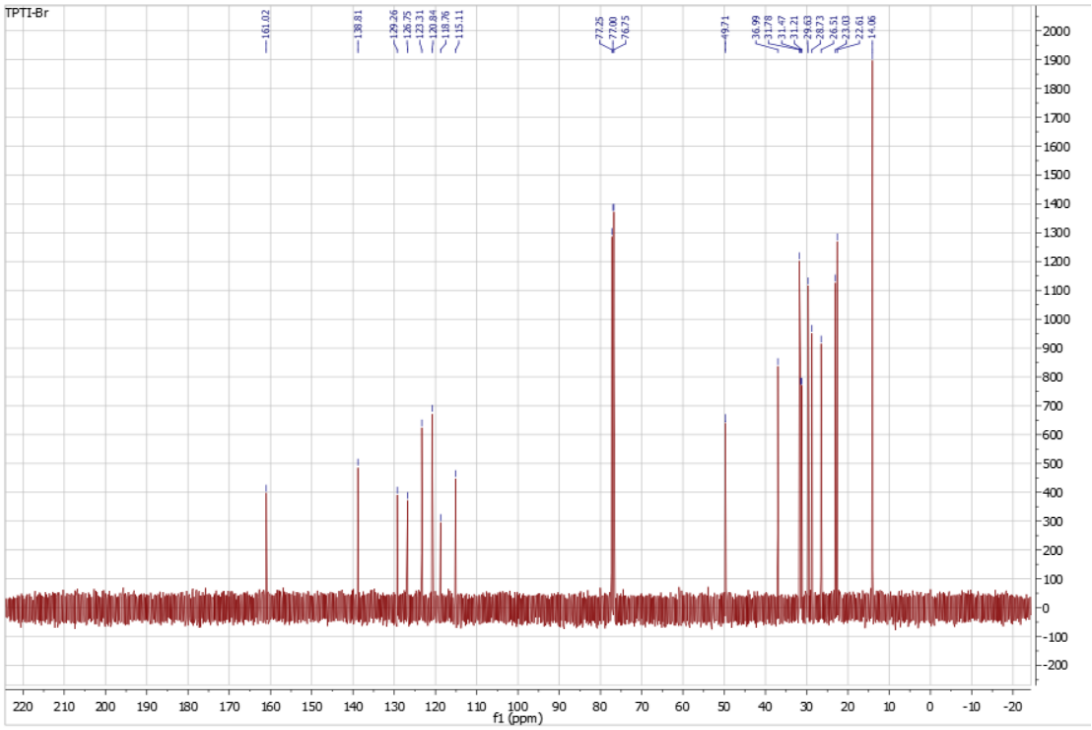

Appendix 2: ^{13}C NMR for Br-TPTI-Br

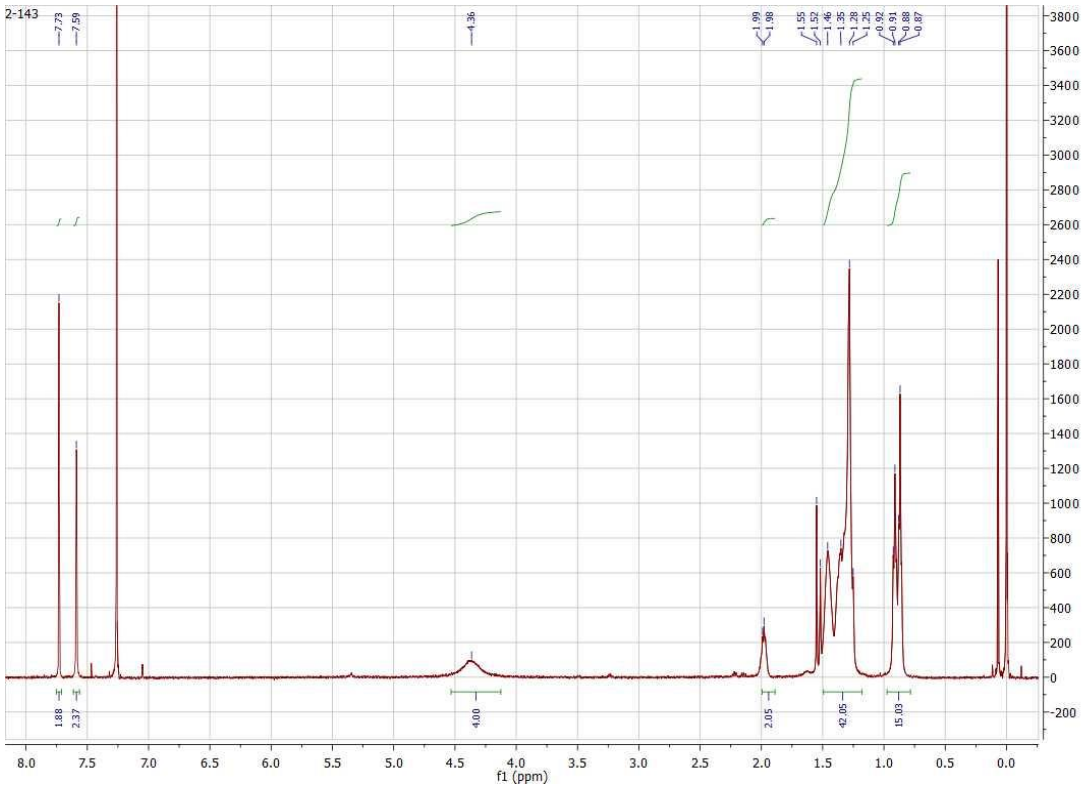

Appendix 3: ^{1}H NMR for Br-TPTQ-Br

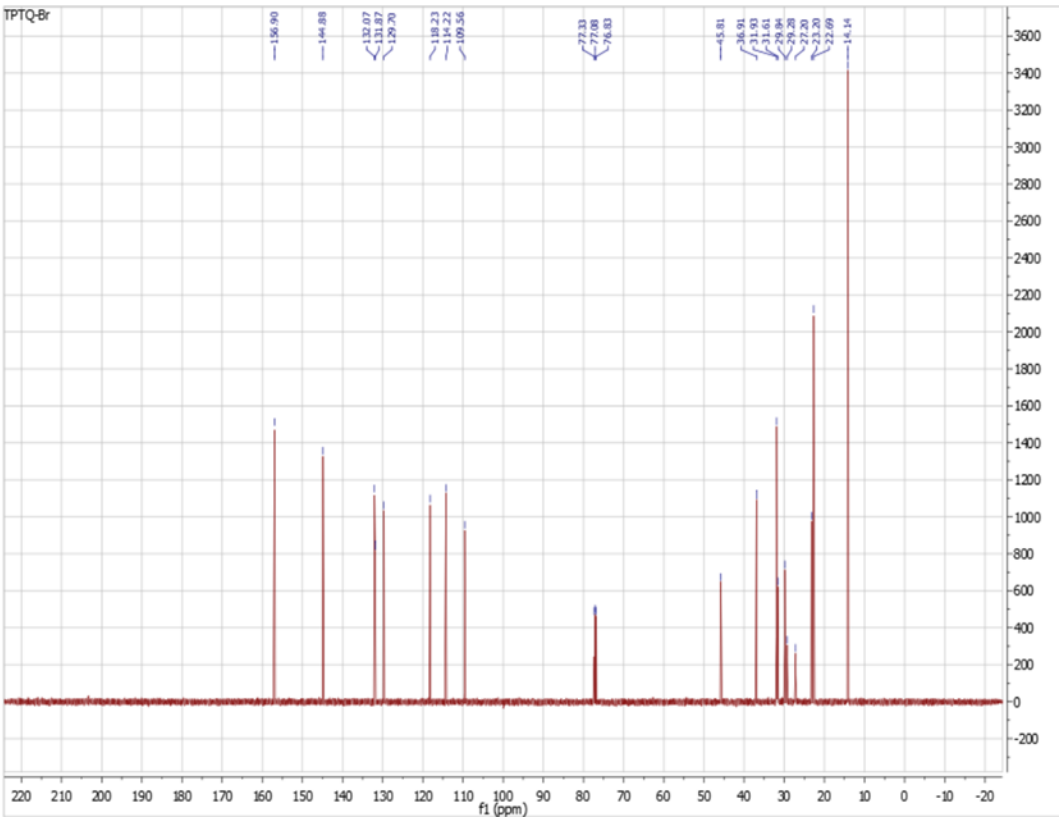

Appendix 4: ^{13}C NMR for Br-TPTQ-Br

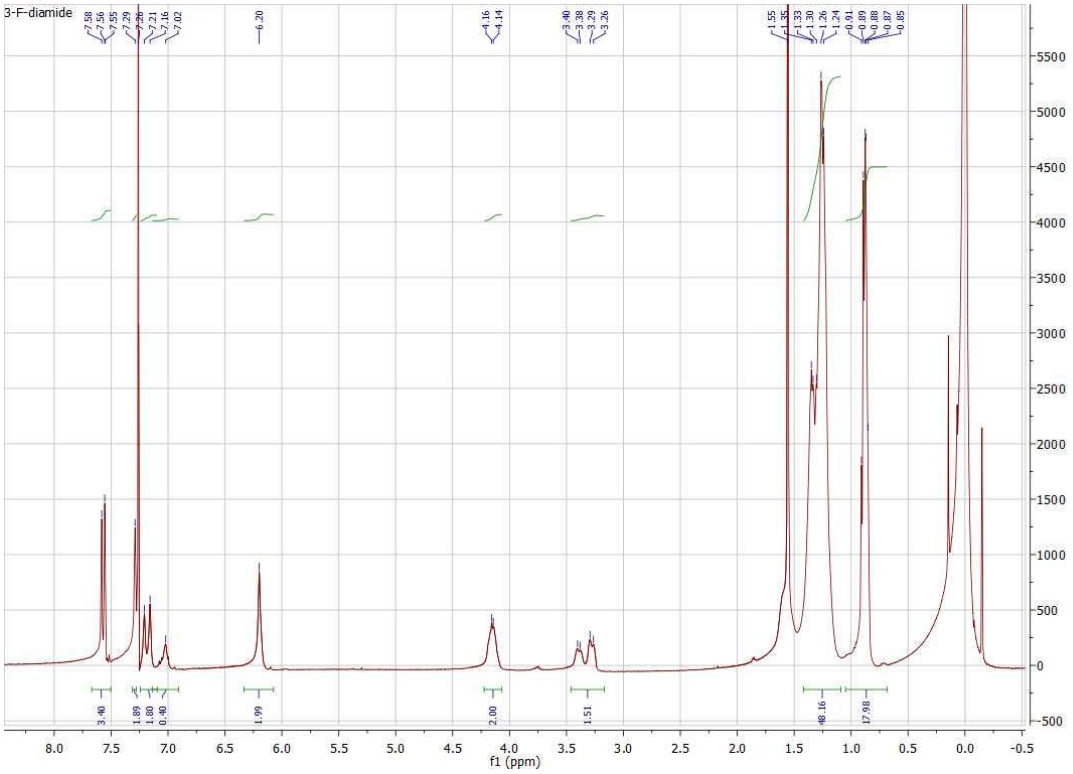

Appendix 5: ^{1}H NMR for Compound 11

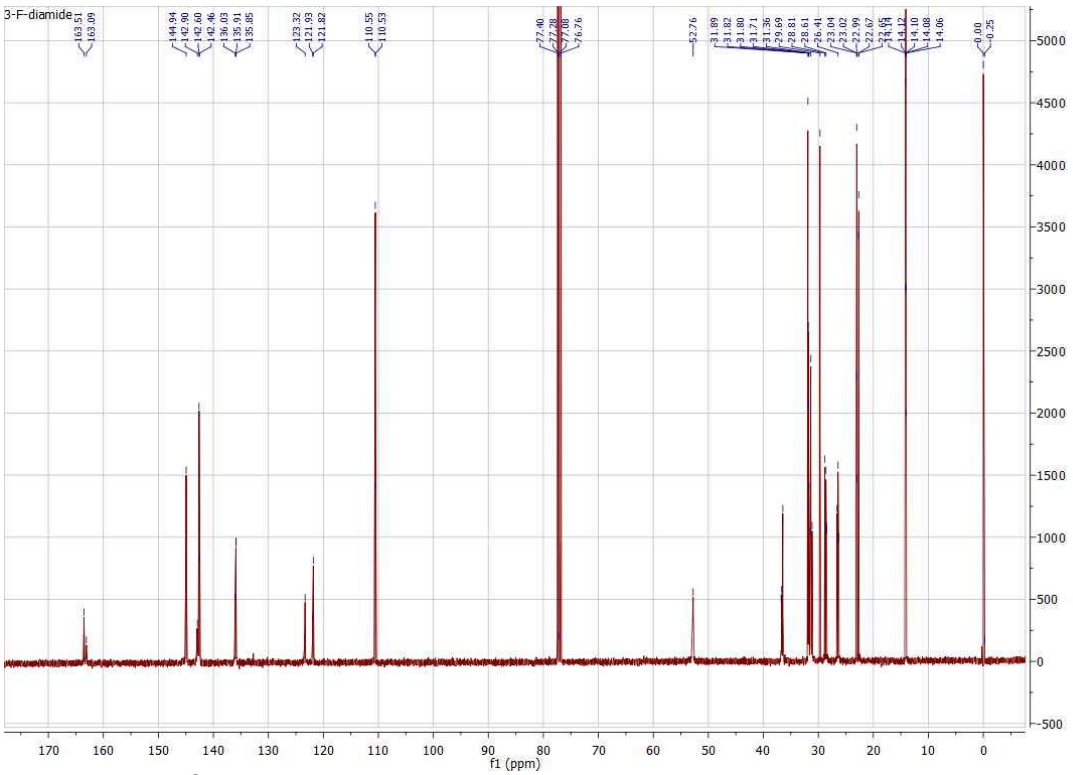

Appendix 6: ^{13}C NMR for Compound 11

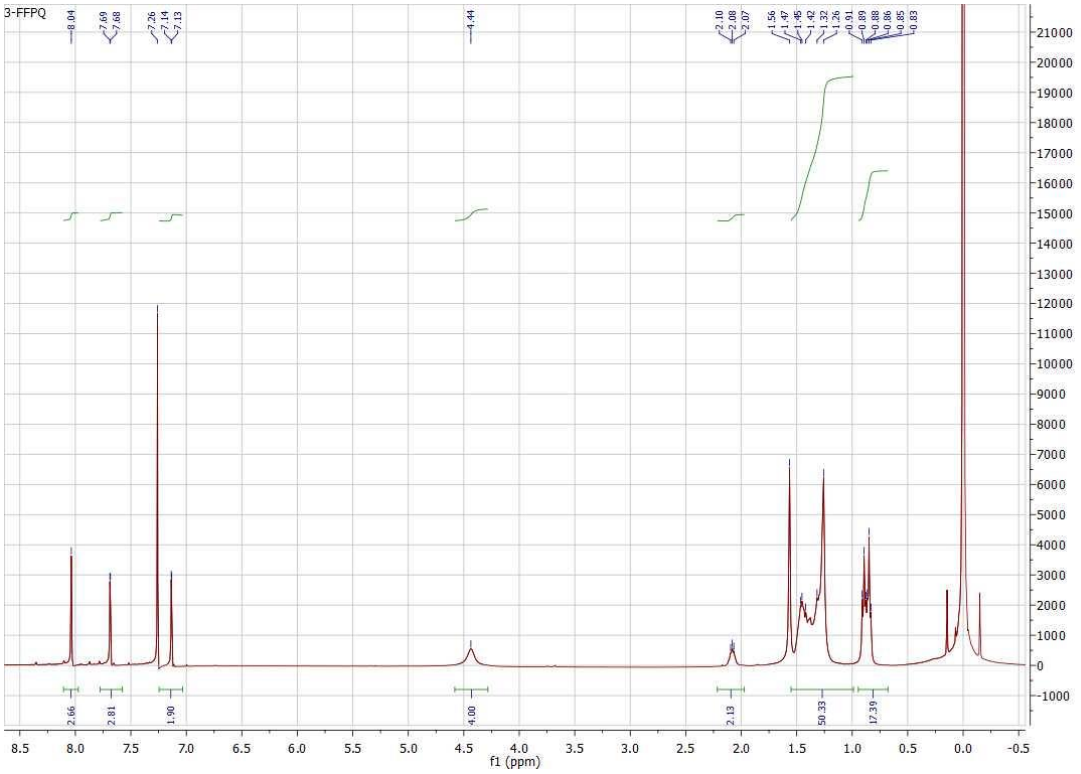

Appendix 7: ^{1}H NMR for FFPQ

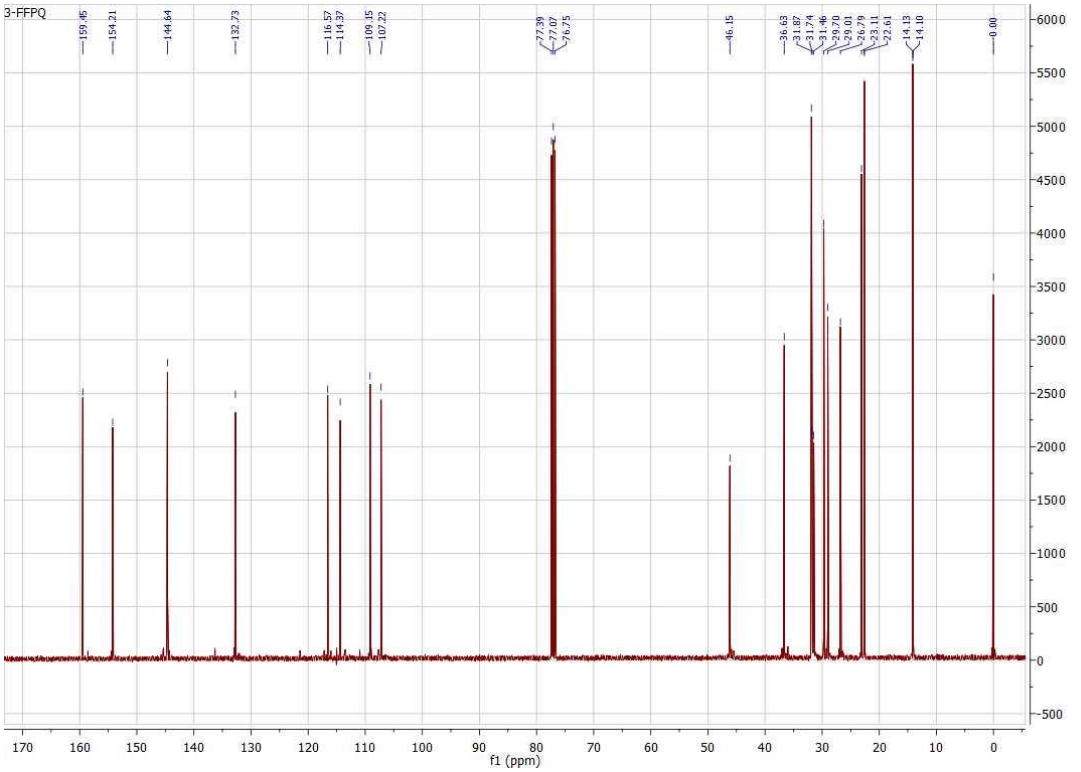

Appendix 8: ^{13}C NMR for FFPQ

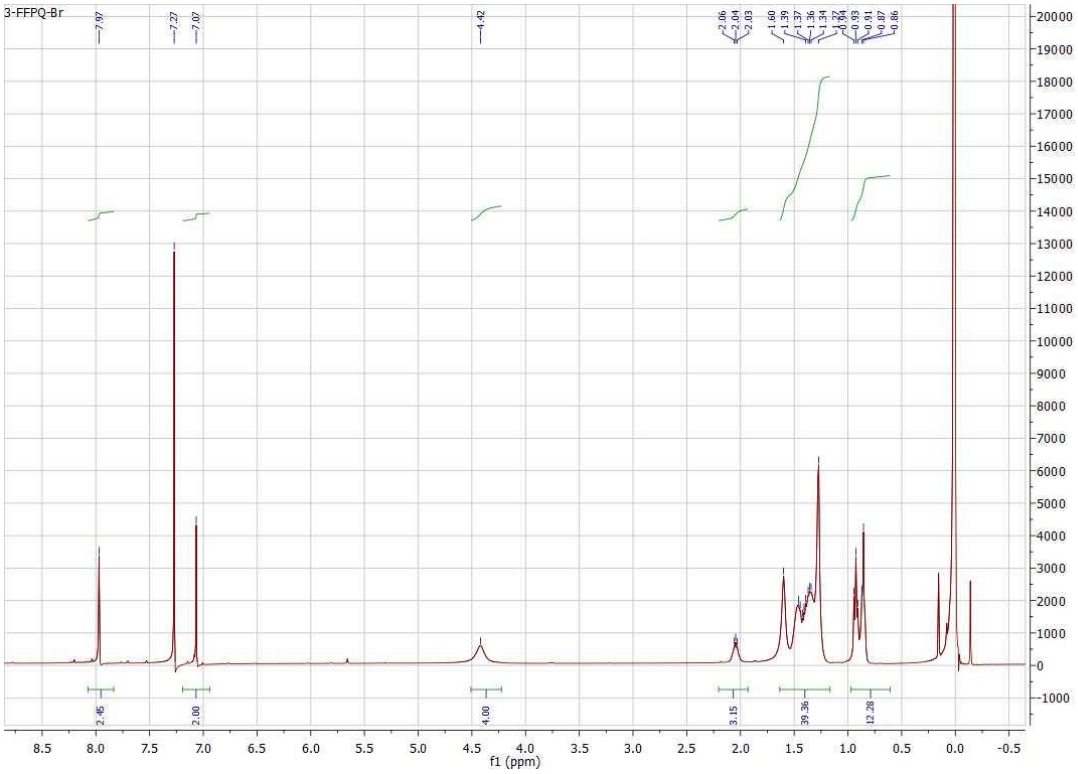

Appendix 9: ^{1}H NMR for Br-FFPQ-Br

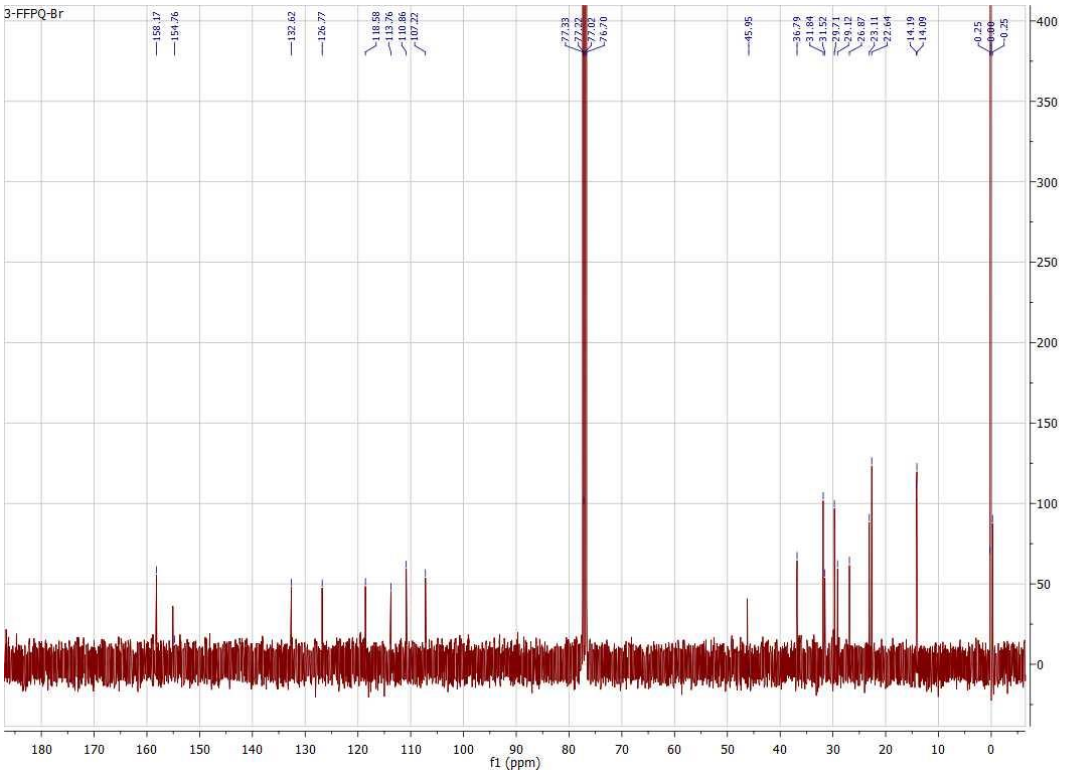

Appendix 10: ^{13}C NMR for Br-FFPQ-Br

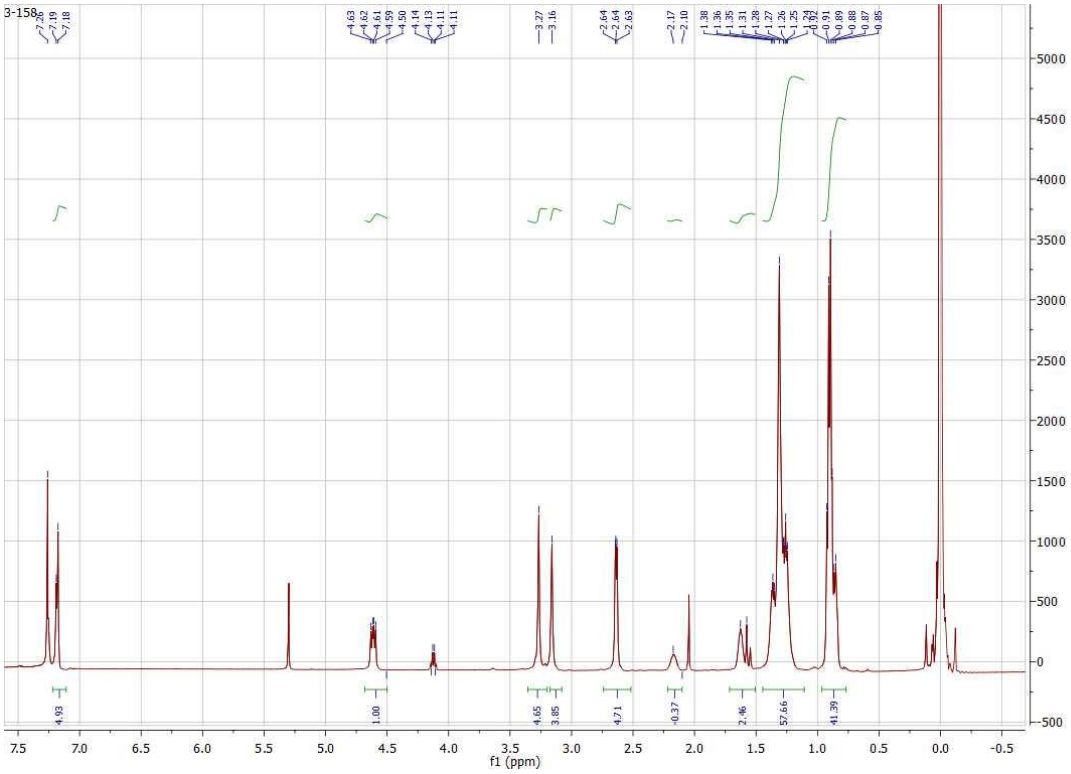

Appendix 11: ^{1}H NMR for Compound 21

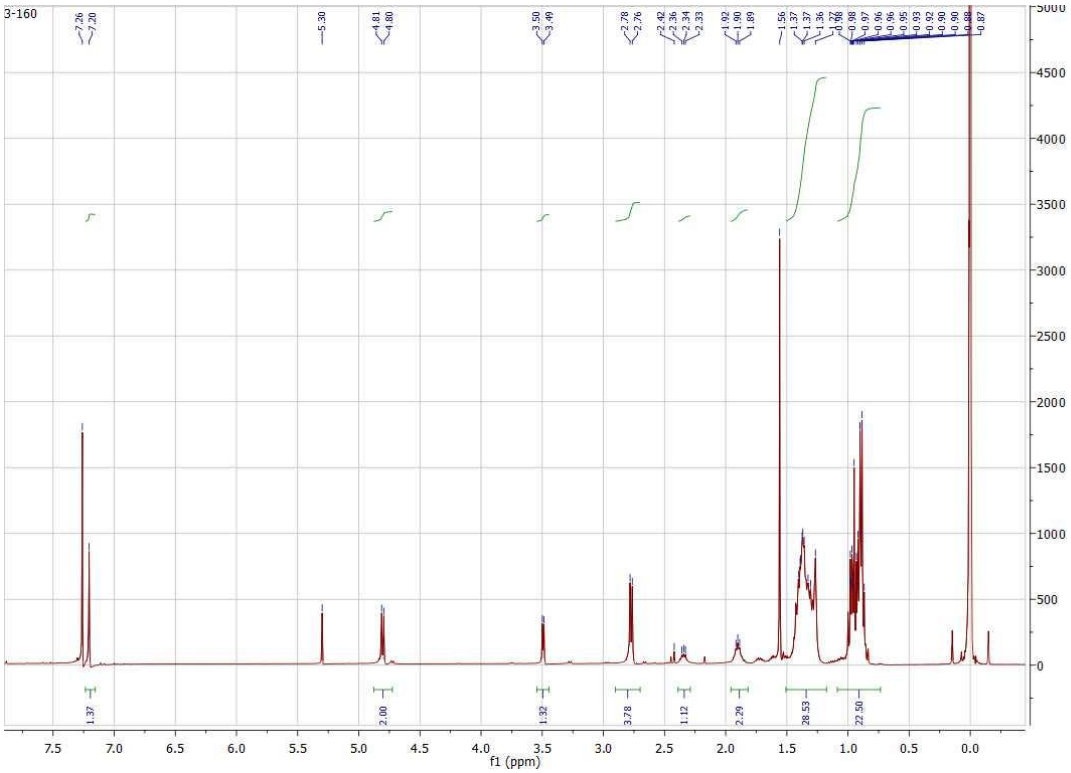

Appendix 12: ^{1}H NMR for Compound N6r

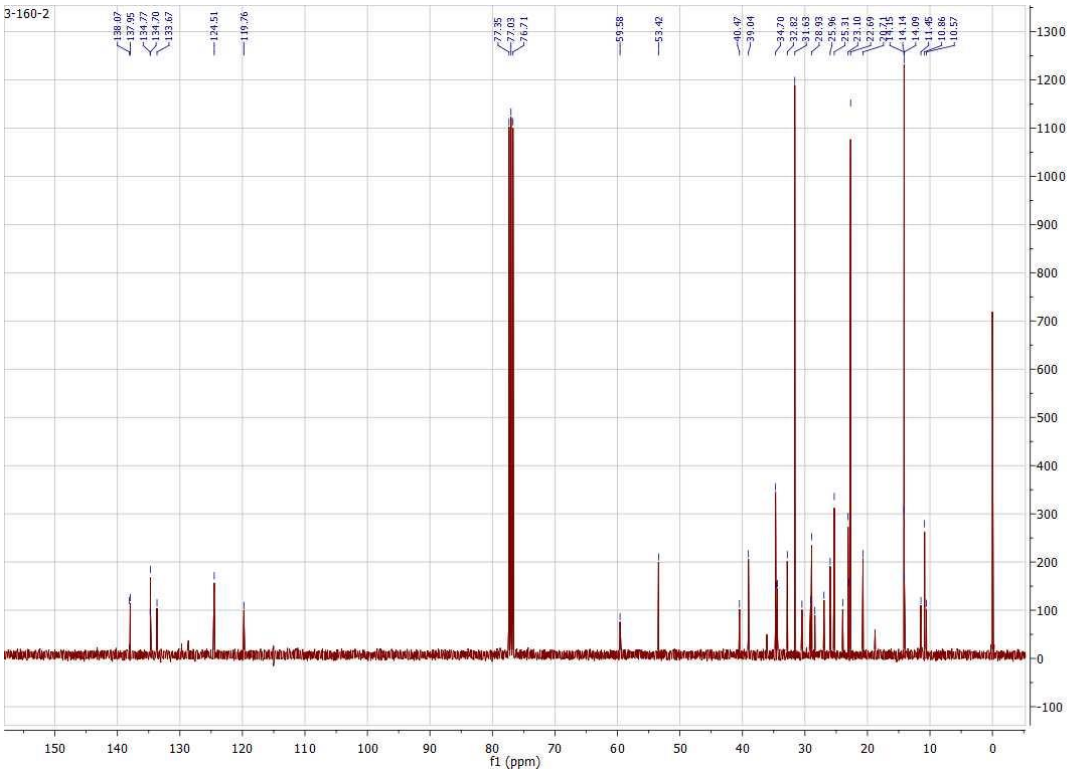

Appendix 13: ^{13}C NMR for Compound N6r

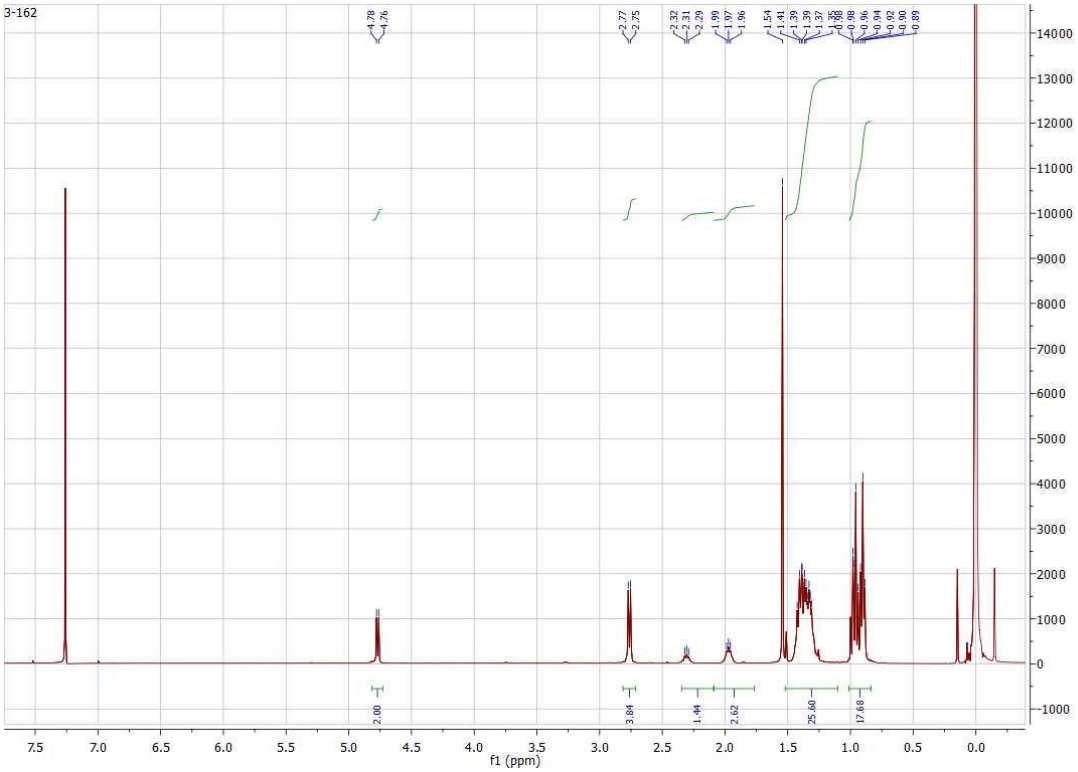

Appendix 14: ^{1}H NMR for Br-N6r-Br

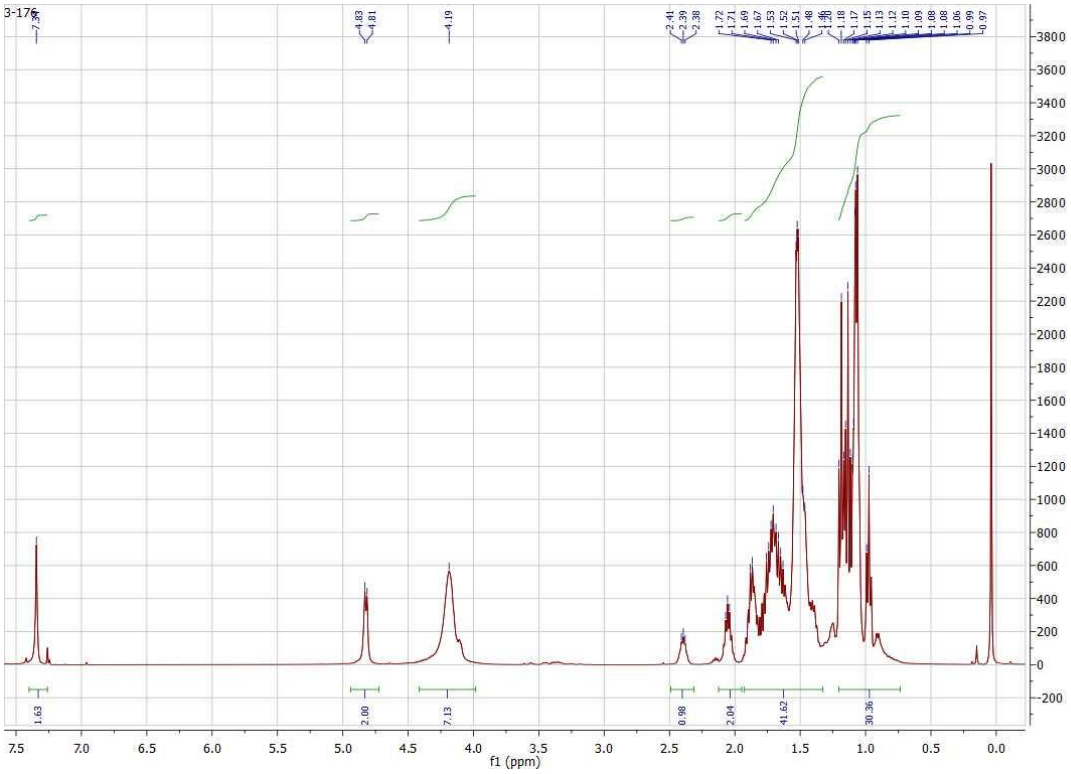

Appendix 15: ^{1}H NMR for Br-N10r-Br